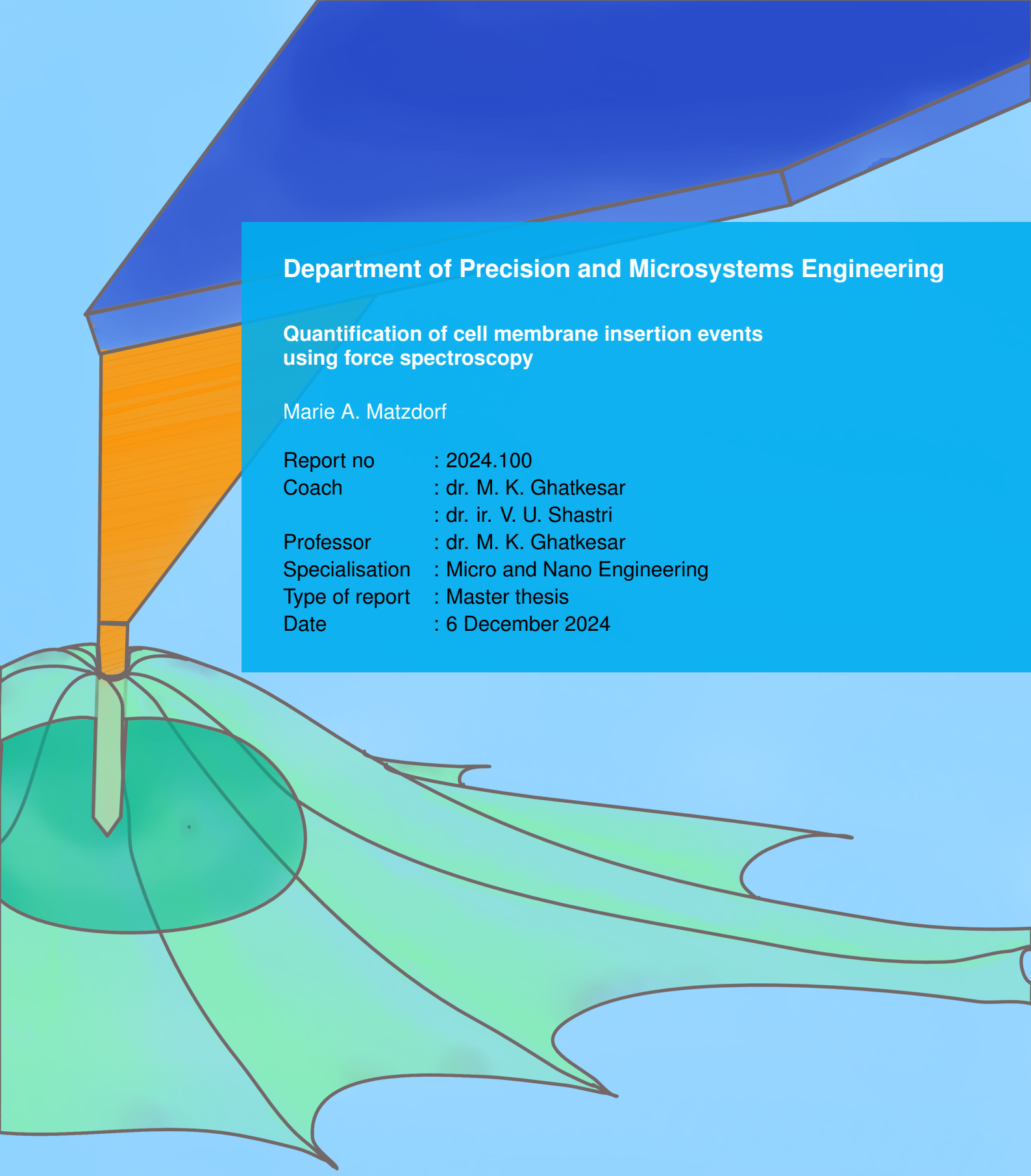

Department of Precision and Microsystems Engineering

Quantification of cell membrane insertion events using force spectroscopy

Marie A. Matzdorf

Report no	: 2024.100
Coach	: dr. M. K. Ghatkesar
	: dr. ir. V. U. Shastri
Professor	: dr. M. K. Ghatkesar
Specialisation	: Micro and Nano Engineering
Type of report	: Master thesis
Date	: 6 December 2024

TU Delft Delft University of Technology

Challenge the future

Quantification of cell membrane insertion events using force spectroscopy

by

Marie A. Matzdorf

to obtain the degree of Master of Science
at the Delft University of Technology,
to be defended publicly on Friday December 6, 2024 at 9:30 AM.

Student number: 4779886
Project duration: September 1, 2023 – December 6, 2024
Thesis committee:

Dr. ir. M. K. Ghatkesar,	TU Delft, supervisor
Dr. ir. V. U. Shastri,	TU Delft, daily supervisor
Dr. ME. Aubin-Tam,	TU Delft, external committee member

This thesis is confidential and cannot be made public until December 6, 2025.

TU Delft

Preface

I would like to thank the following people who have shown me support and help throughout this project. First and foremost, my supervisors Murali and Vijay for interesting discussions during our weekly meetings. Second, the MNE staff and students present during the department meetings where we got to share knowledge and experience to improve all of our work and presenting skills. Third, the technical lab support team for the lab training and helping me when I encountered any problems. Fourth, Maria Klimopoulou and Lidy Fratila-Apachitei from the department of Biomaterials and Tissue Biomechanics for providing me with the cell cultures.

Marie A. Matzdorf
Delft, December 2024

Contents

Introduction

Living cells form the smallest functional system of all living organisms and, based on their intricate structure and diverse functions, play an essential role in all life. Single cells can interact with each other using complex networks of intra- and intercellular signals. Cell biologists study many types of these living cells to understand their ways and to be able to apply this knowledge to larger tissue and organ systems. In addition, studying the fundamentals of biology has shown significant advancements in the available healthcare, such as medicinal drugs, cancer treatment, and tissue and organ transplants [47]. Therefore, single-cell studies are more than research out of curiosity for the essence of all living organisms; they have also proven to have a large societal impact on the overall well-being of the environment, animals, and humans.

One way to study single living cells is by studying how cells sense and respond to external mechanical signals; this field of study is often referred to as mechanobiology. The mechanical response of cells, for instance, stiffness and viscosity, can be correlated to various cell 'behaviours', such as cell adhesion, motility, division, differentiation, and whether diseased or not [34]. There are multiple means by which a single cell can be mechanically probed with a force and its subsequent deformation measured, for example, magnetic bead cytometry, laser particle tracking, magnetic tweezers, micropipette aspiration, and atomic force microscopy (AFM). However, from all available techniques, AFM has been regarded as the superior technique; this can be granted due to its compatibility in liquid environments, sensitive force feedback, the potential to measure both in quasi-static and dynamic mode and its high-resolution imaging capabilities [35].

Another approach to studying single cells is by analysing their subcellular contents, such as metabolites, proteins, mRNA, DNA, and mitochondria. For example, to give insights into the cell's chemical processes and chain mechanisms. See Figure 1 for an illustration of a typical mammalian cell and some of its main subcellular contents. To analyse these contents, they have to be extracted and isolated from one another. Traditionally, contents are extracted by submerging a population of cells in a solution that disrupts the cell membranes, resulting in a mixture of all cell contents in one solution. To isolate specific contents, such as the proteins, one must repeatedly centrifuge the solution to separate them based on density. This process involves the lysis (death) of cells, which may induce molecular changes to some of their contents, resulting in samples that may already be altered thus far to give false conclusions [33]. For example, proteins are very unstable and may change or degrade before analysis occurs. Additionally, if the temperature, pH or salt concentration is not suitable, the proteins are likely to be denatured, and if other experimental conditions are not optimal, the proteins can aggregate, or their structure may be destroyed due to undesired reactions. Also, metabolites are highly sensitive to environmental changes and can react and change within seconds [20]. Consequently, there is a need for methods to extract subcellular contents without cell lysis and with minimal damage.

In 2009, Meister et al. [38] proposed using an AFM embedded with a microfluidic channel for biological applications, enabling the injection of bioactive agents into single cells. These microfluidic cantilevers were known before as nano-dispensing (NADIS) probes; however, they now go by the name of fluidic force microscopy (FluidFM). The unique force feedback provided by the AFM system allows for sensitive monitoring of the injection process, specifically the cell membrane insertion by the probe tip. Guillaume-Gentil et al. first achieved a successful biopsy from single cells using FluidFM in 2016 [24], demonstrating both nuclear and cytoplasmic extractions from living cells. However, multiple technical challenges still exist, especially involving the insertion event, as it exposes the cell to high forces and deformation; thus, minimising these is crucial to avoid damaging the cell and perturbing the natural cell processes. Moreover, the success rates of the cell membrane and nuclear membrane insertion are extremely low due to the relatively large size of the FluidFM probe, making the research not reproducible. Furthermore, since cells are living organisms, there is a high variability in how cells respond to specific forces, compromising the research's reproducibility. A better understanding of membrane mechanics is required to optimise the insertion event, for example, by proposing new designs and settings for FluidFM.

This report consists of two main parts: I) the literature study and II) the research paper. The literature study is split into two sections: the literature study (chapters 1 to 4) and the research proposal (chapter 5). The literature study aims to review the use of AFM and FluidFM for single-cell analysis, focusing on single-cell injection and biopsy and the technical challenges involved. As single-cell biopsy consists of the puncturing of the cell membrane, different influencing factors that may affect the insertion event are reviewed, such as probe geometry and insertion velocity. Additionally, various approaches to model cell membrane insertion are explored, such as finite element analysis (FEA) and molecular dynamics, but more experimental methods are also considered. These findings are then concluded, and the research gap is identified. The research proposal follows the identified research gap, starting with the research goal and plan. Finally, the time planning, as well as risks and mitigations, are presented.

In the second part, the research paper aims to answer the research questions posed in the research proposal. Specifically, to improve the reproducibility and quantifiability of a cell membrane insertion event by collecting and analysing force spectroscopy data on mouse preosteoblast cells (MC3T3-E1). To reach this goal, the following objectives were defined and put into practice: (1) the microfabrication of custom tips with varying diameter on commercial cantilevers, (2) The creation and evaluation of algorithms tailored to process and analyse force-distance curves corresponding to cell membrane insertion, (3) The analysis of variables that affect the occurrence of insertion events, (4) The application of statistical analysis such as multiple linear regression to find individual and interacting effects of the factors that influence insertion event characteristics.

At last, the report presents a final thesis conclusion in the Outlook chapter, followed by recommendations for future researchers in this specific field. The Outlook chapter is ended by a reflection on the thesis project process and planning.

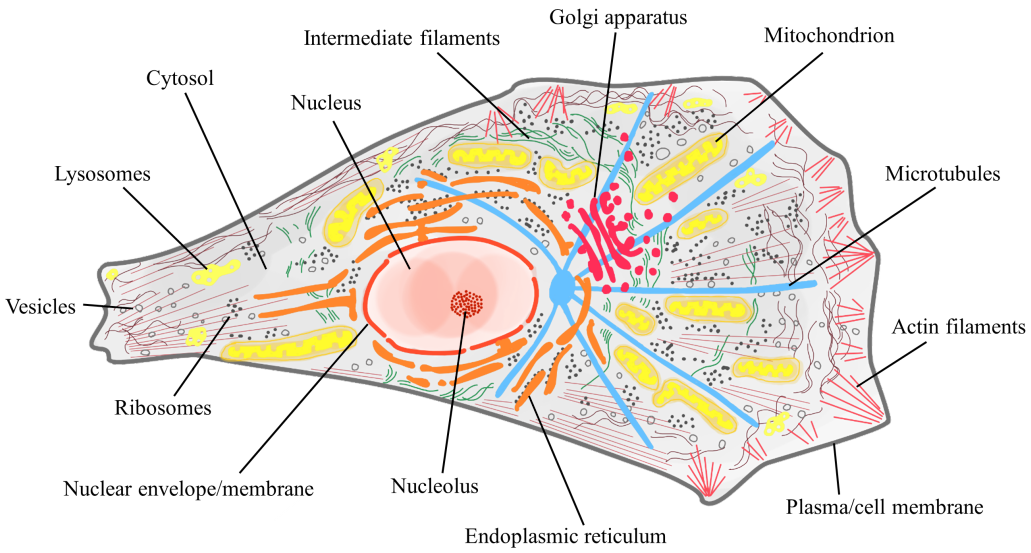

Figure 1: Illustration of a typical mammalian cell with its main components labelled. HeLa cells are commonly used for research and have an average size of 20 by 40 µm spread out on a glass slide, and only a height of a few micrometres (inspired by Milo & Philips (2015) [39]).

I

Literature Study

1

From AFM to FluidFM

1.1. Atomic force microscopy

To begin with, the atomic force microscope (AFM) consists of a cantilever probe which acts as a spring with a known spring stiffness, fixed at one end and free to probe a sample at the other. In surface science, a sharp pyramidal tip is attached to the end of the cantilever to detect nanometer-scale changes in the surface roughness; the sharper the tip, the higher the resolution. To detect changes in surface roughness, the probe (cantilever with tip) is put into contact with the sample surface using a piezo actuator (in the z direction), and it is scanned across the surface (in the x and y directions). As the probe scans the surface and encounters peaks and troughs due to the roughness of the sample surface, the probe cantilever will deflect up and down, respectively. This deflection can be measured using a laser reflecting off the end of the cantilever, which is detected using a photodetector. With the deflection $d_{cantilever}$ and the spring stiffness k of the cantilever known, the force applied by the cantilever on the surface can be calculated [3] using Hooke's law

$$F = -kd_{cantilever}. \tag{1.1}$$

Figure 1.1 shows how the AFM is set up. Since the conception of AFM, new applications of AFM have been found, leading to a wide range of multifunctional AFM probes in many research fields. In biology especially, the AFM can be used for imaging and manipulating biomolecules such as cells. Its compatibility with liquid environment, nanoscale resolution and force control make it especially appealing.

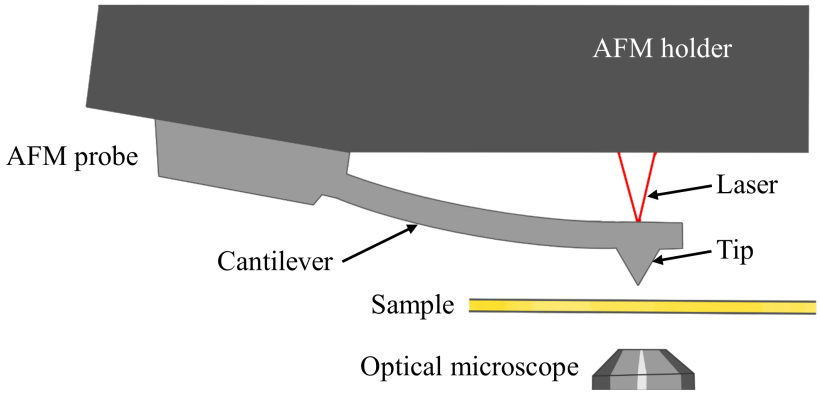

Figure 1.1: Schematic showing the AFM set-up (inspired by Guillaume-Gentil (2013) [21]).

As mentioned before, the spring stiffness of the cantilever should be known to calculate the exact force applied to the tip. However, due to variability in the geometry of the cantilever caused by the manufacturing process, the stiffness value changes even more. This is due to the stiffness varying with the inverse cube of the thickness of the cantilever. This is unavoidable, and the stiffness must be

found for each individual probe before the experiment. The most used calibration method is the Sader method, where the physical geometry of the cantilever (except the thickness) is measured using an optical microscope, and the quality factor (Q) is measured inside the AFM. The Q factor measures the bandwidth oscillation compared to the exciting frequency [8]. Then, Equation 1.2 is used to calculate the spring stiffness of the cantilever k (valid for a rectangular cantilever). Where ρ is the density of the medium (usually air or water), b and L are the width and length of the cantilever, Q_r is the Q factor at resonance, ω_f is the resonant frequency, and $\Gamma_i^f(\omega_f)$ is the imaginary part of the hydrodynamic function [8]. Typical dimensions of an AFM cantilever are a length of 200-400 µm and widths of approximately 40 µm.

$$k = 0.1906\rho b^2 L Q_r \omega_r^2 \Gamma_i^f(\omega_f) \tag{1.2}$$

1.1.1. AFM modes

Several AFM modes, such as contact and dynamic mode, force spectroscopy, and QI mode, may be used. Initially, the only AFM mode of operation was contact mode. This refers to scanning a sample using the tip to obtain a contour image. As the tip moves across the sample, the force applied to it is kept constant by adjusting the probe's height through a feedback loop [6].

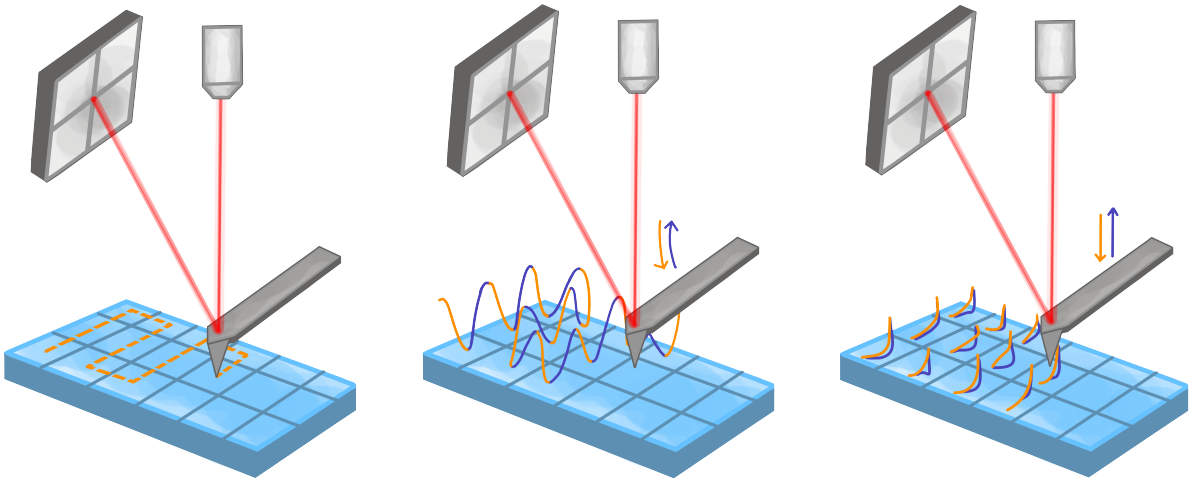

(a) Scanning mode (b) Tapping mode (c) Force-volume mode

Figure 1.2: Schematics of the main AFM modes (inspired by Dufrêne et al. (2017) [6]).

To image soft and delicate biological systems, the force applied should be minimised; thus, a new imaging mode was invented called dynamic mode (or tapping/oscillation mode). The tip is again scanned across the sample in this mode, but the cantilever is actuated with an oscillating force close to its resonance frequency. Only at the end of the tip's downward movement will it contact the sample, thus significantly reducing the force applied to it [6].

A more commonly used AFM mode for biological applications is force spectroscopy mode [6]. This involves the AFM probe only moving down (approach) towards and away (retract) from the sample while recording the force as a function of the probe position. The recorded data is then plotted in a graph called the force-distance curve, which provides interesting information about the biological sample. During the approach, besides still being able to quantify the height of the sample, it also shows the amount of deformation the sample undergoes due to the applied force, also called 'stiffness' measured in Newton-per-metre. During retraction, the force-distance curve shows a dip in the curve just before the release of the sample due to the adhesion force between the tip and the sample; see Figure 1.3 for a typical force-distance curve during an indentation of a cell. Another mode is called QI or force-volume mode [15], which takes hundreds or thousands of force-distance curves of the sample at different locations to generate a map of the sample, such as a height map, stiffness map, or adhesion map [11].

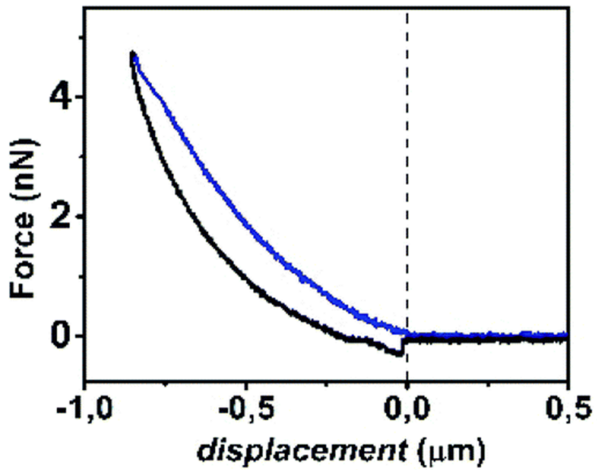

Figure 1.3: Typical indentation force-distance curve of a cell during approach and retraction. The slope of the approach curve describes the 'stiffness' of the cell, and the dip in the retraction curve describes the adhesion of the tip to the cell (adapted from Garcia (2020) [16]).

1.1.2. Imaging of cells

The AFM can image a cell adhered to a substrate, such as a glass slide, by tapping the cell's surface to obtain a height map (see Figure 1.4a). This technique was further advanced by slightly indenting the cell membrane at multiple locations to obtain a stiffness map; stiffer areas may represent the presence of organelles just beneath the membrane (see Figure 1.4b). By adjusting the actuation waveform of the AFM probe to a sinusoidal wave at the maximum indentation depth, the viscoelastic properties of the cell can be probed and mapped (see Figure 1.4c). These approaches allow for the visualisation of subcellular structures, such as the cytoskeleton and the nucleus, but only a 2D projection.

The imaging of the 3D arrangement of intracellular components has been made possible by nanoendoscopy-AFM [43]; this involves a needle-shaped AFM probe with a diameter below 200 nm and a sharp tip. The nanoneedle AFM probe penetrates the cell through to the substrate below at multiple locations. Inside the cell, the tip will interact with the liquid environment, molecular structures and organelles. All the while, the force spectroscopy curve is recorded during each z-scan with respect to time, which can be converted to a coloured 3D image, where areas with little resistance show up blue, and areas with high resistance (such as the cell nucleus) show up red. Even though this may sound invasive and the tip scan temporarily disrupted the encountered subcellular structures, Penedo et al. claim that the original structure is recovered without causing irreversible changes [43].

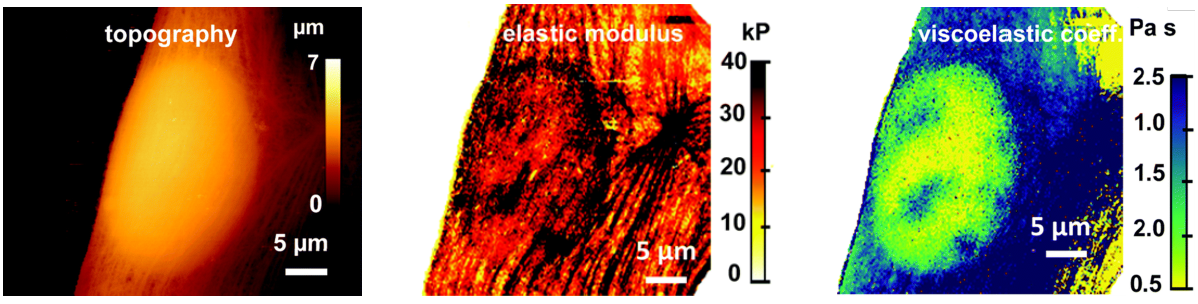

(a) Topography (height) map

(b) Elastic (Young's) modulus map

(c) Viscoelastic coefficient map

Figure 1.4: AFM imaging of a fibroblast cell using force-volume mode. Young's modulus map provides details of the outer cell structures, such as the actin crosslinked networks (cortex) and stress fibres. The viscosity coefficient map detects the presence of intracellular structures such as nucleoli (adapted from Garcia, Guerrero & Garcia (2020) [15]).

1.1.3. Manipulation of cells

The AFM can also be used to manipulate cells, for instance, indentation and adhesion experiments, picking up cells, local delivery of bioactive agents, and local extraction of subcellular components. This involves the force spectroscopy mode. A force is applied to a living cell at a specific location (a fixed

x-y point) by moving the probe only up and down (in the z-direction). As the probe approaches the cell and starts to push into the cell, both the cantilever and the cell will deflect and deform under the same force. The cantilever deflects because it feels resistance from the cell, and the cell deforms because it behaves as a soft material. Next, when the deflection of the cantilever reaches a predefined set point, the probe retracts from the cell, decreasing the force applied to the cell, and both the cantilever and the cell will deform towards their original shape. Leading up to the moment of release between the tip and the cell, the cell is adhering to the tip surface, resulting in a pulling force on the cantilever until the actual release, where the cantilever jumps back to its original shape. The AFM provides measurement data on the deflection of the cantilever $d_{cantilever}$ for a known displacement of the probe itself by the piezo actuator d_{piezo}, from which the deformation of the cell d_{cell} can be derived by

$$d_{cell} = d_{piezo} - d_{cantilever}. \tag{1.3}$$

Figure 1.5 depicts a schematic representation of this derivation. Plotting the data on the force applied (using Equation 1.1) and its resulting deformation of the cell during approach and subsequent retraction results in the force-distance curve. Force spectroscopy is a valuable tool when controlling the forces applied to a sample, such as indenting living cells, where the forces should be minimised to reduce the damage caused. To minimise the forces, a trade-off is made between a low spring stiffness of the cantilever (as flexible as possible) and sensitivity. As a result, a spring stiffness similar to the 'stiffness' of the cell is typically opted for.

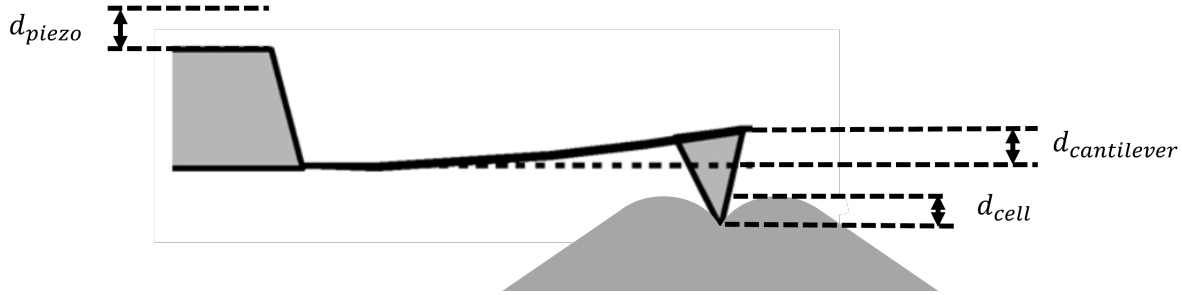

Figure 1.5: Schematic showing the three displacements and deformations involved in cell indentation experiments.

Several material properties used to define the cell's response to certain mechanical stimuli can be tested and found using the force spectroscopy feature of the AFM, for instance, the cell elasticity and viscosity or cell-substrate adhesion. During indentation experiments to test for cell elasticity, the cell may be modelled as a linear elastic material, and the force-distance curve can be fitted using the Hertz model to extract the cell's elasticity. The elasticity is measured using Young's modulus (or elastic modulus) measured in Pascal. The Hertz model is based on linear elastic deformation and depends on the indenter's tip geometry. The original Hertz model was derived for the contact between two spheres; later, Sneddon extended the theory for axisymmetric indenter shapes such as cones or paraboloids. Furthermore, Sneddon derived the relationship between the applied force and the indentation depth; for instance, for the conical indenter, see Equation 1.4 [30]. Where F is the applied force, h is the indentation depth, θ is the cone half angle, E is the Young's modulus, v the Poisson's ratio, and R is the radius of curvature of the AFM tip.

$$\text{Perfect conical indentor:} \quad F = \frac{2}{\pi}\frac{E}{1-v^2}(tan\theta)h^2 \tag{1.4}$$

The force-distance curves can be analysed by fitting the approach curve with a power law equation, see Equation 1.5, where a and m are fitting factors. The fitting factors depend on the properties of the indenter and sample; for example, a cone with a sharp tip ($R << h$) will have $a = \frac{2}{\pi}\frac{E}{1-v^2}(tan\theta)$ and $m = 2$. Moreover, how well the power law equation fits the force-distance curve is measured using the R-squared coefficient [30].

$$F = ah^m \tag{1.5}$$

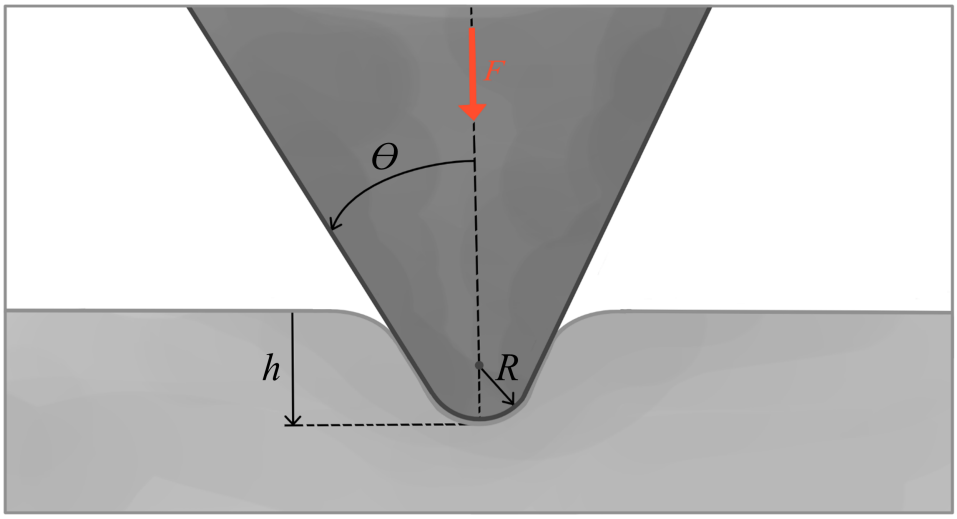

Figure 1.6: Illustration of Sneddon's sphere-conical indenter into a soft sample, labels are F the force, θ the cone half angle, R the tip radius, and h the indentation depth. For Equation 1.4, $R << h$.

However, the cell is known to behave nonlinearly due to the viscoelastic effect, and thus, the accuracy of the elasticity measurements determined without it is very much debatable [15]. Multiple models now exist to account for these viscoelastic effects. Such as the extended Hertz model with the elastic–viscoelastic correspondence principle, which includes dissipative processes [27], or the power law rheology model, which describes the viscoelastic properties under forces which vary in time [15]. Alternatively, cell 'stiffness' is measured, referring to the deformation caused by a force measured in Newtons per meter. It can be extracted from the slope of the force-distance curve, approximated by a linear regression [37].

In some cases, the tip can penetrate through the cell membrane and sometimes even the nuclear membrane. This penetration event is usually paired with a drop in force immediately after, and this can be seen on the force-distance curve as a peak. A typical force-distance curve during the approach is illustrated in Figure 1.7 during the penetration of the tip through the cell membrane. Different regions in the curve can be identified. Region I is when the tip starts approaching the cell and has not yet come into contact. The slope of the curve in this region is zero because no force has yet been applied to the AFM tip. Region II starts when the tip comes into contact with the cell membrane. As the tip moves further into the cell, the cantilever and cell deform, resulting in an increasingly sloped curve.

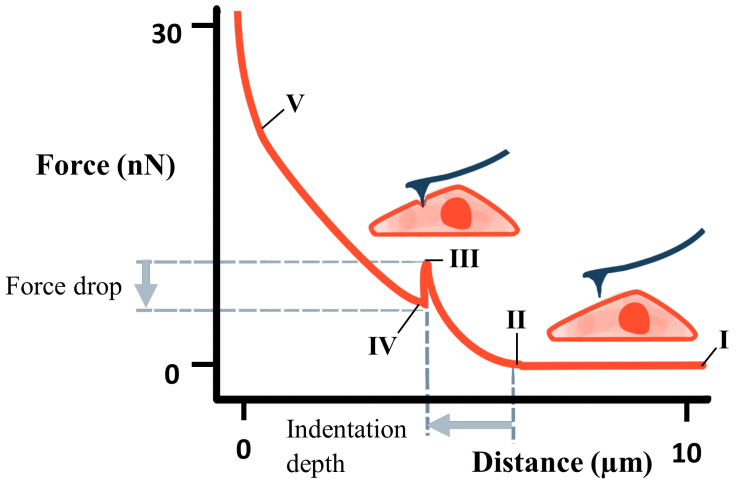

Figure 1.7: Schematic of an ideal force-distance curve during cell membrane penetration.

Region III is when the tip penetrates through the cell membrane; the curve shows a sudden drop in

force accordingly. After that, Region IV is the force the tip feels inside the cell. The slope of the curve in this region is most likely different to the first slope in Region II. Finally, in Region V, the tip starts to contact the rigid substrate underneath; this can be seen by the sharp increase in the slope of the curve. If the tip is placed above the nucleus, two force drops may occur, showing that the cell and nuclear membrane have been successfully penetrated, see Figure 1.8.

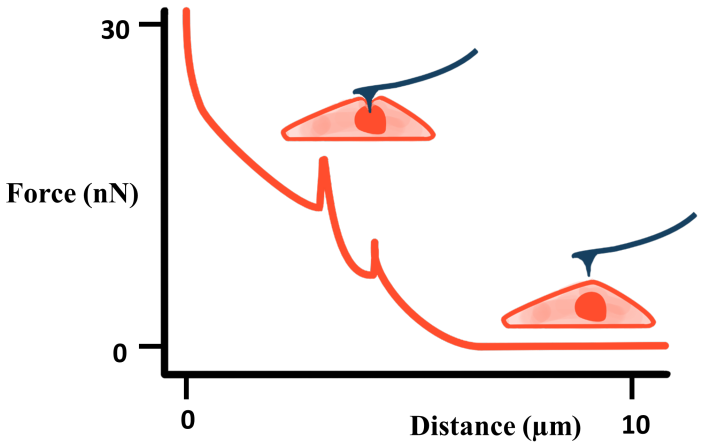

Figure 1.8: Schematic of a force-distance curve for cell and nuclear membrane penetration.

Using this technique, the AFM tip can access the cell's interior, and thus, bioactive agents that adhere to the tip (through surface functionalisation) can be delivered to a single cell through passive diffusion from the tip to its local environment [25]. These deliverables can be either diffused at the cell's periphery or injected if the tip successfully penetrates the cell membrane. These types of experiments can perturb the cell's biological processes, and their effects can be analysed, for example, the impact of a drug on a cell. Similarly, subcellular molecules may be extracted by passive adsorption to the penetrated tip surface; this has been successfully done for mRNA from mammalian cells. The largest challenge in the delivery or extraction of biomolecules is the dependence on passive or spontaneous reactions from or to the tip surface, which is difficult to control and unsuited for every molecule.

1.2. Fluidic force microscopy

The fluidic force microscope (FluidFM) incorporates a microfluidic channel inside the AFM probe, which is connected to a fluid reservoir and delivery system; the probe can act as a fluid dispenser or collector. The channel is considered microfluidic since its channel dimensions are in the range of 100 nm to 1 mm; one speaks of nanofluidics when the channel dimensions are less than 100 nm [4]. The microfluidic channel ends at or beside the apex of the probe tip; the latter is usually applied to keep the sharpness of the tip for cell penetration. A schematic of the FluidFM set-up is depicted in Figure 1.9. FluidFM employs many advantages of the AFM, such as force control and compatibility with a liquid environment, and solves the issue of uncontrolled passive desorption and adsorption during the delivery or extraction of molecules. By applying an overpressure or underpressure, the fluid delivery system can deliver or extract femto to picoliter volumes of a fluid with high controllability. Equally, as to the AFM set-up, the FluidFM uses an inverted optical or fluorescence microscope underneath the sample (typically a glass slide or Petri dish with the cell culture). This provides real-time visual feedback on where the FluidFM probe and the cells are positioned.

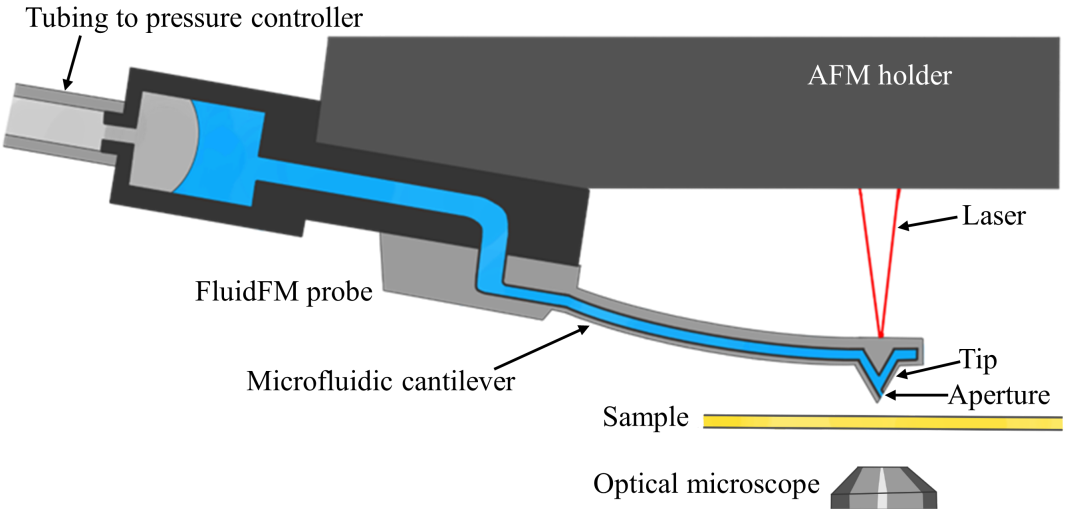

Figure 1.9: Schematic showing the FluidFM set-up (adapted from Guillaume-Gentil (2013) [21]).

The FluidFM probe used by Guillaume-Gentil and co-workers is depicted in Figure 1.10; this is the typical geometry offered now commercially by the company Cytosurge [44]. The hollow cantilever and tip are fabricated through traditional silicon wafer micro-manufacturing, whereas the aperture is milled post-fabrication using focused-ion beam (FIB) etching. Due to the fabrication limitations of silicon wafer micro-manufacturing, the tip is usually pyramid-shaped.

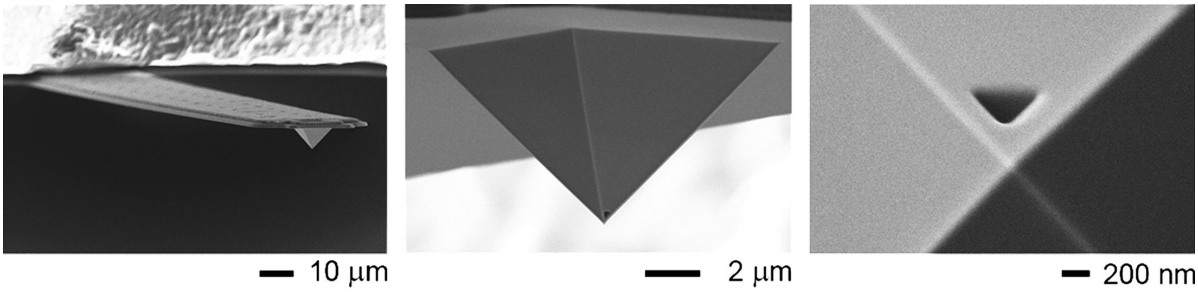

Figure 1.10: SEM images of the FluidFM probe used by Guillaume-Gentil and co-workers, consisting of a hollow cantilever, a pyramidal tip and a triangular aperture (adapted from Guillaume-Gentil et al. (2016) [24]).

1.3. FluidFM for single-cell analysis

Most single-cell analysis methods result in cell lysis (death) or major perturbations in the cell environment. As many subcellular processes and molecules rapidly react to these changes in the environment, the analysis results may be affected to such an extent that they do not accurately mirror reality and thus lead to false conclusions. Furthermore, by causing cell lysis, the possibility of performing any significant downstream analysis (e.g., the effect of injecting a drug after two days) on the same cell becomes nihil. Hence, there is a pressing need for single-cell analysis methods that reduce this invasiveness to a minimum and guarantee cell viability (life) after the analysis.

FluidFM, as a single-cell analysis tool, greatly minimises cell damage and increases the probability of cell viability after analysis, thus opening up many new opportunities for novelties in single-cell biology research. Since its invention in 2009, FluidFM has been used for cell adhesion experiments, injection of bioactive agents, and extraction of subcellular contents.

1.3.1. Injection into cells

The FluidFM probe tip is positioned above the cell cytoplasm or nucleus through the use of the inverted microscope, after which the tip is lowered towards the cell, first indenting and followed by a lesion of the cell membrane such that the tip of the probe penetrates the cell. Now that the tip has access to the cytoplasm or nucleus, a pre-loaded bioactive agent in the FluidFM probe can be dispensed locally

at the tip by applying an overpressure. Afterwards, as the probe is retracted from the cell, the cell membrane lesion closes immediately, resulting in a successful injection.

The alternative to FluidFM injection into cells is using glass pipettes and an optical microscope for positioning. Traditionally, this method is executed by the hand of a skilled person, which requires many training years, and still, the success rate is as low as 15% [51]. This is due to the lack of force control and the lateral vibrations that may tear the cell membrane and cause lethal damage to the cell. Additionally, the optical microscope cannot distinguish subcellular domains; thus, discriminating between mere contact with the cell membrane and puncturing the cell membrane is nearly impossible. FluidFM tackles these challenges; firstly, the penetrating tip is much sharper and attached to a flexible cantilever; the forces applied to the cell are thus much lower. Furthermore, the lateral vibrations are minimal due to the external vibration attenuation feature of the AFM setup. Secondly, the force feedback provides spatial information about the probe tip, such as height and ideally also at what moment the cell or nuclear membrane is penetrated [38].

The first successful injection using FluidFM was the injection of fluorescent dyes into the cytoplasm of myoblast cells; by fluorescence microscopy, the success of the injection could be observed as the dye was present and stayed inside the cytoplasm [38]. Later, injection into the nuclei of HeLa cells was also shown using fluorescent dyes [21].

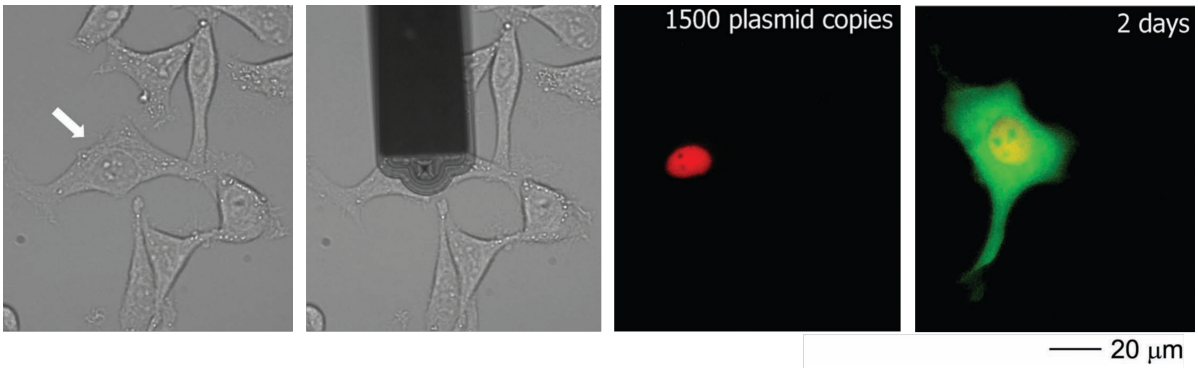

Figure 1.11: Injection with pmaxGFP (plasmid) into the nucleus of a HeLa cell using FluidFM; the first two phase contrast images showing the cell (indicated by arrow) just before and during injection. The two fluorescent images show the cell immediately and two days after injection. The DexTRITC (red) was co-injected with the plasmid to show it remained inside the nucleus; after two days, the cell produced the GFP (green). (Adapted from Guillaume-Gentil et al. (2013) [21].)

1.3.2. Extraction from cells

Similarly to the injection process, the FluidFM probe tip can access the cell cytoplasm or nucleus and extract a small volume of its surroundings by applying an underpressure, resulting in a successful biopsy of intracellular fluid. After extraction, the withdrawn contents can be immediately pipetted to further analysis techniques.

Single-cell biopsy techniques aim to take a snapshot of a cell at a given time via downstream analysis of the extract, which requires sample amounts in the range of picoliters [14]. Guillaume-Gentil et al. managed to sample both cytoplasmic and nucleoplasmic fluid from living cells dispensed and imaged by negative-stain transmission electron microscopy (TEM) [24], see Figure 1.12. They could visualise several subcellular components such as large vesicular structures, smaller globular structures and micro-sized filaments from the cytoplasm, and globular structures and short filaments from the nucleus. Later, by the same group, extracted metabolites from HeLa cells by FluidFM were dispensed into microarrays for time-of-flight mass spectrometry analysis to detect different metabolites [23]. Moreover, injection and extraction from single fungal cells are also achieved; for this study, stiffer cantilevers were necessary to penetrate the stiffer cell wall of fungal cells (compared to mammalian cells) [22]. Another remarkable result is the possibility of extracting RNA from living cells using FluidFM for RNA transcriptome profiling (reflects the current state of the cell). By keeping the cell alive, the state of the cell can be coupled to its downstream molecular and phenotypic properties; this new technique is called live-seq [5].

More recently, another aim of single-cell biopsy techniques is to study the impact of organelle transplantation between cells. FluidFM may extract an organelle from one cell and inject it into another. For example, the transplantation of mitochondria between living cells was achieved [13]. In this study, two

types of FluidFM tips were tested: the typical pyramidal tip and a new slanted cylindrical tip to reduce the invasiveness of the tip entrance. They found that mitochondria extraction was possible with both tip types; however, the injection was only possible using the cylindrical tip.

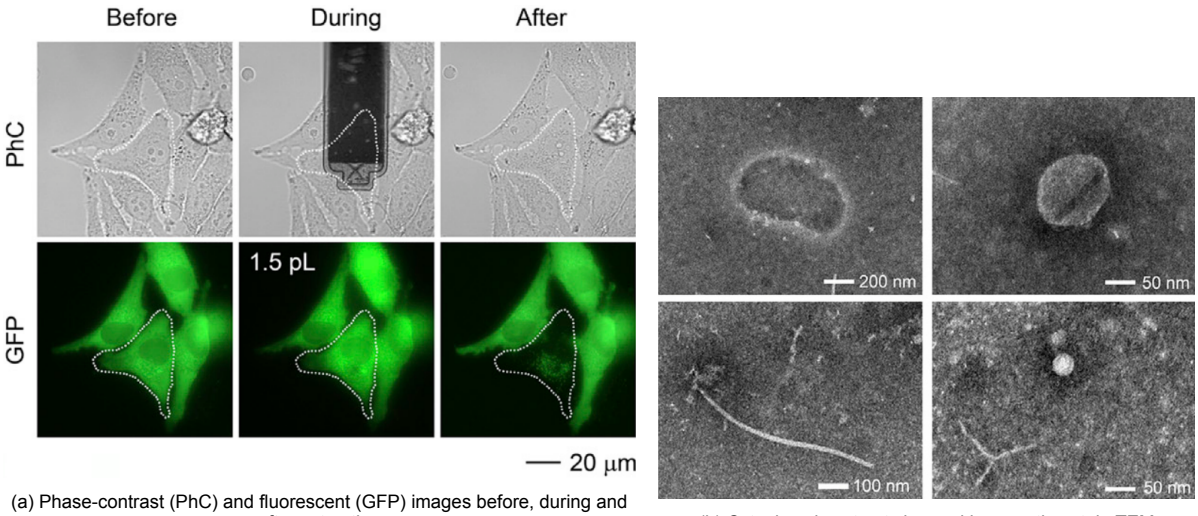

(a) Phase-contrast (PhC) and fluorescent (GFP) images before, during and after extraction

(b) Cytoplasmic extracts imaged by negative-stain TEM

Figure 1.12: Extraction of cytoplasmic fluid and dispensed on TEM grid for imaging (adapted from Guillaume-Gentil et al. (2016) [24]).

1.3.3. Technical challenges

The major advantage of FluidFM over other techniques, such as glass pipettes, is the force feedback; however, when analysing the FluidFM studies, the force-distance curves are not used to their full potential. An overview of the FluidFM papers, their experimental conditions and the force-distance curve characteristics is given in Table 1.1. Ideally, the force-distance curve indicates when the tip has penetrated the cell membrane and, if applicable, the nuclear membrane. Furthermore, the forces and indentation depths are minimised to avoid damage and to maintain some control over the spatial resolution. For relatively high indentation depths compared to the cell's thickness, the z resolution will be limited and more up to chance if targeting a specific molecule [47].

Nonetheless, using force feedback for FluidFM single-cell injection and especially biopsy seems inadequate, resulting in heavy dependence on optical feedback [34] and making the process time-consuming due to the low success rate [53]. This is mainly due to the design of the FluidFM probes, which require a minimum size of 300 nm to accommodate the microfluidic channel. However, to avoid clogging and when targeting larger molecules/organelles, usually the channels have diameters of around 1 µm. It is well known that the penetration success rate of relatively large AFM probes (pyramidal shape and tip radius of 100 nm) is around 15% [29]. Therefore, FluidFM suffers from reproducibility problems.

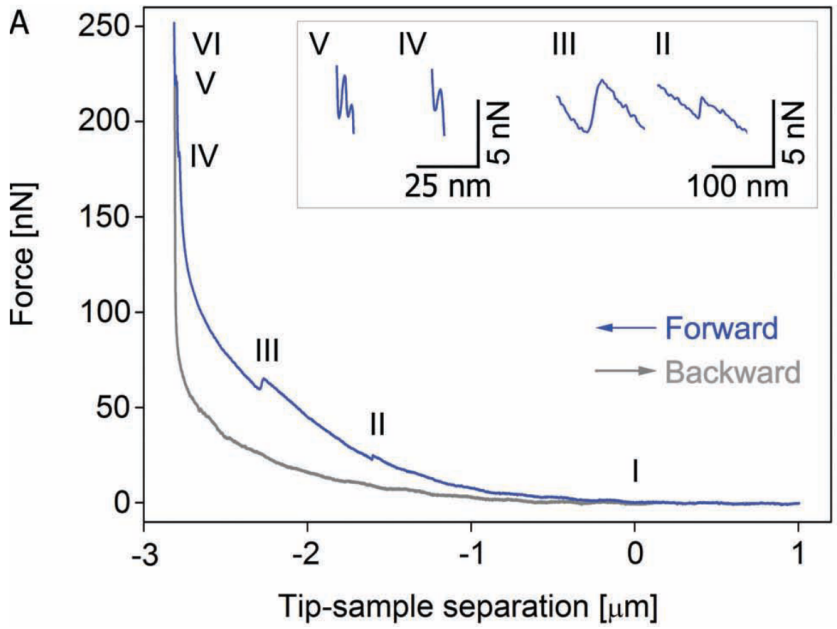

Figure 1.13: The ”typical” force-distance curve acquired from a penetration experiment using a FluidFM probe (adapted from Guillaume-Gentil et al. (2013) [21]).

Moreover, when inspecting the force-distance curves (see Figure 1.13), the force required to penetrate the membrane is in the range of tens [21, 24, 23] or even hundreds [13] of nN. This is far above the rule of thumb to stay below 100 pN to avoid damage to biological samples [6]. Furthermore, the indentation depths before penetration are typically half of the cell's original height, significantly reducing the spatial resolution in the z-axis. Additionally, the force drops to indicate a successful penetration are in the pN range, where it becomes debatable whether it resulted from an actual penetration or other factors such as noise, cell movement, or cell relaxation.

As single-cell injection and biopsy involve the penetration of at least the cell membrane, the variability of cells also poses a serious challenge. Even if the cell type is the same, their dimensions, the location of the subcellular contents, and their behaviour in response to mechanical stimuli can still vary enormously [34]. Due to this unavoidable variability, optimising an experimental set-up, such as FluidFM, becomes extremely difficult. Finding the perfect compromise between spatial resolution, reducing damage to the cell, and the probability of a successful penetration.

Another advantage of FluidFM over other techniques is the potential to require less optical feedback to position the tip above the cell. However, this feature still needs to be fully exploited, possibly due to the more complicated settings for scanning the height profile of a cell without exerting too large forces. The inverted optical microscope provides the optical feedback in the FluidFM set-up, and due to the morphology of the FluidFM probe, the view of the tip apex placed above the cell is blocked. Accurate visual positioning is, therefore, also hindered. Furthermore, the visual feedback is limited to only the x and y planes, providing no information about the distance between the probe tip and the cell. Moreover, it is further restricted by the depth of focus of the optical (or fluorescence) microscope; this means that both the AFM probe and the cell can only be in focus at the same time if they are in sufficient proximity to each other. Thus, improving the FluidFM set-up with the ability to sense the location and height profile of the cells can reduce the dependency on the optical microscope and offer more accurate positioning of the probe [47].

Table 1.1: Overview of FluidFM probes, where r is the tip radius, k the cantilever stiffness, and v the velocity of the probe while it is inserted into the cell.

Material	Tip shape	r (nm)	Aperture shape	Aperture size (μm)	k (N/m)	v ($\mu m/s$)	Cell type	Penetration force (nN)	Force drop (nN)	Indentation depth (μm)	Reference
Si3N4	Pyramid	10	Circle	0.3	0.3	0.05	C2C12	3.4	0.5	0.05	Meister et al. (2009) [38]
Si3N4	Pyramid	10	Triangle	0.2	0.2	0.5	HeLa	25, 60	2, 4	1.5	Guillaume-Gentil et al. (2013) [21, 24, 23]
SU8	Angled	1000	Circle	25	3.7	-	C2C12	40	2	0.2	Kramer et al. (2020) [31]
Si3N4	Pyramid	10	Triangle	1.1	5	-	U2OS, COS7, HeLa	80	-	-	Gabelein et al. (2022) [13]
Si3N4	Cylinder	25	Circle	1.2	2	-	U2OS, COS7, HeLa	400	-	-	Gabelein et al. (2022) [13]
Si3N4	Pyramid	10	Triangle	0.2	2.3	1	Yeast	2000	-	2	Guillaume-Gentil et al. (2022) [22]
SU8	S-shape	25	Circle	1	37	-	MCF-7	50, 100	5	5	Glia et al. (2023) [18]

1.4. Two-photon polymerisation for AFM and FluidFM fabrication

Commercial AFM and FluidFM probes are made from silicon or silicon nitride using micro-manufacturing techniques, limiting the customisation of the tips. Other techniques have been proposed to post-process the available tip using physical or chemical etching, 3D manufacturing the tip onto a commercial (tipless) cantilever or 3D manufacturing the complete probe. The methods discussed in this section are two-photon polymerisation and the possibility of using focused-ion beam (FIB) etching in some cases.

Two-photon polymerisation (2PP) is a 3D manufacturing technique which can create structures with nanoscale resolution (100 nm). It uses a femtosecond laser to polymerise a photosensitive material (resin) initiated by two-photon absorption [10]. Due to the two-photon absorption process, the region that has a high probability of being affected by the laser is confined to a tiny volume at the laser's focus, called a voxel (similar to a pixel in 2D). By moving the focus of the laser beam inside the resin, a 3D structure can be fabricated, after which only the remaining resin is washed away [10].

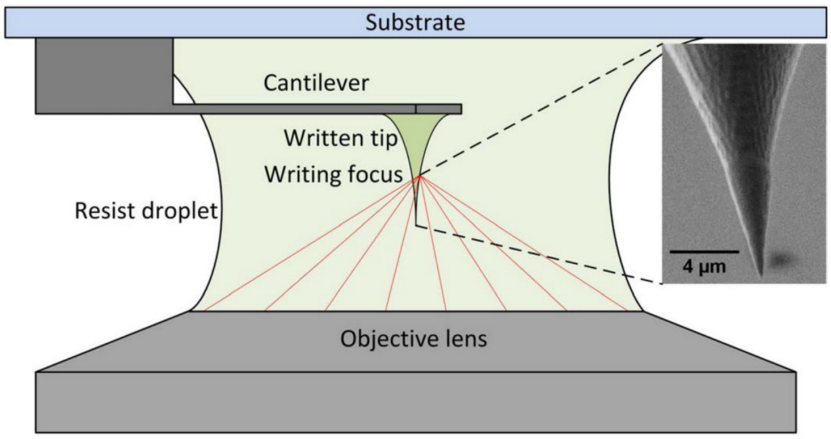

Figure 1.14: Schematic working principle of 2PP (adapted from Göring et al. (2016) [19]).

2PP offers new possibilities for customising AFM and FluidFM tips and cantilevers, raising the question of the optimal design of such a probe for a specific scenario. Several studies have shown successful 2PP manufacturing of tips onto commercially available tipless cantilevers. Suriano et al. (2016) [49] printed a cylindrical tip with a diameter of 3 µm on a commercial silicon nitride cantilever. Göring et

al. (2016) fabricated very sharp conical tips with a tip radius of 25 nm, also on commercial cantilevers. Additionally, they successfully printed protruding tips so that the end of the tip is visible from the top (or bottom), allowing for more accurate visual positioning [19]. Glia, Deliorman & Qasaimeh (2022) [17] also printed conical tips; however, they only managed to reach a resolution of 200-400 nm to ensure proper stability of the printed material. Differences in material, hatching and slicing distance, laser power, and writing speed will affect the printed outcome [17].

The 2PP fabrication technique is limited by resolution (typically 200 nm) and its material choice. The most used polymers for 2PP are SU-8, IP-Dip, and IP-S, which have a much lower Young's modulus, □3 GPa, than silicon, □150 GPa. Subsequently, the tip can be post-processed to change some characteristics. For instance, the polymer tips can converted into carbon by pyrolysis. This involves heating the polymer to 900°C in an inert environment; this causes the tip to shrink, thus becoming smaller, sharper and harder [19]. Alternatively, the tip can be further etched using FIB to obtain, for example, a sharper tip or a different geometry [17].

Using 2PP for the fabrication of FluidFM probes offers several advantages. The microfabrication techniques used to fabricate silicon AFM probes become much more complex for FluidFM fabrication, resulting in a time-consuming and, thus, costly process. 2PP can provide a much faster process, allowing for quick design iteration and greater design freedom [31].

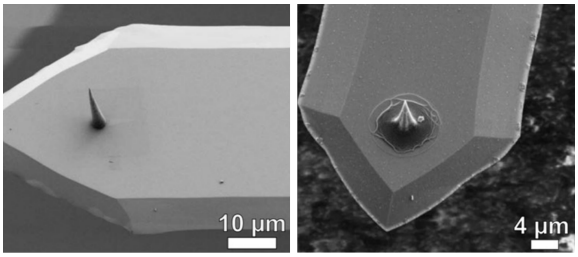

(a) Sharp tip (left) and tip after pyrolysis (right) (adapted from Göring et al. (2016) [19])

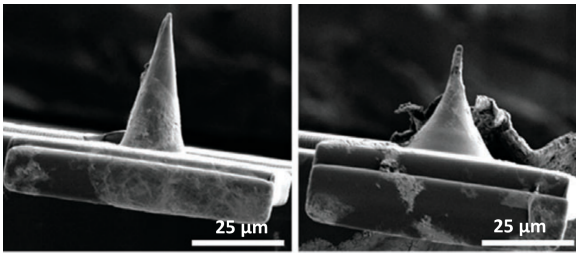

(b) Two different tip geometries (adapted from Glia et al. (2022) [17])

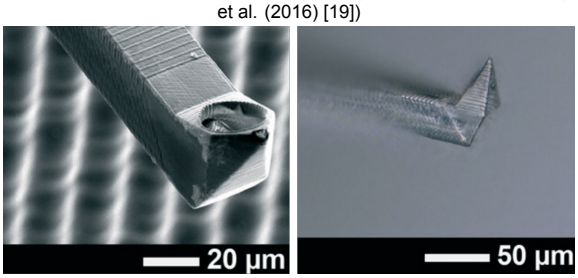

(c) FluidFM probe with large aperture (left) and AFM probe (right) (adapted from Kramer et al. (2020) [31])

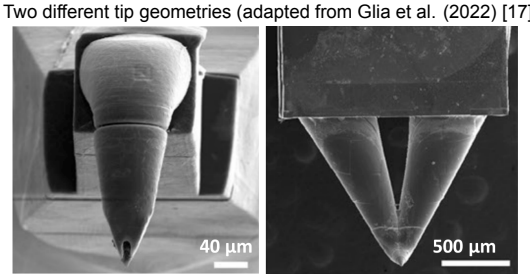

(d) Single channel FluidFM (left) and dual channel FluidFM (right) (adapted from Glia et al. (2023) [18])

Figure 1.15: Examples from the literature show successful printing using 2PP of tips onto commercial AFM cantilevers or the complete probe.

Building on their previous work, Glia, Deliorman & Qasaimeh (2023) [18] expand their 2PP fabrication of AFM tips to FluidFM, successfully creating single and dual channelled probes. The design freedom aspect has been more thoroughly enjoyed, as elephant trunk-like tips were chosen for stability and clogging reasons. Furthermore, they claim that the material used, SU-8, is an excellent material to reduce tip contamination due to its hydrophobic surface and is suitable for cell manipulations due to its soft and thus gentle nature [18].

All the previously mentioned 2PP papers are summarised in Table 1.2 to compare their achievements and which 2PP parameters they used. Unfortunately, Glia and co-workers did not share all their printing parameters.

Table 1.2: Overview of studies fabricating AFM and FluidFM tips using 2PP and their respective printing parameters and post-processing steps

Tip shape	Laser power (mW)	Writing speed (mm/s)	Hatching (µm)	Slicing (µm)	Material	Post-processing	Ref.
Cylinder with hemisphere on top, diameter 3 µm	15	0.1	0.3	0.1	PFPE-PETA	Gold coated	Suriano et al. (2016) [49]
Cone with sharp tip, 25 nm radius	-	20 (1 for tip end)	0.1 (0.05 for tip end)	0.1 (0.05 for tip end)	IP-Dip (63x)	-	Göring et al. (2016) [19]
Cone base 20 µm, height 30 µm	-	100	-	-	SU-8	Gold coated, FIB etching for HAR	Glia et al. (2022) [17]
Hollow cantilever and tip, aperture diameter 25 µm	20	60	0.3	0.5	IP-S (25x)	-	Kramer et al. (2020) [31]
Cone base 20 µm, height 30 µm	-	100	-	-	SU-8 (25x)	Gold coated, FIB etching for smaller apertures	Glia et al. (2023) [18]

1.5. Discussion

The emergence of FluidFM technology has opened many new research opportunities for single-cell biology. It has the potential to inject bioactive agents and extract subcellular content for further analysis without impacting the viability of the cell after the assay. No other technique could extract subcellular contents without causing cell lysis. On the one hand, FluidFM offers many advantages, making it an excellent candidate for this application. On the other hand, diverse technical challenges still exist, limiting the offered advantages to be used to their full potential. Furthermore, cell-to-cell variability is unavoidable, thus making the reproducibility of results extremely difficult and up to chance. For single-cell injection and biopsy, penetration of at least the cell membrane is required to access the cell's interior. More knowledge is needed on the behaviour of this membrane when subjected to a FluidFM probe. Furthermore, new designs can be explored with the advent of 2PP fabrication of FluidFM tips. It is, therefore, necessary to understand the cell membrane mechanics to make substantiated choices regarding the FluidFM probe design.

2

Analysis of cell membrane penetration

Even before FluidFM, the cell membrane penetration using AFM encountered the same problems: low success rate, high penetration forces, and large indentation depths. Considerably more work has been done to improve these issues using AFM, mainly because it is an older technology. This section aims to learn from the AFM papers how the cell membrane responds to specific mechanical stresses and also what is lacking. Firstly, the force-distance curve is analysed to identify which quantities determine a successful penetration event; secondly, by studying what factors influence these quantities and in which way. This information can give insights into how the FluidFM can be improved to overcome these technical challenges.

2.1. How to determine cell membrane penetration

To understand the mechanics behind cell membrane penetration, one should look first at its constituents and what it is made of. The cell membrane is the boundary between the internal substances of the cell and its environment. This membrane is made up of phospholipids, a molecule that is made up of a hydrophilic part (head) and a hydrophobic part (tails) that naturally align to bring together the heads with heads and tails with tails [39]. Different arrangements are possible in this situation (assuming a water-based environment), for example, circular structures with all the tails facing the centre and the heads facing outward; this is called a micelle. Another structure goes by the name of lysosome; these are similar in shape but consist of a double-layered membrane, a bilayer. The cell membrane is a larger structure comprising a phospholipid bilayer, as well as many different transmembrane proteins and other types of fats such as cholesterol, and has a thickness of about 4 nm [39]. Interfacial hydrophobic, hydrophilic, and van der Waals interactions hold all these constituents together. [29]

In the event of a membrane rupture due to the persisting force applied by an AFM tip, a nanoscale hole forms abruptly, letting the tip pierce through to the internals of the cell. This event is paired with a sudden drop in force, which can be identified on the F-d curve as a peak. However, this might also occur due to tip interactions with membrane proteins or a shift of organelles or the cytoskeleton [29]. Various papers defined a force drop threshold value, such as 500 pN [41], to decide if it indicates cell membrane penetration. In comparison, most others decided whether the force drop was present or not.

Furthermore, the curve's slope corresponding to the cell's local "stiffness" will change after the penetration event, as the cytoplasm is mostly water. Therefore, an indication of cell membrane penetration could be the change in the slope of the force-distance curve [29]. Penedo et al. (2021b) [42] define a successful penetration event based on whether the force-distance curve shows a force drop or a long plateau after contact with the cell. Figure 2.1 depicts the curves found: unsuccessful penetration, successful penetration based on force drop, and successful penetration based on the long plateau.

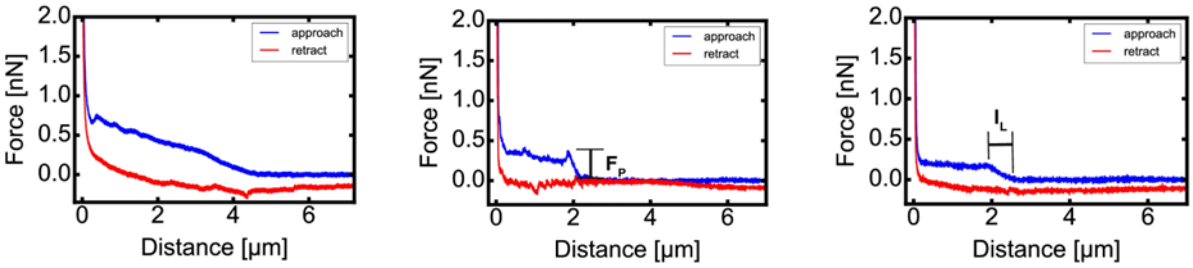

(a) Force gradually increases without a force drop nor plateau

(b) Force drop (F_p) present after a certain indentation depth

(c) Long plateau present after a certain indentation depth (I_L)

Figure 2.1: Example force-distance curves from Penedo et al., three curve types are identified, where (a) is an unsuccessful and (b,c) are successful penetration events (adapted from Penedo et al. (2021b) [42]).

Some papers have used this indication instead of a force peak, as they saw an apparent plateau in the curve [42]. Whereas Bitterli [29] believes that the combination of a change in slope and a force peak with a certain threshold is a correct indicator. It is clear that a universal definition of what indicates a successful cell membrane penetration event is lacking. Once a definition is found, the force-distance curves can be categorised as successful and unsuccessful, and the probability of success can be determined for every experiment and compared to others.

2.2. Influence of tip geometry and sharpness

To enhance the penetration likelihood, the tip's sharpness—measured as the tip radius—can be increased (made sharper) to facilitate a smoother insertion into the cell. However, it is equally crucial to examine the impact of the tip radius on penetration force, force drop, and indentation depth.

Obataya et al. (2005) [41] compared two nanoneedle probes with a diameter of 200 nm, one with a sharp cone-shaped tip and the other with a flat-ended tip. The force-distance curves during their insertion into living melanocytes (NHEM) were observed, and the peak phenomena during penetration were analysed, see Figure 2.2. The sharpened nanoneedle probe resulted in an initial force slope with a quadratic function first, followed by a linear function, due to the change in geometry from conical to cylindrical. The flat-ended nanoneedle probe showed only a linear force slope. According to Obataya et al., these observations can be adequately estimated using the Hertz model. Furthermore, the penetration force for the sharp tip was higher, 1.5 nN, compared to the flat-ended tip, only 1 nN. Similarly, the indentation depth for the sharp tip was larger than the flat-ended tip, 1.4 and 1.1 µm, respectively. Additionally, both force drops brought the force down to 0.4 nN, thus the force drop for the sharp tip was larger.

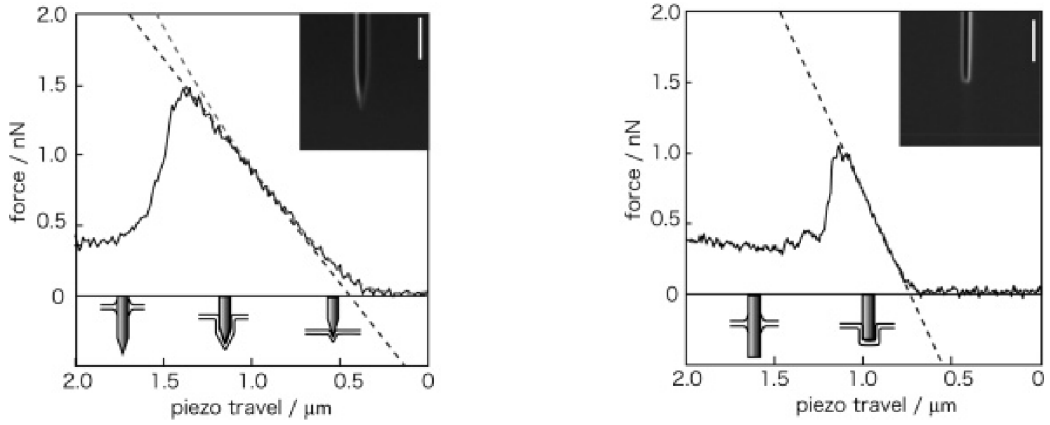

(a) Sharp cone-shaped tip

(b) Flat-ended tip

Figure 2.2: Force-distance curves during penetration of NHEM using a sharp and flat-ended nanoneedle probe, including an SEM image of the tip used (scale bar indicates 500 nm) (adapted from Obataya et al. (2005) [41]).

However, changing the diameter of the nanoneedle tip may have an even more significant effect on

the penetration force, indentation depth, and force drop than tip sharpness. Another study by Vakarelski et al. (2007) [50] builds forth on this by fabricating even thinner nanoneedles using bottom-up carbon nanotube (CNT) assembly on commercial AFM tips. These CNTs needed a carbon coating to increase their stability, resulting in a diameter of about 30-40 nm and a more variable length of 1 to 5 µm. The force-distance curves show very low penetration forces around 0.1-0.2 nN and small indentation depths of 0.1-0.2 µm. However, these results are difficult to compare with Obataya et al. since a different type of cell (human epithelial cells) was used. However, they conclude that the decrease in diameter by a factor of 10 does play a role.

Another important quantity, which is not mentioned in Obataya et al. and Vakarelski et al., is the penetration success rate. In the study by Han et al. (2008) [25], a nanoneedle with a diameter of 200 nm and length of 6 µm, where the surface is treated such that the gene that expresses the GFP protein is adsorbed onto it. The AFM drives the nanoneedle into both human embryonic kidney cells (HEK293) and human mesenchymal stem cells (hMSC) through the cell and nuclear membranes. A successful penetration is then judged from the resulting force-distance curve, the first and second force drops indicating a successful cell and nuclear membrane penetration. They found that the penetration success rate of the cell membrane (one or two force drops in a curve) for both HEK293 and hMSC was about 90%, whereas for the nuclear membrane (two force drops), only 40% for HEK293 and 10% for hMSC. In the case of hMSC, the large indentation depth (2-3 µm) before penetration resulted in the cell and nuclear membranes touching and thus penetrating both simultaneously, resulting in only one force drop.

Important to note is the lack of information on the number of samples and the statistical analysis in the papers mentioned. As they are dealing with living cells and thus highly variable physical properties, doing a tenfold of experiments is insufficient to cover the wide variety of possible measurements.

Bitterli (2012) [29] stresses the importance of doing proper experiments with as many sample points as possible to allow for statistical analysis with a higher confidence level. In her PhD thesis, two probes with different sharpness, tip radius 10 nm and 100 nm, are tested on human osteosarcoma cells (SaOs-2) for a range of set point forces (1-18 nN). The resulting force-distance curves are analysed, and the performance of the probes is compared with the probability of a successful penetration event. She finds that this probability for the sharper 10 nm tip is already 84% for a set point force of 5 nN, whereas the 100 nm tip only reaches 44% at a higher set point force of 18 nN (see Figure 2.3). Moreover, she compares the effect of having different set point forces on the probability of having zero, one, two and three successful penetration events. The results show that a higher set point force increases the probability of more penetration events occurring in one force-distance curve. Thus, in the case of a biopsy or injection from or into the cytoplasm, the set point force must be chosen such that the probability is highest for only one penetration event.

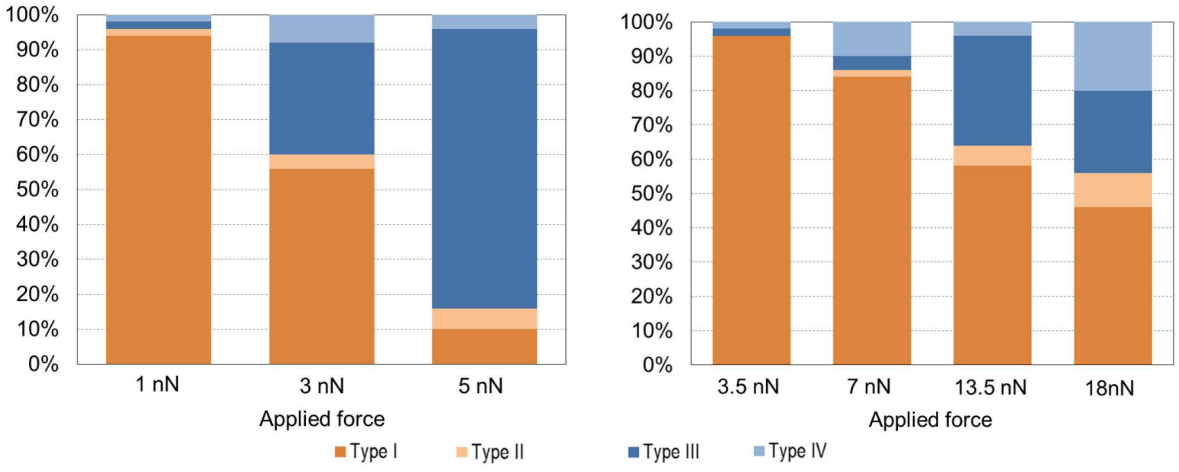

(a) 10 nm tip radius

(b) 100 nm tip radius

Figure 2.3: Distribution of force-distance curves across four curve types as a function of the set point force for a 10 and 100 nm tip radius. Type I) No force drop, Type II) Force drop but no change in elastic modulus, Type III) Force drop and a decrease in elastic modulus, Type IV) Force drop and an increase in elastic modulus. Type I and II are unsuccessful, and Type III and IV are successful penetration events. (Adapted from Bitterli (2012) [29].)

Other studies, such as Angle et al. (2014) [1] and Fan et al. (2018) [9], also compare sharp pyramidal tips to flat tips and to sharpened nanoneedle tips, respectively. Both yield results that indicate a higher penetration success rate for the sharper tips, as shown in Figure 2.4. The penetration forces for a flat tip have a median of 22 nN; for the pyramidal tip, 12 nN, and the nanoneedle tip, the penetration forces are below 1 nN. Comparison, however, remains debatable. The set point force and the cell type differ in the two experiments. Angle et al. used a high set point force of 100 nN and HEK293, whereas Fan et al. used a low set point force of 3 nN and human fibroblast cells (h-FB).

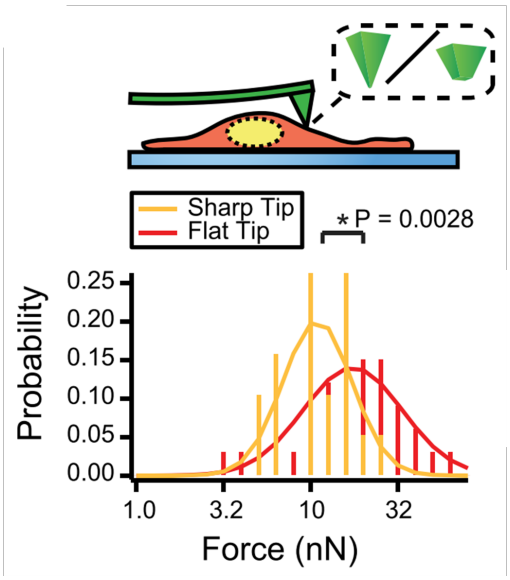

(a) Probability distribution as a function of the penetration force for two different probes (adapted from Angle et al. (2014) [1])

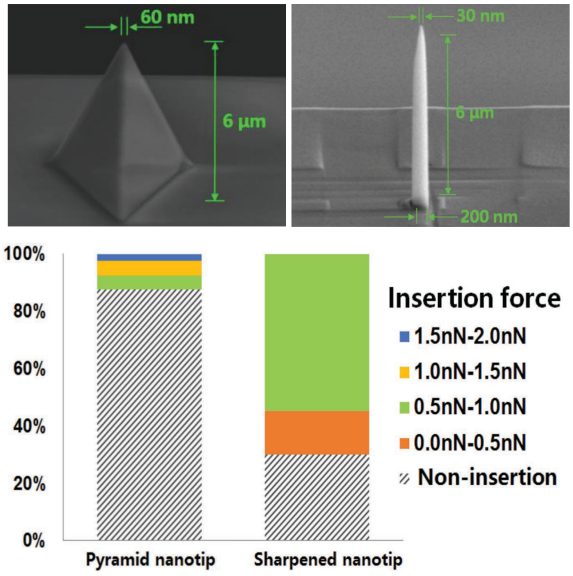

(b) The distribution of the penetration force as a function of probe used (adapted from Fan et al. (2018) [9])

Figure 2.4: Probability of a successful penetration for two AFM probes with different sharpness, including a schematic in (a) and SEM images in (b).

Finally, a study by Penedo et al. (2021b) [42] did extensive research on human cervical cancer cell (HeLa) penetration efficiency for different nanoneedle probes. This study compared several flat and sharp tips with various diameters, measuring the required penetration force and indentation length on HeLa cells. They found that the probability of successful penetration of a thin (200 nm) and flat nanoneedle was 94%, whereas its sharp counterpart was 98%. Next to that, a thicker (400 nm) and flat nanoneedle only had a probability of 70%, and a sharper conical nanoneedle (100 nm at 2 µm from the tip) had a probability of 98%, which is the same as the 200 nm and sharp nanoneedle. Due to their thorough statistical analysis, the spread of the results can be observed. Although the difference in penetration force is slight between flat and sharp tips, the flat-ended tips seem to have twice the amount of spreading compared to the sharp tips. This may suggest that the sharper tips give more reproducible results regarding penetration force.

2.3. Influence of cantilever stiffness

AFM probe fabrication often leads to a variable cantilever stiffness. Thus, the commercial probe specifications are always denoted by a range of cantilever stiffness, such as 0.06-0.12 N/m or even 0.7-9 N/m. Only after the probe is mounted into the AFM machine can the probe be calibrated and the actual cantilever stiffness measured. This may imply that a researcher may do the ”same” experiments with the ”same” cantilever stiffness; however, there is some variability in the stiffness value between different probes. The question that may be posed is if the cantilever stiffness also influences the experimental measurements such as penetration force, indentation depth, force drop and penetration success rate. More importantly, how to choose the best cantilever stiffness for the cell penetration experiment. In this case, ”the best” may be based on minimal damage caused to the cell and how well the penetration event can be monitored through the force-distance curve.

The only study that investigates the effect of cantilever stiffness is by Kwon, Kim & Kim (2009)

[32], and its effect on the penetration force and indentation depth. The stiffness values of the tested cantilevers are 0.26 and 23 N/m for a standard pyramidal AFM probe. The stiffness of the cantilever was observed to affect the penetration force; the stiffer cantilever (23 N/m) showed higher penetration forces and also more spread out, 74.7 $\pm$ 32.6 nN. Whereas the low stiffness cantilever (0.26 N/m) resulted in much lower penetration forces and less spread out, 9.5 $\pm$ 1.4 nN. Furthermore, the indentation depth was much larger for the low-stiffness cantilever (several micrometres) than the stiffer cantilever (several hundreds of nanometers).

The main drawback of this study is that only two stiffness values are tested. What would be more interesting is smaller changes in stiffness values and the effect on the measurements. Additionally, the indentation depth and penetration force should also be minimised; judging from this study, a trade-off between very soft and stiff cantilevers needs to be made.

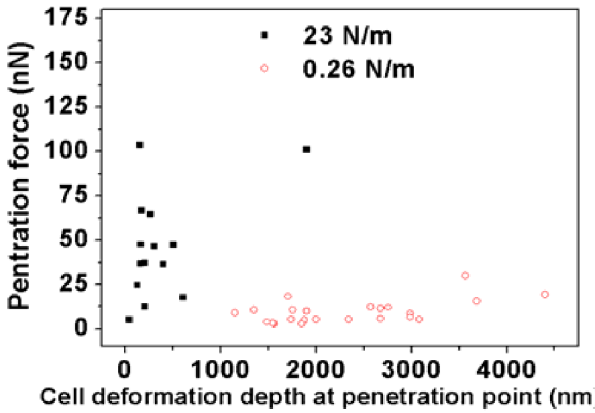

Figure 2.5: Distribution of penetration force and indentation depth (cell deformation) for stiff (23 N/m) and flexible (0.26 N/m) cantilevers (adapted from Kwon et al. (2009) [32]).

2.4. Influence of location of penetration

The cells that the AFM is probing adhere to a rigid substrate, such as glass or plastic, which are far stiffer (GPa range) than the average mammalian cell (1 kPa) [15]. Due to the small thickness of the cell, the rigid substrate underneath will affect the AFM force-distance curves; it makes the cells seem stiffer than they are. Also, the thinner the cell at the probed location, the stiffer it appears to behave. An interesting question may be if this effect also influences the probability of a successful penetration.

Kwon, Kim & Kim (2009) studied the effects of the measurement location on the force-distance curve during penetration experiments using a sharp pyramidal tip on mouse fibroblast cells (L929). The cell was split into the nucleus/centre region (about 4 µm) and the peripheral region (about 500 nm). The force-distance curves of the centre region show a slow force increase after contact (softer behaviour) and a small penetration force (4 nN). Meanwhile, the peripheral region shows a much faster increase in force after contact (stiffer behaviour) and a higher penetration force (20 nN). On the other hand, the cell's heterogeneous nature may result in more random results with respect to location. Other aspects may have more effect on the penetration event, such as if an organelle or filament is present just underneath the membrane. If such structures can be identified beforehand, a preferred location of penetration can be chosen.

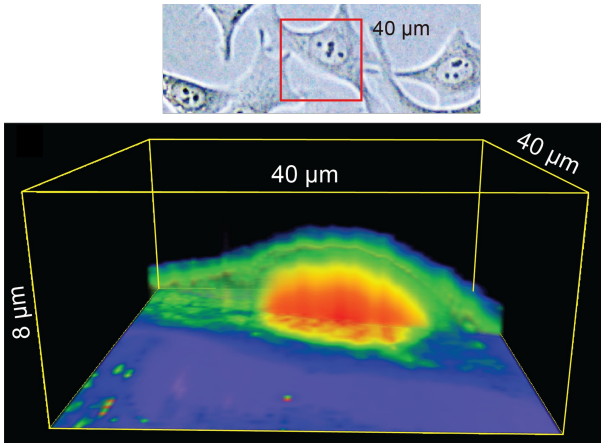

Figure 2.6: 3D map of the HeLa cell enclosed in the red square shown in the SEM image above (adapted from Penedo et al. (2021a) [43]).

Penedo et al. (2021a) [43] use a nanoneedle AFM probe to visualise the internal structures of a living cell. They acquired force-distance curves on many cell locations; this data is then processed to extract the various structures, such as the membrane, actin fibres and the nucleus, in three dimensions. Figure 2.6 shows such a 3D map of a HeLa cell with a colour scale to indicate the stiffer (red) and softer (blue) areas. This technique, however, requires a minimally invasive probe to penetrate the cell many times. Penedo et al. state that the nanoneedle probe should have a diameter below 200 nm and a sharp tip end.

2.5. Influence of tip velocity

Although researchers claim that the cell behaves like a viscoelastic material, the effect of the deformation rate, or insertion rate during penetration, is almost unknown. The FluidFM and AFM papers usually (not always) note the velocity at which the experiments were conducted but without mentioning why this was chosen. Furthermore, across the various papers, the range of velocities is extensive, such that comparisons between results may become disputable. The velocities found range from 0.05 to 1 µm/s for the FluidFM papers, where four out of seven papers did not mention the velocity, and from 0.08 to 20 µm/s for the AFM papers, where two out of eight papers did not mention it. The question that arises is, is the effect of velocity something that can be neglected?

Hategan et al. [26] studied the effect of velocity on the penetration force and indentation depth of erythrocytes (red blood cells), and they found for velocities 1, 8, and 20 µm/s that the penetration force increased exponentially, from an average of 14 to 27 nN. Additionally, the indentation depth also increased with larger velocities. On the other hand, when the indentations are kept small (no penetration), the deformation is observed to behave elastically, independent of the velocity. They, therefore, conclude that the cell behaves elastically for small deformations, and viscous effects only start playing a role for large deformations. For a successful penetration, large deformations are necessary; thus, the viscoelastic behaviour dominates, suggesting that the effect of velocity cannot be neglected.

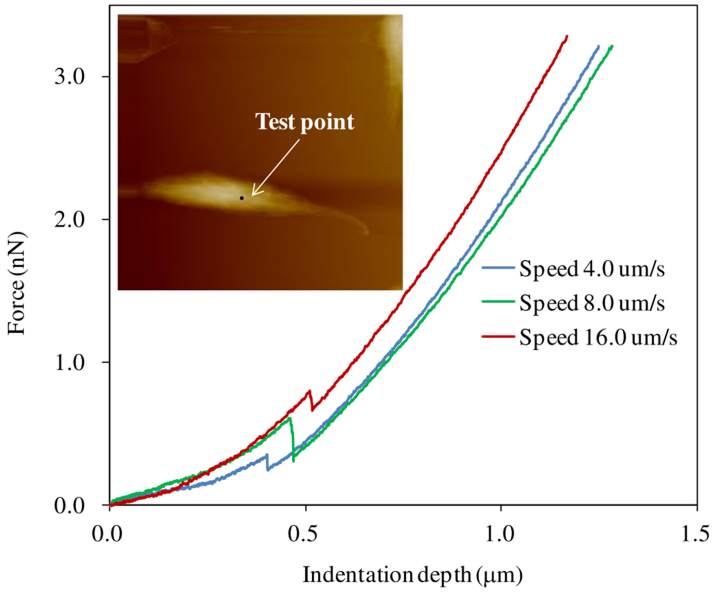

Figure 2.7: Force–distance curves at di□erent velocities on a single location of a mouse fibroblast cell (NIH3T3), see the black point in the image (adapted from Zhang et al. (2018) [52]).

Another paper by Zhang et al. [52] mentions the effect of velocity on the penetration force and indentation depth for velocities 4, 8 and 16 µm/s. They found that the penetration and indentation forces increased with increasing velocity. However, the velocity 8 µm/s showed twice the force drop at the moment of penetration; see Figure 2.7. However, the experiment was carried out in one single NIH3T3 cell, so the confidence level in this trend is deficient.

2.6. Influence of cell stretching

Next to AFM setting parameters and the geometry of the tip and cantilever, other aspects concerning the cell culture may play a significant role. Through simulations of the cell membrane using a molecular dynamics model, Zhang et al. (2018) [52] found exciting results when putting the simulated membrane under strain (stretch). The stretch ratios tested are 0.2, 0.5 and 0.8, and they recorded the force and indentation depth. The results show a decrease in both the penetration force and the indentation depth as the stretch ratio increases.

Later, the same group investigated the effect of stretching actual cells on the penetration force, indentation depth and the probability of a successful penetration [53]. They recognise the low penetration probability of FluidFM tips and the limitation of making the FluidFM tips as small as a nanoneedle tip. Thus, alternative solutions to increasing the penetration probability are explored, such as applying a 'pre-stress' to the cells by stretching the substrate on which they are cultured. The culture dish was fabricated using the material PDMS and imprinted with a micro-groove pattern using soft photolithography. They used NIH3T3 cells and stretched the cells by 0, 5, 10, 15 and 20% strain; at each strain, a sharp pyramidal tip was used to penetrate the cell membrane while recording the force-distance curves. The results show a decrease in the average penetration force (from 2 to 1 nN) and average indentation depth (from 1.2 to 0.2 µm), similar to the simulation. Furthermore, the penetration probability also increased from 19% to 62%; see Figure 2.8.

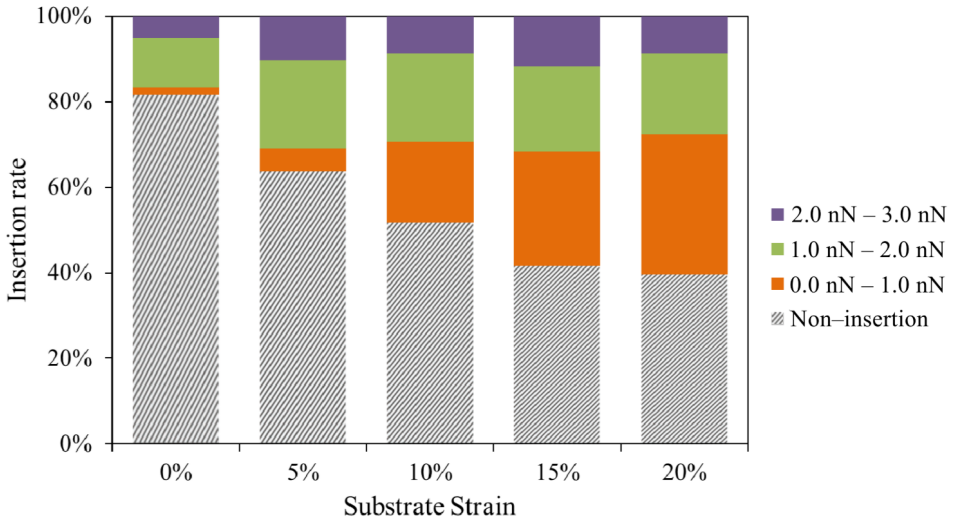

Figure 2.8: Distribution of penetration force as a function of the substrate strain (adapted from Zhang et al. (2023) [53]).

Zhang et al. claim that the pre-stress increases the concentration of stress on the cell membrane at the point of insertion, which reaches the stress fracture threshold much faster and for lower forces [53]. Janshoff (2021) [27] may provide a possible explanation for this phenomenon. He points out that the cell membrane is not elastic and breaks relatively quickly at low forces and indentation depths. However, the membrane has various folds and ruffles to protect the cell that stores the needed stretch. Janshoff refers to this structure as 'membrane reservoirs'. During a penetration event, the mechanics of solely the membrane only come into play at considerable strain due to membrane reservoirs being used up [27]. By stretching the cell, the membrane becomes stretched, and its membrane reservoirs become more used up. As the AFM tip penetrates the cell membrane, the breaking point is reached much faster and at a lower penetration force.

2.7. Discussion

There is a larger pool of literature involving thin nanoneedle-like AFM probes that study the effect of various factors on the cell membrane penetration event. However, a universal definition of what characteristics or quantities determine a successful cell membrane penetration is nonexistent. Table 2.1 summarises the papers found that use an AFM probe for cell membrane penetration experiments. In summary, the penetration success rates are very low for large pyramidal tips, and studies show that tip sharpness, tip diameter and cell stretching can increase the penetration success rate. Furthermore, cantilever stiffness, velocity and penetration location affect the penetration force and indentation depth. However, studies sometimes lack proper statistical relevance due to small sample numbers. Additionally, there is a lack of understanding of the effect of penetration velocity on the penetration success rate.

Table 2.1: Overview of force-distance curve characteristics for different AFM parameters during the penetration of the cell membrane. Cell types are denoted by an acronym, please refer to text. Not mentioned before are: Chon. is chondrocyte, PMC is pleural mesothelial cell, SiHa is a human cervical cancer cell. The material CNT refers to carbon nanotubes. Additionally, h is height of tip, d is diameter of tip, k is the cantilever stiffness, and v the velocity of insertion.

Material	Tip shape	h (µm)	d (nm)	θ (°)	r (nm)	k (N/m)	v (µm/s)	Cell type	Success rate	Penetr. force (nN)	Force drop (nN)	Indent depth (μm)	Refs
Si	Needle	6-8	200-300	0	-	0.1-0.2	-	NHEM, HEK293	-	1	0.3	1	Obataya et al. (2005) [41]
CNT	Needle	1-5	30-40	0	15	0.03-0.08	-	PMC	-	0.1-0.2	0.1-0.2	0.1-0.2	Vakarelski et al. (2007) [50]
Si	Needle	6	200	0	0	0.2	4	hMSC, HEK293	90%	1-2	0.5	1	Han et al. (2008) [25]
Si	Pyramid	17	20	25	10	5	2	SaOs-2	84% (48%)	2.5	0.53	1.2	Bitterli (2012) [29]
Si	Pyramid	16	200	35	100	7	2	SaOs-2	36% (16%)	4.4	0.27	1.4	Bitterli (2012) [29]
Si	Needle	10	300	2	50-150	0.1-1	0.3	HEK293	-	-	-	-	Angle et al. (2014) [1]
Si	Needle	6	30	0.8	15	0.03	2	h-FB	70%	-	-	-	Fan et al. (2018) [9]
Si3N4	Pyramid	6	40	17.5	20	0.03	2	h-FB	13%	1.3	-	0.5	Fan et al. (2018) [9]
Si	Needle	11.8	150	0	10	0.15	0.08	HeLa, SiHa, NIH3T3	87, 84, 90%	5-10	1	-	Song et al. (2020) [48]
Ag2Ga	Needle	7-12	40-200	0	20-100	0.8	20, 10	HeLa, Chon.	-	10, 35	2, 8	1, 1	McCreery et al. (2021) [37]
Si	Needle	10	200	0	15	0.3	10	HeLa	98%	0.17	-	0.645	Penedo et al. (2021b) [42]

3

Modelling of cell membrane penetration

One can take two approaches to optimise the FluidFM probe geometry and the experimental conditions for a high cell membrane penetration efficiency and low forces and indentation depths. The first approach is theoretical, based on simulations, and the other practical, based on experiment observations.

3.1. Theoretical approach

The cell's mechanical behaviour is due to its structure and components with a specific mechanical response, where the main components are the cytoskeleton and the cell membrane. However, a variable factor regulating biological processes and changes in cellular architecture that sustain the cell's survival also plays a significant role in its mechanical behaviour. Research efforts have recently been directed towards a better understanding of these 'direct consequence' and 'regulating' factors. This understanding can explain the behaviours observed in the experiments and form the foundations of theoretical models.

If one considers the cell a material, its properties describe how it would deform (strain) in reaction to an applied stress. A constant usually denotes the relationship between stress and strain; for solid elastic materials, this constant is the Young's modulus. Whereas for fluids, which flow away during the application of stress, the constant is related to the fluid's viscosity [40]. A cell is both elastic and viscous, thus referred to as viscoelastic. Under stress, the cell both stores and dissipates mechanical energy, causing deformation and stress relaxation to increase over time. Typically, the Young's modulus of a cell ranges from hundreds of pascals to tens of kilopascals, and the viscosity is usually hundreds of pascal-seconds [40].

It has been observed that the cytoskeleton largely determines the mechanical properties of the cell. The cytoskeleton is a network consisting primarily of three biopolymers: filamentous actin (F-actin), intermediate filaments and microtubules. Further enhancing the cytoskeleton structure and dynamics are the countless filament crosslinker, motor and regulatory proteins [28]. With increasing applied stress, these networks of semi-flexible biopolymers exhibit an unusual property, namely stress-stiffening; their elastic modulus increases.

One can use mechanical models to characterise the cell's time-dependent and mechanical responses. This enables comparison between cell types, treated and untreated, diseased and healthy cells based on their mechanical response [40]. Researchers have tried different computational models, such as continuum, microstructural, and dissipative particle dynamics models, for the specific application of AFM tip penetration through the cell membrane. Continuum models include simple spring-damper systems to model the viscoelastic behaviour (such as the Maxwell and Kevin-Voigt models) or a power law model. Papers modelled only parts of the membrane [9], or the membrane which encapsulates a fluid [46]. For instance, Rostami & Ahmadian (2023) [46] used finite element analysis (FEA) to simulate the interaction between the cell and a tip. They used a continuum model but included three components: the cell membrane and the actin cortex combined, the nucleus, and the cytoplasm, each having different material models and properties. However, the point of failure was based on the Von Mises stress at a predefined value. The difficulty with these continuum models is replicating the point of fracture, and even if this can be reproduced, it cannot explain why this occurred.

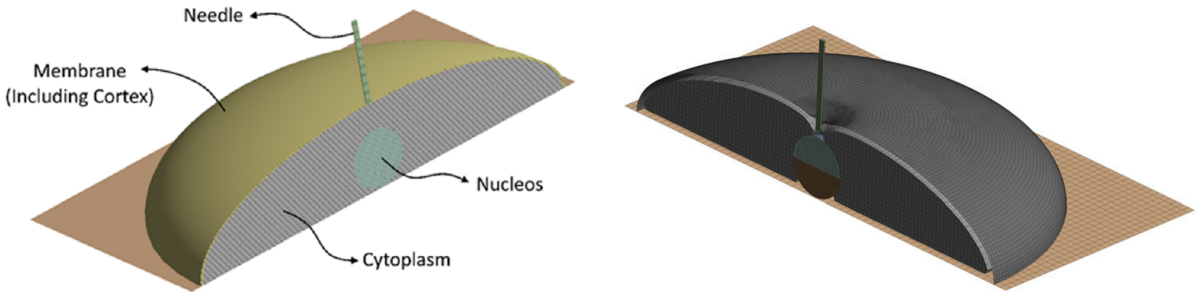

(a) The model geometry and components.

(b) Simulation of the penetration.

Figure 3.1: A finite element approach to modelling the cell (adapted from Rostami & Ahmadian (2023) [46]).

Tensegrity is also used; this is a microstructural model replicating the cell's different components and how they work together [2, 53]. For example, Zhang et al. (2018) use a tensegrity to model the cell membrane, actin filaments and stress fibres to test the effect of 'pre-stress' on the penetration threshold, see Figure 3.2. The disadvantage of these empirical models is that they cannot relate the measured behaviour to the actual structural and biological state of the cell, thus it cannot predict changes in behaviour if the cell changes state.

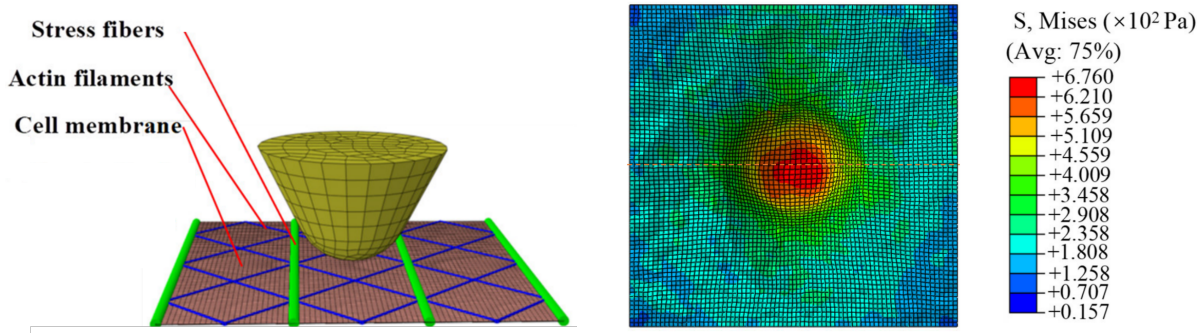

(a) The placement of the cell membrane actin filaments and stress fibres.

(b) The stress distribution of the cell membrane under the indentation depth of 100 nm

Figure 3.2: A tensegrity model of the cell membrane to measure deformation and Von Mises stress (adapted from Zhang et al. (2023) [53]).

An alternative model is called dissipative particle dynamics or molecular dynamics, where particles represent a whole molecule, such as a phospholipid, and have a hydrodynamic interaction. The dynamics between two particles are governed by Newton's equations of motion [52, 36]. Forces between two particles consist of conservative, dissipative and random forces. Zhang et al. (2018) [52] were able to model the penetration of a rigid ball through a lipid bilayer; this can be seen in Figure 3.3. However, extensive comparison to experimental data is lacking; therefore, how well the model reproduces reality remains unknown.

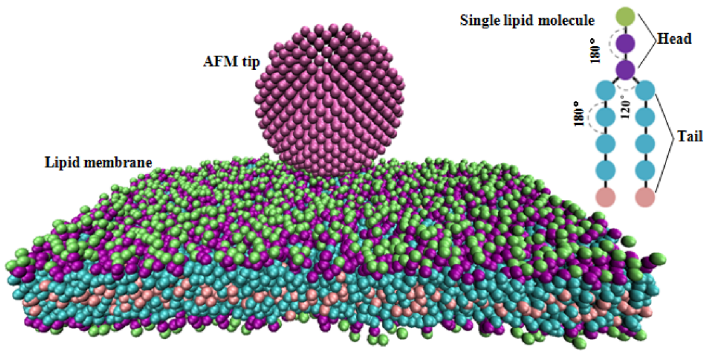

(a) The hydrophilic lipid beads (head) and hydrophobic lipid beads (tail) are presented in a single lipid molecule.

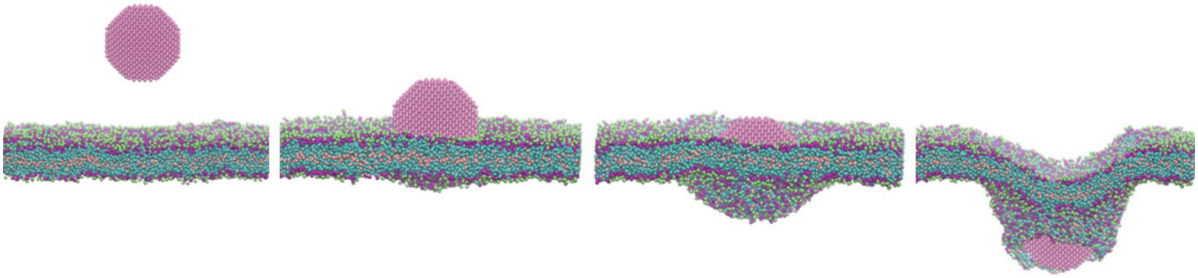

(b) The process of the AFM tip penetrating the cell membrane, moving from the initial stage to the contact stage, bending stage and penetration stage.

Figure 3.3: Schematic of the interaction between the AFM tip and lipid membrane (adapted from Zhang et al. (2018) [52]).

Other models include, soft glassy rheology (SGR) which considers the cytoskeleton as a soft glassy material [12], the cell as a dynamic network of polymers, and biphasic models based on poroelasticity, which are all reviewed in the paper by Moeendarbary & Harris (2014) [40]. However, these have not yet been used for a tip penetrating the cell membrane. Furthermore, it is essential to realise that all these theories lack a unifying theory that can explain all the complexities encountered with cell mechanics.

3.2. Experimental approach

The cell is a living organism; thus, modelling its behaviour in response to certain stimuli becomes highly complex. In this case, collecting and analysing large numbers of data to find relationships may be of greater significance when designing a FluidFM probe. This approach is difficult because one can only test one variable at a time while keeping all others as control variables. This means that the researcher will have to conduct many experiments if many variables have to be tested. Furthermore, it is assumed that the variables are independent of one another; thus, it is overlooked if there is dependence between variables, and the full scope of possibilities is not obtained. Additionally, it is sometimes not possible to control all other variables, such as temperature and humidity. In the case of AFM and FluidFM, the cantilever stiffness and tip radius (sharpness) may vary slightly between probes.

Design of Experiments (DOE) has become more popular in various research fields and addresses these issues. DOE is a mathematical approach used for designing and conducting experiments, and analysing the obtained data [7]. It is often utilised in a system with multiple input variables X's (influencing factors), which may affect a measured response variable Y (penetration force, indentation depth, probability of a successful penetration). This method allows for multiple variables to be tested simultaneously, either due to time constraints, sample number limitations, or just because it is impossible to control all variables. The statistical background is given in the paper Durakovic (2017) [7].

Machine learning can accompany DOE, as the data can be used to train an algorithm to make predictions for the force-distance curve. A paper by Rajabifar et al. (2022) [45] has shown a machine learning approach to characterise the mechanical and adhesive properties of soft viscoelastic polymers tapping mode AFM. First, the algorithm is developed to predict the force-distance curves for a known set of AFM operating conditions, including the cantilever parameters and the viscoelastic sample with known material and adhesive properties. Second, the algorithm is used for a parametric study to predict

variations in the force-distance curves because of changes in the operating conditions or the material. After, the machine learning algorithm is implemented in experiments of polymer samples, where the estimated mechanical properties agree well with the actual material properties.

3.3. Discussion

In literature, the modelling or theoretical approach has been used to design their AFM penetration experiment in such a way as to improve the cell membrane penetration success rate. A great example is Zhang and co-workers' molecular dynamics model [52] and later their tensegrity model [53] to show the influence of stretching the membrane on the penetration success rate of a tip through a cell membrane. However, developing such a model with sufficient accuracy and complexity is a whole research project on its own; thus, many others take the more practical and experimental approach. For instance, Penedo et al. (2021b) [42] conducted various experiments while changing tip diameter, AFM operating mode (contact vs. dynamic), and tip sharpness to identify which parameters affect the cell membrane penetration success rate. The advantage is that the results represent real data and not some estimated result produced by a model. As this project works with living cells, and a theoretical model will never capture its full complexity, an approach based purely on experimental data may result in more valuable and applicable conclusions. On the other hand, the researcher must be aware that the experiments must be well designed and conducted (such as using DOE), acquire high sample numbers and use the correct statistical methods to analyse the data. It is important to make decisions with a higher confidence level and avoid bias and errors due to assumptions (such as assuming a normal distribution when it usually is not).

4

Conclusion

This literature study presented how AFM and FLuidFM have contributed to single-cell analysis methods. Especially appealing is the potential of extracting subcellular components for subsequent analysis, which was only possible recently in 2016. AFM's great advantage is the force feedback, plotted in a force-distance curve, which can (ideally) indicate the moment of penetration due to a sudden force drop experienced by the tip. Although this sounds promising, many technical challenges still need to be solved. For instance, the large forces (>20 nN) required to penetrate the cell membrane can cause irreversible damage. Furthermore, the large indentation depths, which usually reach half of the cell height, significantly reduce the spatial resolution when targeting a specific subcellular component. Most importantly, the reproducibility of results is extremely low, mainly due to the natural cell-to-cell variability but also due to the low cell membrane penetration success rate. This success rate for the typical FluidFM probes is usually around 13%, mainly owing to the large size of the FluidFM probe. With the rise of two-photon polymerisation printing of AFM and FluidFM probes, new designs can be explored to improve the success rate and large penetration force and indentation depth.

An important question may arise: what is the best tip design for cell membrane penetration? This study examined papers on cell membrane penetration mechanics using AFM and which factors influence the penetration event. The factors that have the most effect are AFM tip geometry, tip sharpness and cell stretching. However, other factors, such as cantilever stiffness, location of cell membrane penetration, and tip velocity, have been shown to have an effect but have been insufficiently researched. Additionally, most papers lack proper statistical analysis due to low sample numbers and changing independent variables simultaneously, causing low confidence levels and an inability to conclude the influence of just one factor.

Modelling cell membrane penetration can assist in optimising the FluidFM probe and the experimental conditions. Furthermore, it can predict the cell's response to specific settings or local cell stiffness. There are two approaches to achieve this: through theoretical models to obtain simulations of the penetration event or through actual experimental data. The theoretical approach has been successfully used to improve the cell membrane penetration success rate. Other models found are based on continuum mechanics, which usually involve a soft elastic membrane filled with a fluid; however, simulating the actual cell membrane penetration is difficult. Alternatively, the experimental approach is more commonly used, as the results are based on actual data. To assist in conducting proper and efficient experiments, the Design of Experiments can be employed, but the researcher must also use correct statistical analysis and acquire large sample numbers to avoid wrong conclusions.

By achieving higher reproducibility, spatial control, and possibly sampling automation, the FluidFM can make an immense impact, enabling precise injection or extraction into or from the cell with minimal invasiveness. Pushing the limits of single living cell analysis techniques to new heights and contributing to understanding the complex system that the cell is, which plays a central role in all life.

5

Research proposal

5.1. Research goal

The goal of this research is to employ the force feedback of the atomic force microscope for guidance and monitoring cell membrane penetration.

> *How to reproducibly and quantifiably monitor cell membrane penetration events using microfluidic probe force spectroscopy?*

This question will be the overarching theme of this research. In the process, some useful sub-questions are posed:

i. What is the influence of AFM tip velocity and location of cell membrane penetration?
ii. What is the optimal tip geometry and cantilever stiffness for cell membrane penetration?
iii. How can the optimal tip geometry and cantilever stiffness be integrated in a microfluidic force probe?

After the effects of AFM experimental conditions (tip velocity and location of cell membrane penetration) and AFM probe (tip geometry and cantilever stiffness) have been quantified, a 'milestone' is achieved, a result to fall back on if the next step fails. Upon reaching the milestone, the following steps can be taken to decide how to integrate the findings with a microfluidic cantilever.

5.2. Research plan

5.2.1. Phase 1: Defining reproducibility and quantifiability

Before beginning to find the AFM system parameters that influence the reproducibility and quantifiability of a cell and nuclear membrane penetration events, it is important to define the terms reproducibility and quantifiability for such an event. Reproducibility refers to the consistency of repeated measurements, and quantifiability refers to the quality of being measurable. Initial data on HeLa cell penetration using a standard AFM probe can be utilised to analyse the quantifiability of a successful penetration event by identifying characteristics that we can measure and quantify. The reproducibility can be quantified based on these measurable characteristics between repeated experiments.

To collect this initial data, a suitable AFM probe needs to be designed and fabricated; this marks the first step of the research project. A first design is proposed based on the nanoneedle-like probes mentioned in the literature review since they have a higher probability of successful penetration. In addition, they typically require lower forces to penetrate the cell and nuclear membrane, thus minimising cell damage and allowing for repeated measurements on the same cell. An additive manufacturing method, namely two-photon polymerisation (2PP), is also proposed to print the needle-like AFM tip onto a commercial tipless cantilever.

The experiment will employ force spectroscopy while inserting and retracting a cylindrical needle-like AFM tip into HeLa cells adhered to a rigid substrate, which is repeated in multiple locations on the same and different cells to obtain as many force-distance curves as possible. In parallel, optical images will be taken from the side to visualise and validate if penetration of the cell membrane was successful; these images can be compared to their force-distance curve. If visualisation is unclear through the optical microscope, fluorescent microscopy may be employed. Moreover, the experiment will be designed such that the effect of tip velocity and location of penetration on the penetration event can be simultaneously studied.

The data will be analysed using Python or Matlab, and an effort will be made to automate the process. Quantities that describe the peak phenomena sometimes seen during a successful penetration event can be identified, such as indentation depth, force drop, penetration force, and slope of the curve before and after. A code will be written to measure these quantities when inputting a force-distance curve automatically. Through manually set thresholds, the code can classify the force-distance curves into successful and unsuccessful penetration events. This code can then be used as a data analysis tool for all future experiments in my research project, as well as other projects that have to deal with cell or nuclear membrane penetration.

Fabrication of needle AFM tip

To successfully fabricate a needle-like AFM tip using 2PP, a protocol must be established that is unique to the geometry, size and substrate to which it must adhere. An initial design of the tip is made using the computer-aided design (CAD) software SolidWorks. This initial design can then be printed with varying diameters on a commercial tipless cantilever; see Figure 5.1. To start, the design with the largest diameter will be printed to see if printing on cantilevers is possible and with what printing parameters. If successful, printing the design with smaller and smaller diameters can be attempted. Furthermore, the height of the tip in the initial design is 6 µm but may be varied according to the height of the cell.

Further analysis is necessary to assess the axial and lateral stiffness of the tip since the Young's modulus of the polymer is much lower (□1 GPa) than the traditional silicon tip (□165 GPa). This will be done through COMSOL simulations beforehand and through experiments after fabrication by probing a rigid surface. Through these simulations and experiments, the axial and lateral stiffness and the maximum loading force can be used to avoid damage to the tip and possibly correct for the deflection of the tip during single-cell experiments.

Additionally, the printed structures should be observed using a scanning electron microscope (SEM) to check for faulty printing and measure its dimensions, which may not be precisely equal to the CAD drawing.

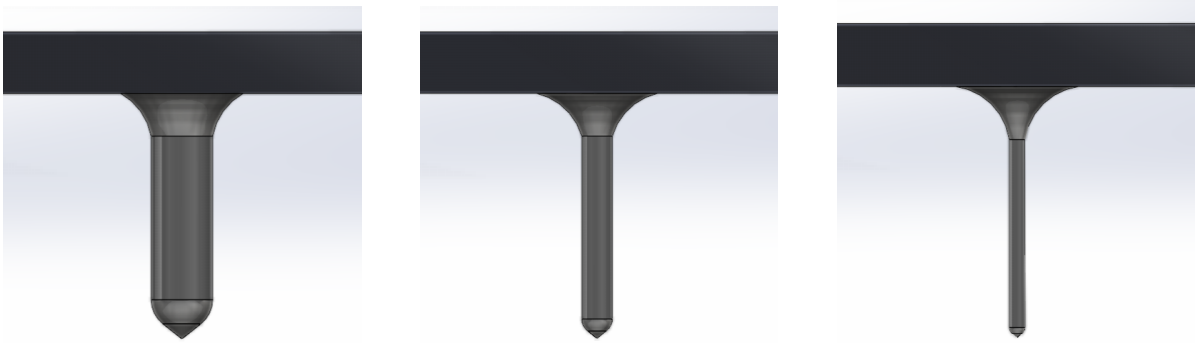

(a) 2 µm (b) 1 µm (c) 500 nm

Figure 5.1: Initial design of needle AFM tip with a height of 6 µm and large (a), medium (b) and small (c) diameters.

HeLa cells

The HeLa cell line, derived from cervical cancer cells, is the oldest human cell line and, thus, also the most commonly used in cell biology research. Most papers on single-cell manipulation, injection, and extraction using AFM or FluidFM use HeLa cells for their experiments. This makes for strong comparisons between the results of this thesis project and other results due to the large amount of data available. Moreover, the results may contribute to the broad range of research on HeLa cells, especially towards cancer research.

Tip velocity

To study the effect of AFM tip velocity during insertion and retraction, an experiment is proposed where force spectroscopy is employed while the tip is inserted in and retracted from HeLa cells adhered to a rigid substrate at different velocities. The velocities tested will be the full range of the AFM system, starting around 500 nm/s; anything lower will require fixing the data acquisition noise; otherwise, it will be down to 50 nm/s. The maximum velocity of the AFM system is about 100 µm/s, but from the literature, the most used velocities lie below 20 µm/s. To cover the large range of velocities, from 0.05 to 100 µm/s, an equidistant sampling (increment 1 µm/s) is chosen between 1 and 20 µm/s, and only several sampling points are chosen at very low and high velocities such as 0.05, 0.1, 0.5, 50 and 100 µm/s. The insertion location on the cell should be kept the same to be compared. Hence, two locations are chosen: above the centre of the nucleus and the cytoplasm, halfway between the plasma and nuclear membrane.

The data will be used to define reproducibility and quantifiability, and the code will be written to analyse a large number of force-distance curves automatically. The code will quantify the peak phenomena and whether the penetration was successful or not. Using this information, plots can be made that compare a change in velocity to any of these quantities or probability of success. The relationships can be studied, and an effort can be made to propose an explanation for a particular relationship or lack thereof. If an optimal velocity can be found, this can be used as the default setting for all further experiments.

Location of cell membrane penetration

When comparing velocities, the location of cell membrane penetration may also play a role; therefore, this effect should also be studied. The aim is to find if there are locations that are more favourable for reproducible and quantifiable membrane penetration events. For this, another experiment is proposed to employ force spectroscopy in QI mode, still fully inserting the tip to penetrate the membrane(s) to obtain a force-distance curve at many locations on the cell.

No two cells look alike; therefore, a method is proposed to compare the 'location' between different cells. A simple way would be to use height as an indicator for location, as the highest point is probably the centre of the nucleus, and this height gradually becomes zero as you move away from the nucleus. Moreover, the cell's height at the location can be easily extracted from the force-distance curve as the height at which the curve shows its first slope increase. However, the height between cells also differs; thus, to compare the location between cells, the height can be normalised using their maximum height;

see Equation 5.1 and Figure 5.2.

$$h_o = 0 \qquad h = \frac{h_{sample}}{h_{max}} \tag{5.1}$$

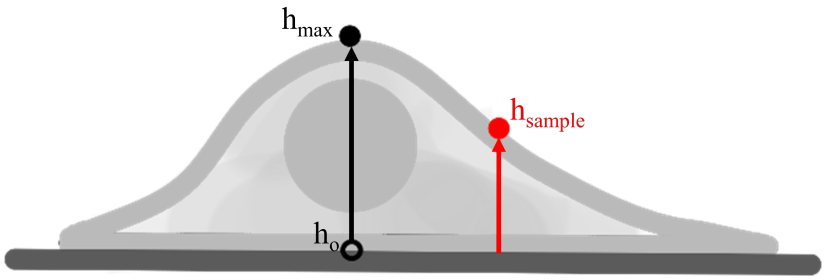

Figure 5.2: Normalised height with respect to the maximum height of the cell, as an indicator for the location of cell membrane penetration.

Alternatively, the location can be compared through the distance from the centre of the nucleus; see Figure 5.3. This distance can also be normalised with respect to the size of the nucleus; see Equation 5.2. This distance may also be extracted from the data, as we know which force-distance curve corresponds to which data point. The distance between a data point and the data point corresponding to the centre of the nucleus can be calculated if we know the distance between two neighbouring data points (which we should as it is chosen beforehand in the QI mode settings).

$$d_o = 0 \qquad d = \frac{d_{sample}}{d_{nucleus}} \tag{5.2}$$

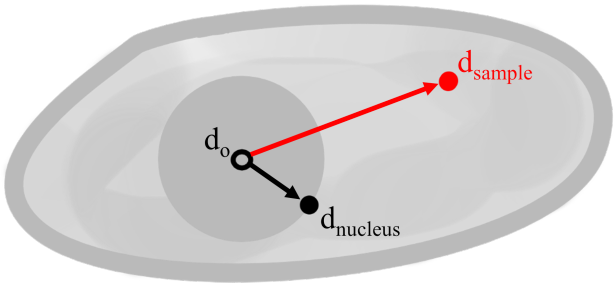

Figure 5.3: Normalised distance from the centre of the nucleus w.r.t. the nucleus radius, as an indicator for the location of cell membrane penetration.

Additionally, the initial indentation slope, or stiffness of the cell during indentation, can be used as a rough indicator for location because the nucleus is stiffer than the cytoplasm. Even if this is a 'rough' indicator, it may have a higher correlation with the reproducibility and quantifiability of a penetration event.

To summarise, the force-distance curves will be analysed the same way as for the velocity experiments; however, in this case, they do not compare a change in velocity, but instead a change in distance from the centre of the nucleus, height and stiffness measured during initial indentation. Due to the high number of data points per cell, an image or map can be created for visualisation purposes.

5.2.2. Phase 2: Effect of AFM probe properties

This second phase involves the study of the effect of AFM probe properties, such as the tip's geometry and the cantilever's stiffness, on the penetration event's reproducibility and quantifiability. Correspondingly, several new AFM probes will need to be fabricated, again by 2PP, to accommodate for different tip geometries and cantilever stiffness to be tested. To study these individual factors, it is important

only to change one variable while keeping the rest constant and collecting enough data for statistical relevance.

Initial designs for the different tips and cantilever stiffness are proposed based on AFM probes used in the literature and on what is within the limits of 2PP fabrication. As before, the cantilevers will be bought as commercial tipless cantilevers, and thus, several with different stiffness can be chosen.

The experiments will employ force spectroscopy while inserting and retracting the different AFM probes into HeLa cells adhered to a rigid substrate, which is repeated in multiple locations on the same and different cells to obtain as many force-distance curves as possible. The code written in phase 1 can then be used to automatically measure the quantities that describe the peak phenomena and classify the force-distance curves into successful and unsuccessful penetration events. Once all the quantities are extracted, they can be compared to the tip geometries and cantilever stiffness that they correspond to.

The aim is to find the effect of changing the tip geometry and cantilever stiffness on the reproducibility and quantifiability of cell and nuclear membrane penetration events and determine if there is an optimal tip geometry and cantilever stiffness. These results may then be integrated into the design of a microfluidic cantilever.

Fabrication of AFM tips with different geometries

Several factors make up the geometry of an AFM tip, for instance, shape, length, base diameter, half angle, and tip radius. The literature shows that diameter and tip radius affect the penetration event. In this case, the length of the tip is chosen to be slightly larger than the height of a cell so that the complete cell, at any location, can be penetrated until the substrate underneath. For different geometries, the conical and cylindrical shapes are chosen (see Figure 5.4), where the diameter is also varied for the cylindrical tip.

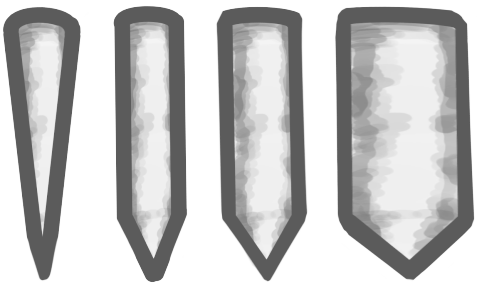

Figure 5.4: AFM tip geometries that will be studied, conical and cylindrical, and different diameters.

The tip radius refers to the 'sharpness' of the tip apex; this may be in the range of 10 nm (very sharp) to several 100 nm (blunt) or even zero (flat end). When varying the tip radius, the shape and diameter of the tip must remain constant; therefore, a cylindrical (needle-like) tip with a diameter of 500 nm (or, if not possible, 1 µm) is chosen as the default, see Figure 5.5.

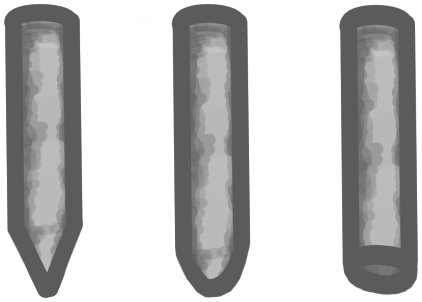

Figure 5.5: Cylindrical AFM tip with varying tip radius (sharpness), from very sharp to flat.

The diameter of the AFM tip can be studied by using the default cylindrical tip, as it is more straightforward than the 'diameter' of a pyramidal or conical tip. Since the protocol to fabricate the cylindrical

tips with varying diameters has already been explored in phase 1, this would also take less time to repeat.

Fabrication of AFM tips on different stiffness cantilevers
Besides tip geometry, the stiffness of the cantilever also plays an essential role in the penetration event. Since it decides the amount of flexibility of the cantilever and, subsequently, the amount of force it will exert on the cell. The stiffness also affects the sensitivity and the noise of the measurements; a lower stiffness increases the sensitivity but also improves the noise, and thus, a certain compromise needs to be struck (high sensitivity and low noise). Usually, the cantilever stiffness is chosen to be similar to the cell stiffness; however, in the literature, this seems to vary drastically when subjected to different tip geometries and AFM experimental conditions, such as velocity and location of penetration.

To obtain probes with different cantilever stiffness, several commercial tipless cantilevers can be used, and the same tip can be printed at the end, or the complete cantilever and tip are printed, where the cantilever dimensions are altered to change the stiffness. The latter, however, is a challenging and time-consuming extra step in the fabrication process; this approach will only be resorted to if the former is lacking or fails. Stiffness values from the literature are usually in the range of 0.1 to 0.8 N/m; however, values such as 0.03 and 7 are also encountered. Therefore, a suitable set of stiffness to be tested is 0.05, 0.1, 0.5, 1, 5 and 10 N/m, or in a similar order of magnitude.

5.2.3. Phase 3: Integration with microfluidic cantilever

To reach the research goal, the findings from phase 2 should be integrated into the design of commercial microfluidic cantilevers so that cell biopsy can be realised using force feedback. To assess to what extent the optimal tip geometry and cantilever stiffness can be applied to microfluidic cantilevers, such a probe's design requirements must first be identified. For example, the minimum diameter of the microfluidic channel, minimum/maximum aperture size, and minimum stiffness of the hollow cantilever due to limitations in dimensions.

After the design requirements are defined, the more optimal geometry for the AFM tip in a penetration event can be included in the design of a microfluidic cantilever and tip. This may result in one or multiple designs for a new microfluidic probe. Next, the designs can be made ready for 2PP printing and altered slightly if necessary. The idea is to buy commercial tipless microfluidic cantilevers from Cytosurge (see Figure 5.6); these have available stiffness 0.3, 1, 2 and 4 N/m, and then print the tip design with an aperture on top of the aperture of the cantilever. If this is not possible, then fully printed probes will be considered.

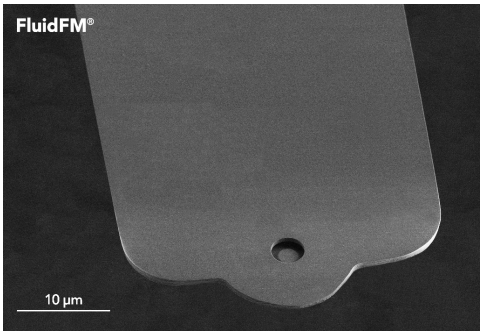

Figure 5.6: Cytosurge, MAT FluidFM Micropipette [**Cytosurge.**]

After their fabrication is successful and the microfluidic channel is working, their performance can be evaluated through force spectroscopy experiments on HeLa cells adhered to a rigid substrate. The acquired force-distance curves can be analysed for quantifiability and reproducibility, and subsequently compared to commercial FluidFM probes, either from literature or our experiments.

5.3. Planning

5.3.1. Milestones

Milestone 1: To conduct the cell membrane penetration experiments, fabricating the needle AFM tip on commercial AFM cantilevers is necessary. Preferably using two-photon polymerisation or focused-

ion beam etching or deposition. The successful fabrication of different tip geometries and cantilever stiffness will lead to the achievement of this milestone. To confirm success, the printed tips will be observed using scanning electron microscopy images to check the quality of the structure and if the dimensions are correct. Furthermore, the stiffness of the cantilevers can be checked using the AFM cantilever calibration method.

Milestone 2: The terms 'reproducibility' and 'quantifiability' are defined in quantities that can be measured/extracted from the force-distance curves. Furthermore, the thresholds for those quantities mark the dividing line between a successful and unsuccessful penetration event. The effect of velocity, location of penetration, tip geometry, and cantilever stiffness are experimentally studied, and their data analysed for reproducibility and quantifiability of the penetration event. This milestone will be achieved when at least one force-distance curve shows the ideal properties.

Milestone 3: This marks the completion of a successful fabrication of a new FluidFM design, which can be confirmed through scanning electron microscopy images and cantilever stiffness calibration method offered by the AFM. To test if the FluidFM operates, fluid can be inserted, and an overpressure applied using a pressure controller. If the fluid is ejected from the tip aperture and nowhere else, it operates and does not leak. To evaluate its performance on its reproducibility and quantifiability of a cell membrane penetration event, the force-distance curves acquired are compared to those of a commercial FluidFM probe. If the quantifiability and reproducibility improve, then this milestone is achieved.

5.3.2. Gantt chart

The current time planning for this research project is presented in the Gantt chart in a simplified version in Figure 5.7 and in full detail in Figure 5.8.

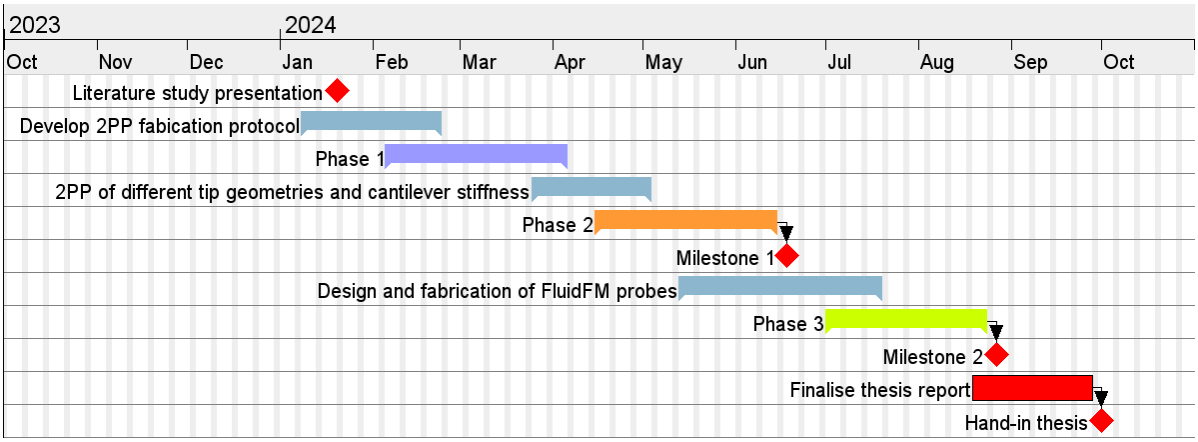

Figure 5.7: Simplified Gantt chart.

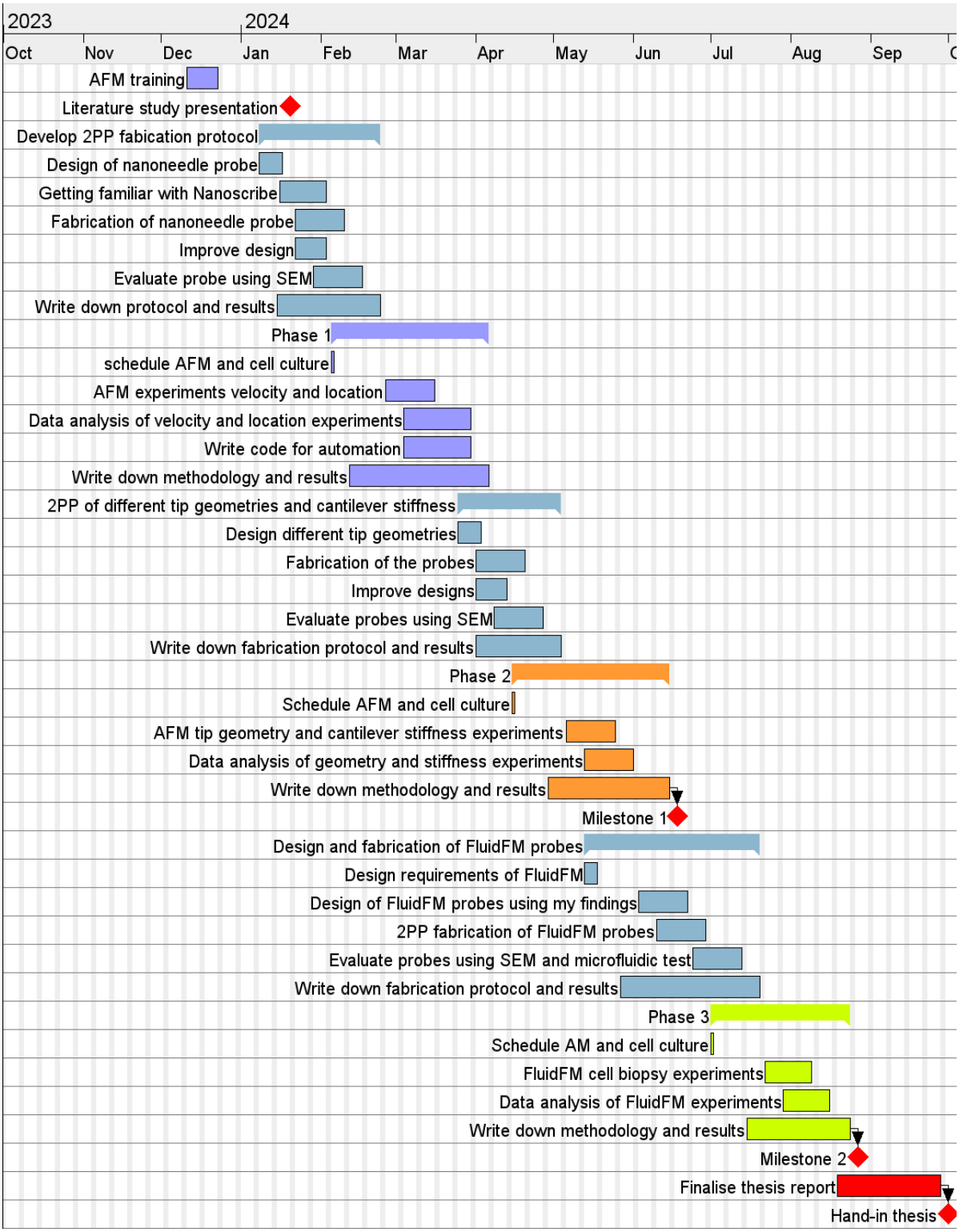

Figure 5.8: Time planning in a Gantt chart.

5.4. Risks and mitigations

This section provides an overview of possible risks involved in the thesis project, their risk score (S) calculated by multiplying the probability (P) and impact (I) scores, and mitigation strategies to prevent these risks from occurring, see Table 5.1

Table 5.1: Risk and mitigation overview, with probability (P) and impact (I) are ranked 1=low and 5=high, and the risk score (S) is PxI

Risk description	Risk cause	Mitigation strategy	P	I	S
2PP fabrication					
Desired sharpness of AFM probe is not possible	Due to resolution limitations of 2PP	Look at possibility of FIB milling to sharpen polymeric probe or buy commercial sharp AFM probes	3	1	4
Printing a nanoneedle probe on a tipless cantilever is a challenge itself and becomes time-consuming	Due to the many printing parameters that have to be optimised with trial and error, and there is limited availability of the 2PP machine	Continue with the process of fabricating the probes, however already start phase 1 experiments with a commercial pyramidal probe	3	2	6
The cantilever plastically deforms during the printing process	The resin droplet exerts high forces om the cantilever, it is weighed down	Make a holder for the cantilever which reduces the distance between the base of the resin droplet and the cantilever, the amount of resin can then also be reduced	2	4	8
Polymerization is incomplete in some areas	Due to the resin droplet not being contained and flowing away from those areas	Make the setup such that the resin droplet is contained around the complete cantilever to ensure that the resin is present at the polymerisation site	2	2	4
Printed tip separates from cantilever surface	Due to contact surface area being too small, or the interface not being found correctly, or the cantilever surface being too hydrophilic	Increase the base area of the design of the tip, could add a silane to the surface of the cantilever for better adhesion (hydrophobic), and properly plasma clean the cantilever beforehand	4	3	12

Risk description	Risk cause	Mitigation strategy	P	I	S
Phase 1					
Cell death during penetration experiments which may cause anomalous data	Penetration of the cell membrane sometimes requires high forces and thus may cause lethal damage to the cell	Use an optical or fluorescent microscope to take images before, in between, and after experiments to check which cells are dead, also take note what data correspond to what cell	3	3	9
AFM probe breaks during experiments	Due to accidentally crashing it into the hard substrate, applying forces from the side, or the mechanical strength of the tip is not high enough	Fabricate multiple of the same probes, also fabricate some that are slightly larger in diameter in case the thinner ones fail	3	5	15
No peak phenomena observed in force distance curves	This may be due to the geometry of the tip or the stiffness of the cantilever, or other unknown causes	Try to find other characteristics of the curve that could identify the penetration event, or redo the experiments with different tip geometry and/or cantilever stiffness	3	1	3
Phase 2					
No trend can be extracted from data	There is no trend or sample size is too small	Increase the sample size and thus more time needed for experiments	4	1	4
Phase 3					
Results for tip geometry and cantilever stiffness are inapplicable to the FluidFM probe	Due to design requirements of the microfluidic channel or fabrication limitations.	Results are still results, define a threshold below where the geometry or velocity could play a role. Other factors could be explored, however with time may not be realistic	3	1	3

Bibliography

[1] Matthew R. Angle et al. “Penetration of cell membranes and synthetic lipid bilayers by nanoprobes”. In: *Biophysical Journal* 107 (9 Nov. 2014), pp. 2091–2100. ISSN: 15420086. DOI: 10.1016/j.bpj.2014.09.023.

[2] Sara Barreto et al. “A multi-structural single cell model of force-induced interactions of cytoskeletal components”. In: *Biomaterials* 34 (26 Aug. 2013), pp. 6119–6126. ISSN: 01429612. DOI: 10.1016/j.biomaterials.2013.04.022.

[3] Hans Jürgen Butt, Brunero Cappella, and Michael Kappl. “Force measurements with the atomic force microscope: Technique, interpretation and applications”. In: *Surface Science Reports* 59 (1-6 2005), pp. 1–152. ISSN: 01675729. DOI: 10.1016/j.surfrep.2005.08.003.

[4] L. Chen et al. “Millifluidics, microfluidics, and nanofluidics: manipulating fluids at varying length scales”. In: *Materials Today Nano* 16 (Dec. 2021). ISSN: 25888420. DOI: 10.1016/j.mtnano.2021.100136.

[5] Wanze Chen et al. “Live-seq enables temporal transcriptomic recording of single cells”. In: *Nature 2022 608:7924* 608 (7924 Aug. 2022), pp. 733–740. ISSN: 1476-4687. DOI: 10.1038/S41586-022-05046-9. URL: https://www-nature-com.tudelft.idm.oclc.org/articles/s41586-022-05046-9.

[6] Yves F. Dufrêne et al. “Imaging modes of atomic force microscopy for application in molecular and cell biology”. In: *Nature Nanotechnology* 12 (4 May 2017), pp. 295–307. ISSN: 17483395. DOI: 10.1038/nnano.2017.45.

[7] Benjamin Durakovic. “Design of experiments application, concepts, examples: State of the art”. In: *Periodicals of Engineering and Natural Sciences* 5 (3 Dec. 2017), pp. 421–439. ISSN: 23034521. DOI: 10.21533/pen.v5i3.145.

[8] Peter Eaton and Paul West. *Atomic Force Microscopy*. Oxford University Press, Mar. 2010.

[9] Na Fan et al. “The Insertion Mechanism of a Living Cell Determined by the Stress Segmentation Effect of the Cell Membrane during the Tip–Cell Interaction”. In: *Small* 14 (22 May 2018). ISSN: 16136829. DOI: 10.1002/smll.201703868.

[10] Maria Farsari and Boris N. Chichkov. “Materials processing: Two-photon fabrication”. In: *Nature Photonics* 3 (8 Aug. 2009), pp. 450–452. ISSN: 17494885. DOI: 10.1038/nphoton.2009.131.

[11] Cécile Formosa-Dague et al. “Zinc-dependent mechanical properties of Staphylococcus aureus biofilm-forming surface protein SasG”. In: *Proceedings of the National Academy of Sciences of the United States of America* 113 (2 Jan. 2016), pp. 410–415. ISSN: 10916490. DOI: 10.1073/pnas.1519265113.

[12] Jeffrey Fredberg and Ben Fabry. “The cytoskeleton as a soft glassy material”. In: *Cytoskeletal Mechanics: Models and Measurements in Cell Mechanics* (2006). Ed. by Mohammad R. K. Mofrad and Roger D. Kamm, pp. 50–70.

[13] Christoph G. Gäbelein et al. “Mitochondria transplantation between living cells”. In: *PLoS Biology* 20 (3 Mar. 2022). ISSN: 15457885. DOI: 10.1371/journal.pbio.3001576.

[14] Christoph Georg Erich Gäbelein. “Single cell engineering using fluidic force microscopy”. In: (2021).

[15] Pablo D. Garcia, Carlos R. Guerrero, and Ricardo Garcia. “Nanorheology of living cells measured by AFM-based force-distance curves”. In: *Nanoscale* 12 (16 Apr. 2020), pp. 9133–9143. ISSN: 20403372. DOI: 10.1039/c9nr10316c.

[16] Ricardo Garcia. “Nanomechanical mapping of soft materials with the atomic force microscope: Methods, theory and applications”. In: *Chemical Society Reviews* 49 (16 Aug. 2020), pp. 5850–5884. ISSN: 14604744. DOI: 10.1039/d0cs00318b.

[17] Ayoub Glia, Muhammedin Deliorman, and Mohammad A. Qasaimeh. “3D Generation of Multipurpose Atomic Force Microscopy Tips”. In: *Advanced Science* 9 (27 Sept. 2022). ISSN: 21983844. DOI: 10.1002/advs.202201489.

[18] Ayoub Glia, Muhammedin Deliorman, and Mohammad A. Qasaimeh. “FluidTIP for High-Resolution Imaging and Enhanced Micro- and Nano-Scale Biomanipulations in Atomic Force Microscopy”. In: IEEE, Oct. 2023, pp. 1–6. ISBN: 979-8-3503-3039-7. DOI: 10.1109/MARSS58567.2023.10294147. URL: https://ieeexplore.ieee.org/document/10294147/.

[19] Gerald Göring et al. “Tailored probes for atomic force microscopy fabricated by two-photon polymerization”. In: *Applied Physics Letters* 109 (6 Aug. 2016), p. 63101. ISSN: 00036951. DOI: 10.1063/1.4960386/32602. URL: /aip/apl/article/109/6/063101/32602/Tailored-probes-for-atomic-force-microscopy.

[20] H.M. Grandin et al. “Bioinspired, nanoscale approaches in contemporary bioanalytics (Review)”. In: *Biointerphases* 13 (4 Aug. 2018), p. 040801. ISSN: 1934-8630. DOI: 10.1116/1.5037582.

[21] Orane Guillaume-Gentil et al. “Force-Controlled Fluidic Injection into Single Cell Nuclei”. In: *Small* 9 (11 June 2013), pp. 1904–1907. ISSN: 1613-6829. DOI: 10.1002/SMLL.201202276. URL: https://onlinelibrary-wiley-com.tudelft.idm.oclc.org/doi/full/10.1002/smll.201202276%20https://onlinelibrary-wiley-com.tudelft.idm.oclc.org/doi/abs/10.1002/smll.201202276%20https://onlinelibrary-wiley-com.tudelft.idm.oclc.org/doi/10.1002/smll.201202276.

[22] Orane Guillaume-Gentil et al. “Injection into and extraction from single fungal cells”. In: *Communications Biology* 5 (1 Dec. 2022). ISSN: 23993642. DOI: 10.1038/s42003-022-03127-z.

[23] Orane Guillaume-Gentil et al. “Single-Cell Mass Spectrometry of Metabolites Extracted from Live Cells by Fluidic Force Microscopy”. In: *Analytical Chemistry* 89 (9 May 2017), pp. 5017–5023. ISSN: 15206882. DOI: 10.1021/acs.analchem.7b00367.

[24] Orane Guillaume-Gentil et al. “Tunable Single-Cell Extraction for Molecular Analyses”. In: *Cell* 166 (2 July 2016), pp. 506–516. ISSN: 0092-8674. DOI: 10.1016/J.CELL.2016.06.025.

[25] Sung Woong Han et al. “High-efficiency DNA injection into a single human mesenchymal stem cell using a nanoneedle and atomic force microscopy”. In: *Nanomedicine: Nanotechnology, Biology, and Medicine* 4 (3 Sept. 2008), pp. 215–225. ISSN: 15499634. DOI: 10.1016/j.nano.2008.03.005.

[26] Alina Hategan et al. “Adhesively-Tensed Cell Membranes: Lysis Kinetics and Atomic Force Microscopy Probing”. In: *Biophysical Journal* 85 (2003).

[27] Andreas Janshoff. “Viscoelastic properties of epithelial cells”. In: *Biochemical Society Transactions* 49 (6 Dec. 2021), pp. 2687–2695. ISSN: 14708752. DOI: 10.1042/BST20210476.

[28] Karen E. Kasza et al. “The cell as a material”. In: *Current Opinion in Cell Biology* 19 (1 Feb. 2007), pp. 101–107. ISSN: 09550674. DOI: 10.1016/j.ceb.2006.12.002.

[29] Bitterli. Joanna Katarzyna. “AFM Based Single Cell Microinjection: Technological Developements, Biological Experiments and Biophysical Analysis of Probe Indentation”. In: (2012).

[30] S. V. Kontomaris, A. Malamou, and A. Stylianou. “The Hertzian theory in AFM nanoindentation experiments regarding biological samples: Overcoming limitations in data processing”. In: *Micron* 155 (Apr. 2022). ISSN: 09684328. DOI: 10.1016/j.micron.2022.103228.

[31] Robert C.L.N. Kramer et al. “Multiscale 3D-printing of microfluidic AFM cantilevers”. In: *Lab on a Chip* 20 (2 Jan. 2020), pp. 311–319. ISSN: 14730189. DOI: 10.1039/c9lc00668k.

[32] Eun Young Kwon, Young Tae Kim, and Dae Eun Kim. “Investigation of penetration force of living cell using an atomic force microscope”. In: *Journal of Mechanical Science and Technology* 23 (7 2009), pp. 1932–1938. ISSN: 1738494X. DOI: 10.1007/s12206-009-0508-z.

[33] Chang Hun Lee. “A simple outline of methods for protein isolation and purification”. In: *Endocrinology and Metabolism* 32 (1 Mar. 2017), pp. 18–22. ISSN: 20935978. DOI: 10.3803/EnM.2017.32.1.18.

[34] Mi Li, Lianqing Liu, and Tomaso Zambelli. “FluidFM for single-cell biophysics”. In: *Nano Research* 15 (2 Feb. 2022). A review paper, pp. 773–786. ISSN: 19980000. DOI: 10.1007/s12274-021-3573-y.

[35] Qing Luo et al. “Cell stiffness determined by atomic force microscopy and its correlation with cell motility”. In: *Biochimica et Biophysica Acta - General Subjects* 1860 (9 Sept. 2016), pp. 1953–1960. ISSN: 18728006. DOI: 10.1016/j.bbagen.2016.06.010.

[36] Kang Lv and Yinfeng Li. “Indentation of Graphene-Covered Atomic Force Microscopy Probe Across a Lipid Bilayer Membrane: Effect of Tip Shape, Size, and Surface Hydrophobicity”. In: *Langmuir* 34 (26 July 2018), pp. 7681–7689. ISSN: 15205827. DOI: 10.1021/acs.langmuir.8b01262.

[37] Kaitlin P. McCreery et al. “Nuclear Stiffness Decreases with Disruption of the Extracellular Matrix in Living Tissues”. In: *Small* 17 (6 Feb. 2021). ISSN: 16136829. DOI: 10.1002/smll.202006699.

[38] André Meister et al. “FluidFM: Combining atomic force microscopy and nanofluidics in a universal liquid delivery system for single cell applications and beyond”. In: *Nano Letters* 9 (6 June 2009), pp. 2501–2507. ISSN: 15306984. DOI: 10.1021/NL901384X/SUPPL_FILE/NL901384X_SI_001.PDF. URL: https://pubs-acs-org.tudelft.idm.oclc.org/doi/full/10.1021/nl901384x.

[39] Ron Milo and Rob Philips. *CELL BIOLOGY by the numbers*. 1st ed. Garland Science, 2015. ISBN: 9780815345374.

[40] Emad Moeendarbary and Andrew R. Harris. “Cell mechanics: Principles, practices, and prospects”. In: *Wiley Interdisciplinary Reviews: Systems Biology and Medicine* 6 (5 2014), pp. 371–388. ISSN: 1939005X. DOI: 10.1002/wsbm.1275.

[41] Ikuo Obataya et al. “Nanoscale operation of a living cell using an atomic force microscope with a nanoneedle”. In: *Nano Letters* 5 (1 Jan. 2005), pp. 27–30. ISSN: 15306984. DOI: 10.1021/nl0485399.

[42] Marcos Penedo et al. “Cell penetration efficiency analysis of different atomic force microscopy nanoneedles into living cells”. In: *Scientific Reports* 11 (1 Dec. 2021). ISSN: 20452322. DOI: 10.1038/s41598-021-87319-3.

[43] Marcos Penedo et al. “Visualizing intracellular nanostructures of living cells by nanoendoscopy-AFM”. In: *Sci. Adv* 7 (2021), p. 4990. URL: https://www.science.org.

[44] *Products | Cytosurge*. https://www.cytosurge.com/shop. Accessed: 23-11-2022.

[45] Bahram Rajabifar et al. “Machine Learning Approach to Characterize the Adhesive and Mechanical Properties of Soft Polymers Using PeakForce Tapping AFM”. In: *Macromolecules* 55 (19 Oct. 2022), pp. 8731–8740. ISSN: 15205835. DOI: 10.1021/acs.macromol.2c00147.

[46] M. Rostami and M. T. Ahmadian. “Numerical investigation of force and deflection of nanoneedle penetration into cell using finite element approach: Parameter study and experimental validation of results”. In: *International Journal for Numerical Methods in Biomedical Engineering* 39 (9 Sept. 2023). ISSN: 20407947. DOI: 10.1002/cnm.3749.

[47] Prithwidip Saha, Tal Duanis-Assaf, and Meital Reches. “Fundamentals and Applications of FluidFM Technology in Single-Cell Studies”. In: *Advanced Materials Interfaces* 7 (23 Dec. 2020). ISSN: 21967350. DOI: 10.1002/admi.202001115.

[48] Jianmin Song et al. “Probing Multidimensional Mechanical Phenotyping of Intracellular Structures by Viscoelastic Spectroscopy”. In: *ACS Applied Materials and Interfaces* 12 (1 Jan. 2020), pp. 1913–1923. ISSN: 19448252. DOI: 10.1021/acsami.9b19597.

[49] Raffaella Suriano et al. “Nanomechanical probing of soft matter through hydrophobic AFM tips fabricated by two-photon polymerization”. In: *Nanotechnology* 27 (15 Feb. 2016). ISSN: 13616528. DOI: 10.1088/0957-4484/27/15/155702.

[50] Ivan U. Vakarelski et al. “Penetration of living cell membranes with fortified carbon nanotube tips”. In: *Langmuir* 23 (22 Oct. 2007), pp. 10893–10896. ISSN: 07437463. DOI: 10.1021/la701878n.

[51] Yuzhang Wei and Qingsong Xu. “A Survey of Force-Assisted Robotic Cell Microinjection Technologies”. In: *IEEE Transactions on Automation Science and Engineering* 16 (2 Apr. 2019), pp. 931–945. ISSN: 15455955. DOI: 10.1109/TASE.2018.2878867.

[52] Guocheng Zhang et al. “Molecular dynamics simulation of cell membrane penetration by atomic force microscopy tip”. In: *Modern Physics Letters B* 32 (18 June 2018). ISSN: 02179849. DOI: 10.1142/S0217984918501981.

[53] Guocheng Zhang et al. “Study of the Effect of Cell Prestress on the Cell Membrane Penetration Behavior by Atomic Force Microscopy”. In: *Micromachines* 14 (2 Feb. 2023). ISSN: 2072666X. DOI: 10.3390/mi14020397.

II

Paper

Quantification of cell membrane insertion events using force spectroscopy

This study investigates the processes of cell membrane puncturing and the factors influencing these processes through force spectroscopy experiments. A custom-designed tall and sharp tip was fabricated on a commercially available microcantilever using two-photon polymerization (2PP). Force spectroscopy curves were measured at several locations on the cell while the tip was inserted inside the cell. A cell membrane insertion event, identified as a "force drop" in force spectroscopy curves, is often hardly visible or does not occur. In this study, the effects of probe tip diameter, cantilever spring constant, insertion velocity, and cell height of mouse preosteoblast cells were systematically analysed for their influence on how often the force drops occur and how clearly they are visible. Data processing algorithms were employed to process thousands of force spectroscopy curves, enabling large sample statistical analysis using multiple linear regression. The results demonstrate that selecting cells with maximum height and size increases force drop occurrence from 10% to 40%. Furthermore, while decreasing the tip diameter from 2 to 0.7 μm did not affect the occurrence rate, it increased force drop visibility from $\sim$250 to $\sim$600 pico-Newton (pN). Additionally, cantilevers with a spring constant of 0.2 N/m achieved higher force drop occurrence (40%) and visibility ($\sim$300 pN), compared to more flexible cantilevers with a spring constant of 0.02 N/m (20% occurrence, $\sim$40 pN visibility). These findings provide valuable insights for optimizing experimental parameters in cell membrane mechanics research.

I. Introduction

With the invention of micro and nanotechnologies, biologists studying single living cells encountered a new and unexplored field. Related technologies enable dynamic sensing and manipulation of single cells, and especially the real-time analysis of subcellular contents. The presence or absence of certain biomolecules inside the cell gives insights into underlying processes, physical or chemical, that affect cell behaviour. A fundamental understanding at the single-cell level can be applied to larger tissue and organ systems and has shown significant advancements in the available healthcare, such as medicinal drugs, cancer treatment, and tissue and organ transplants [1]. Therefore, single-cell studies have had a profound societal impact, benefiting the well-being of the environment, animals, and humans.

The atomic force microscopy (AFM) device, which has been used for this research, has demonstrated multiple capabilities for single-cell studies due to its force-sensitivity at the nanoscale and compatibility with liquid environments, and provides an inverted optical microscope for real-time monitoring of the cells. As depicted in Figure 1, the AFM consists of a flexible cantilever with a specific spring constant (k) and a sharp tip at its free end. A laser detects the deflection of the cantilever when applying nano-Newton forces to a sample. The force applied to the sample (F) can be calculated from the deflection of the cantilever ($d_{cantilever}$) using Hooke's law (Equation 1).

$$F = kd_{cantilever} \tag{1}$$

Examples of AFM for single-cell studies include measuring the elastic and viscous deformation of cells in reaction to mechanical forces [2][3], subsurface imaging of internal structures using sharp nanoprobes [4][5], and subcellular biopsy using microfluidic probes [6][7]. Because these processes minimise invasiveness, the cell usually remains alive, which allows for time-dependent studies. Moreover, the cell's processes are left mostly unperturbed, resulting in unaltered samples and more reliable conclusions.

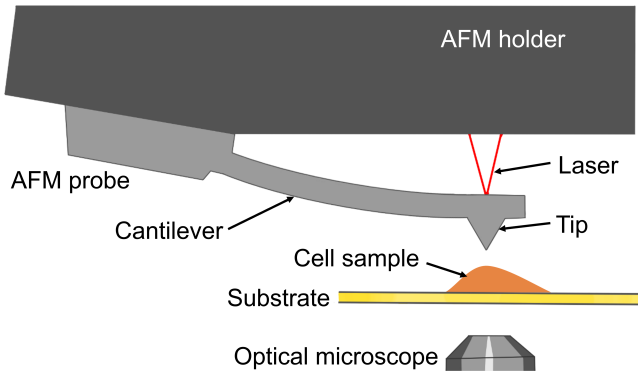

Fig. 1: Schematic of an Atomic Force Microscope (AFM) device showing the probe, cantilever, and tip. A laser is directed onto the back of the cantilever to detect deflections caused by interactions with the sample surface. The sample is placed beneath the tip and observed through an inverted optical microscope.

AFM is not the only sharp tip tool to probe cells on a subcellular level; micro and nanopipettes, nanostraws, and dielectrophoretic systems have shown their capabilities [8]. The important aspect that all these methods possess is the mechanical disruption of the cell membrane. Even though the micro and nano-sized probes minimise invasiveness, they still apply significant forces and deformation to puncture the cell membrane. Furthermore, due to cell-to-cell variability and single-cell variability over time, cell membrane insertion is not always successful, and measurements of these forces and deformations are not reproducible.

The force feedback of the AFM can be used to obtain a force spectroscopy curve, also known as a force-distance curve. To see if a cell membrane insertion is successful, the force-distance curve is observed for the presence of a

discontinuity in the curve, a small drop in force (“force drop”). Figure 2 depicts a typical force-distance curve as a sharp tip is inserted into and through a cell until the hard support substrate underneath. When the tip is far from the cell, zero cantilever deflection is measured, and thus, there is zero force; see area 1. The moment where the tip starts touching the cell membrane (contact point), the cantilever starts to deflect due to the cell body resisting the movement of the tip. As the tip indents the cell more and more, the force exerted on the tip increases nonlinearly, creating a curved, increasing line, see area 2. Eventually, the tip penetrates the cell membrane and inserts into the cell, momentarily releasing the force exerted on the tip. This results in a peak in the force-distance curve as the force drops during the insertion. Afterwards, the tip still moves further into the cell, and the force exerted increase again nonlinearly; see area 3. Finally, the tip reaches the hard support substrate underneath, which results in a sharp increase in cantilever deflection and force, as the tip cannot move further, see area 4. Multiple insertion events are also possible in one force-distance curve as the tip can encounter various membrane-bound organelles, such as the nucleus and endoplasmic reticulum.

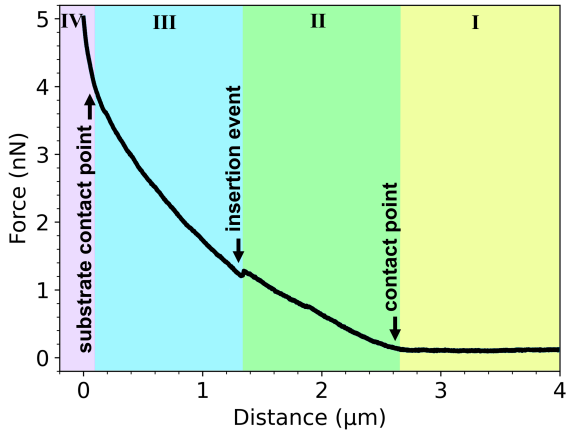

Fig. 2: A typical force-distance curve as a tip inserts into a cell, with labels at the contact point, insertion event and substrate contact point, and the coloured areas differentiating between different slopes

Real-time knowledge of the insertion event is crucial in single-cell biopsy or other sampling techniques, as it allows the researcher to confirm that the tip is inside the cell and proceed with the extraction procedure. The AFM force-distance curve can provide this real-time knowledge, however, in practice this insertion event is rarely seen due to the use of relatively large tip sizes[9], and always different insertion forces and indentation depths [10]. Furthermore, it is usually assumed that a force drop is caused by an insertion event and that an insertion always results in a force drop, it may not actually be the case. Thus, any efforts to increase the chance of a successful insertion event only increases the chance of observing a visible force drop, but this may not indicate a successful insertion.

Various attempts have been made to solve the cell insertion success rate problem, for instance, by manufacturing nanoprobes with high aspect ratios and diameters below 400 nm obtaining success rates of 98% [10], or by applying a prestress to the cell resulting in success rates of 62% at a strain of 20% [11]. Also, how the insertion forces and indentation depths can be reduced has been investigated, for example, by changing the spring constant of the cantilever [12] or by changing the geometry and size of the tip [9][13]. Furthermore, researchers claim that the cell behaves like a viscoelastic material. However, the effect of the insertion velocity is almost unknown. Additionally, most studies lack proper statistical analysis due to a small sample size and changing independent variables simultaneously, which results in low statistical power and validity of results.

Using two-photon polymerisation (2PP), a nanoscale three-dimensional (3D) printing technique, new force spectroscopy tip designs can be explored to improve success rates and reduce insertion forces and indentation depths. Multiple papers demonstrate how custom 2PP tips were printed on top of commercial silicon cantilevers [14], and even complete microfluidic cantilevers [15][16].

The aim of this study is to improve the quantifiability and reproducibility of a cell membrane insertion event using force spectroscopy on mouse preosteoblast cells (MC3T3-E1). The following four factors: cell height, tip diameter, insertion velocity, and cantilever spring constant; are studied for their effects on the following outcome variables: how often a force drop occurs (reproducibility), and how visible it is (quantifiability). Additionally, the effects on the insertion force and indentation depth corresponding to a force drop are also analysed. In particular, this paper defines the following objectives: (1) the microfabrication of custom tips with varying diameter on commercial cantilevers, (2) creating and evaluating algorithms tailored to process and analyse force-distance curves corresponding to cell membrane insertion, (3) analysing the variables that affect the occurrence of insertion events, (4) applying statistical analyses such as multiple linear regression to quantify individual and interaction effects of the factors that influence insertion event characteristics.

II. Materials and Methods

A. Fabrication of custom 3D printed tips

1) Tip design

The custom tips were printed on the cantilevers of the Tipless Silicon SPM Sensors ARROW-TL2 (NanoWorld, Switzerland), with two equally sized cantilevers on one chip, see Figure 3. The technical specifications were: length = 500 µm, width = 100 µm, and thickness = 1 µm. The spring constant was 0.03 $\mathrm{N/m}$, but could fall in the range 0.004 to 0.54 $\mathrm{N/m}$ due to variation in cantilever dimensions. The triangular end of the cantilever had an angle of 58° and side lengths of 94 µm.

The considerations during the tip design process can be summarised as follows:

- The base of the tip must fit inside the area of the surface of the cantilever;

- The tip must correct for the 11° tilt in the cantilever holder;
- The tip must be printed at the very end of the cantilever for tip visibility during use;
- The tip design must be flexible so that different diameter tips can be made;
- The tip apex must have a sharp ending;
- The base dimensions must be increased to improve adhesion strength between substrate and printed tip.

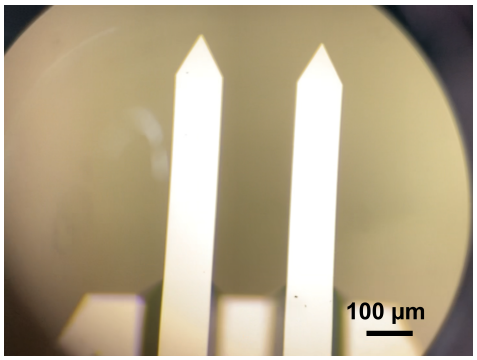

Fig. 3: The Arrow-TL tipless cantilevers seen through an optical microscope with magnification 40x

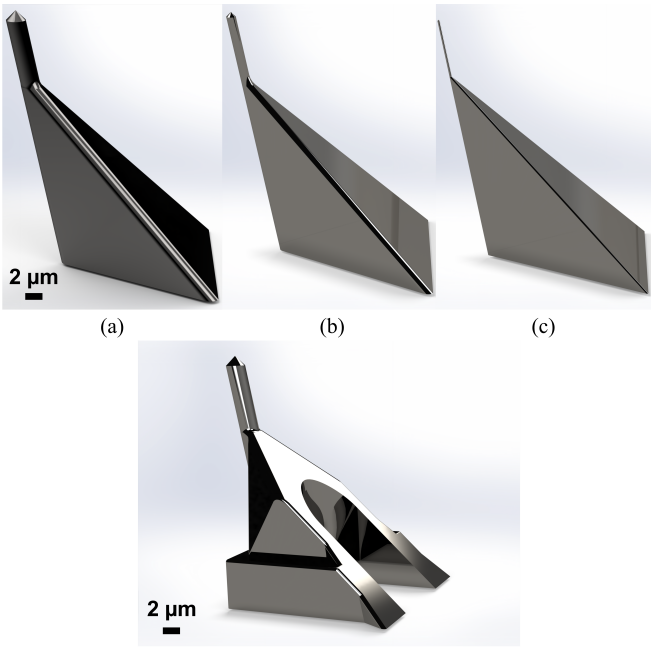

(a) (b) (c)

(d)

Fig. 4: 3D SolidWorks model of tip designs for cylindrical diameters: (a) 2, (b) 1 and (c) 0.2 µm; and (d), the altered tip design for the re-used clogged microfluidic cantilever with cylindrical diameter 2 µm

The final tip design was made using the computer-aided design (CAD) software SolidWorks (Dassault Systèmes SolidWorks Corporation, US). It consisted of an 11° slanted triangular pyramid base with side lengths of 20 µm, carrying a cylindrical tip with a diameter of 2 µm, finished off with a sharp cone on top (Figure 4a). This tip design was also made with cylindrical tip diameters of 1 and 0.2 µm (Figures 4b and 4c).

Additionally, to increase the range of the cantilever spring constant between different probes, clogged microfluidic cantilevers (FluidFM Nanosyringe, Cytosurge AG, Switzerland) were re-used by printing the tip design around the already existing pyramidal tip. The tip design was slightly altered around the base to increase the contact area for adhesion and avoid printing on the pyramid (see Figure 4d).

2) Two-photon polymerisation

The fabrication technique used to print the tip on the cantilever is two-photon polymerisation. The printer used is the Photonic Professional GT2 by Nanoscribe (Nanoscribe GmbH & Co. KG), using a 63x objective with a numerical aperture of 1.4 operated in Dip-in Laser Lithography (DiLL). The micro-cantilever chips were fixed on a 3D printed chip holder (see Appendix A), and one droplet of the negative tone IP-Dip2 photoresist (Nanoscribe GmbH & Co. KG) was deposited on the cantilevers before printing.

The tip designs were imported as STL files into the software Describe (Nanoscribe GmbH & Co. KG) to create a file which can be read by the printer. In this process, the design volume is split into horizontal hatching layers and vertical slicing layers. The hatching and slicing distances were both 0.1 µm. This fabrication technique requires correctly tuned laser power and scan speed to obtain the correct laser dose. The higher the laser power (%) and/or scan speed (µm/s), the higher the laser dose. To find the best combination of laser power and scan speed, a parameter sweep was printed. This resulted in a laser power of 10 mW (20% of a maximum power of 50 mW) and a scan speed of 10 mm/s. Using the software NanoWrite (Nanoscribe GmbH & Co. KG), the tip design can be aligned correctly with the end of the cantilever and subsequently printed.

Afterwards, the micro-cantilever chips are developed by submerging the chip holder horizontally in a borosilicate Petri dish filled with propylene glycol methyl ether acetate (PGMEA) for 25 min, with refreshment after 10 min, to dissolve the unpolymerised resin. Then, it was submerged in iso-propanol (IPA) for 10 min, followed by submersion in Novec™ 7100 Engineered Fluid for 5 min. In each step, the submerged chip holder was agitated every ∼30 s using tweezers. Finally, the chips are left to air dry.

The Young's modulus of polymerised IP-Dip2 is known to be 1.5 GPa, however this may vary depending on the printing conditions and parameters.

3) Scanning electron microscopy

To image the micro-cantilever chips using a scanning electron microscope (SEM), they are first sputtered with a thin (∼10 nm) layer of gold to avoid charge buildup. This was done using the Sputter Coater JEOL JFC-1300 (JEOL Ltd., Japan). The chips are then coated horizontally using a current of 20 mA for 45 s.

The SEM used is the JEOL JSM-6010LA scanning electron microscope (JEOL Ltd., Japan), where the secondary electron generated images were recorded of the cantilevers, the complete tip from top, side and 45° views, and a close-up of the cylindrical tip from the side. The accelerating voltage ranged

from 4 to 8 kV, and the electron beam spot size ranged from 48 to 56 nm.

The images were inspected to see if the tip was printed successfully without visual artefacts. Moreover, a close-up of the cylindrical tip is used to measure and compare the dimensions of the tip w.r.t. in the design. Three characteristics are measured using Fiji (ImageJ) [17]: the height of the tip (H), the diameter of the tip (D), and the radius of curvature at the tip apex (r). The measurement for height and radius of curvature was repeated three times on the same tip, and the diameter was repeated six times at different locations along the tip length. The mean was calculated for each characteristic and added to the table. Then, the total mean and uncertainty were calculated, which were then compared to the actual design dimensions. The min-max uncertainty is used in this case, which is defined by the range of measured values divided by two (see Equation 2).

$$Uncertainty = \frac{Max - Min}{2} \tag{2}$$

4) Force spectroscopy experiments on PDMS

The instrument used for the force spectroscopy experiments was a JPK Nanowizard 4 BioAFM (Bruker-JPK Instruments AG, Germany) mounted on an inverted optical microscope (Zeiss Axio Observer 3, Carl Zeiss Microscopy GmbH). To test the operation of the tip, a micro-cantilever chip with a printed tip of diameter 2 $\mu\mathrm{m}$ was installed in the AFM. Force-distance curves were measured in force spectroscopy mode as the tip came into contact with a polymer sheet of polydimethylsiloxane (PDMS).

Using the JPK data processing software (Bruker-JPK Instruments AG, Germany), the force-distance curve is fitted using the Hertz model and the indenter geometry to estimate the Young's modulus of the PDMS [18]. The indenter geometry is estimated using a paraboloid shape with a tip radius of 260 nm and a Poisson ratio 0.5. The same PDMS sample is tested under the PIUMA nanoindenter system (Optics 11, Amsterdam, The Netherlands), using a spherical probe with tip diameter 20 $\mu\mathrm{m}$ and stiffness 51.2 $\mathrm{N/m}$. The nanoindenter also measured the Young's modulus using the Hertz model, which was then compared to the measurement from the AFM.

B. Force spectroscopy experiments on cells

1) Cell culture

Mouse preosteoblast cells (MC3T3-E1, Sigma-Aldrich, Germany) were seeded at a concentration of 1×10^5 and 2×10^5 $\mathrm{cells/cm^2}$ in a 35 mm tissue culture dish (TPP Techno Plastic Products AG, Switzerland). The samples are incubated in the alpha minimal essential medium (α-MEM without ascorbic acid: supplemented with 10% (v/v) fetal bovine serum, 1% (v/v) penicillin-streptomycin (10 000 units/mL), pH = 7.5, Life Technologies, US), for 2 to 4 days (37°C, 5% CO_2). The medium is refreshed after 2 days. All cells were adhered to the substrate, which creates a sparse monolayer.

2) Force spectroscopy data collection

The micro-cantilever with the custom 3D tip was loaded into the AFM, and the Petri dish containing the cells was mounted in the JPK Petri dish heater (Bruker-JPK Instruments, Germany), maintaining a constant temperature of 37°C during experiments. Before starting the measurements, the cantilever sensitivity and spring constant were calibrated using the thermal noise method implemented in the JPK AFM control software.

Force-distance curves were again acquired in the force spectroscopy mode. The tip was inserted into the cell at a constant insertion velocity until it reached the hard substrate underneath with a certain set-point force. The set-point force ranged between 5 and 10 nN. After reaching the set-point force, the tip retracts for 8 $\mu\mathrm{m}$ at the same velocity. The force exerted on the tip of the cantilever is measured as it is inserted into and retracted from the cell, and this is plotted against the distance travelled by the cantilever.

To obtain as much data as possible, all force-distance curves were acquired in a grid-like manner. The grid dimensions and resolution were varied throughout the experiments, with dimensions ranging between 10x10 and 25x25 points and with point-to-point increments ranging between 2 and 5 $\mu\mathrm{m}$. The live camera from the inverted optical microscope was used to position the tip, which was exactly underneath the end of the cantilever, to the desired position on the edge of the cell. The grid force spectroscopy measurements were started, which then covered a part of the cell and part of the surrounding hard substrate.

To test the tip diameter effects, the tips with different diameters (2, 1 and 0.7 $\mu\mathrm{m}$) were alternated in the cell experiments while keeping the insertion velocity constant at 2 $\mu\mathrm{m/s}$. Keeping insertion velocity constant during those experiments will help to isolate their separate effects. Similarly, to test the insertion velocity effects, the tip with a diameter of 2 $\mu\mathrm{m}$ was used while changing the insertion velocity (0.5, 1, 2, 5, 10 and 20 $\mu\mathrm{m/s}$). To test the effect of spring constant, two cantilever models were used: the Arrow-TL tipless cantilevers with spring constants in the range of 0.004 to 0.54 $\mathrm{N/m}$, and re-used clogged microfluidic cantilevers with spring constants around 1.6 $\mathrm{N/m}$.

During these experiments, the exact spring constant of the cantilever could not be controlled, even though the same two cantilever models were used. This is due to the fabrication limitations in accurately controlling the thickness of the cantilever. Therefore, the slight differences in the cantilever spring constant were measured to later examine its effects.

After the cell experiments were finished, SEM images of the used cantilevers were taken to check if the tip was still intact.

3) Processing the force spectroscopy data

Data analysis was performed using a self-built Python tool (see Section II-C), and sometimes the JPK data processing software (Bruker-JPK Instruments, Germany) was used to examine individual force-distance curves.

First, the distance data was processed to transform the axis to be zero at the hard substrate and positive as you move away from it. This means, that while the tip is approaching the cell, the distance decreases between the hard substrate and the tip, reaching zero when in contact with the hard substrate. Second, during the indentation process, the cantilever deflects, resulting in a small offset between the distance measured by

the piezo and the actual position of the tip. The distance axis is therefore again transformed to correct for this small changing offset (see Section II-C1), to create a new x-axis called 'tip-sample separation'.

A visible force drop is not always observed, suggesting that an insertion event is not always paired with a force drop, or the insertion event did not occur, where the cell deforms under the load and does not let the tip inside. Figure 5a shows a typical force-distance curve when there is no force drop; the force nonlinearly increases until it reaches the hard substrate underneath. Additionally, multiple force drops in one force-distance curve can occur; see Figure 5b. This may be due to multiple membrane perforations from the nucleus to other membrane-bound organelles present inside the cell. To obtain information on how often the insertion event occurs, and if there are multiple insertion events, the number of insertion events per force-distance curve was counted using a peak detection algorithm (II-C3).

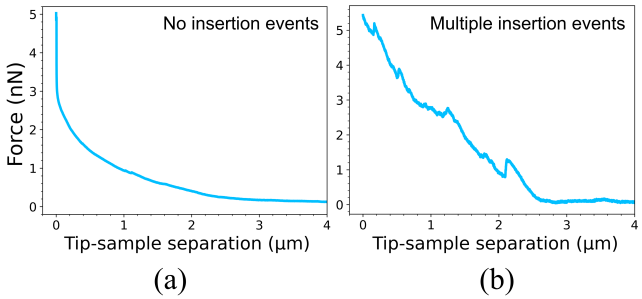

Fig. 5: A typical force-distance extend curve with (a) no insertion events, and (b) with multiple insertion events

In the case of a successful insertion event, three characteristics of the peak are calculated: insertion force, force drop and indentation depth (see Figure 6).

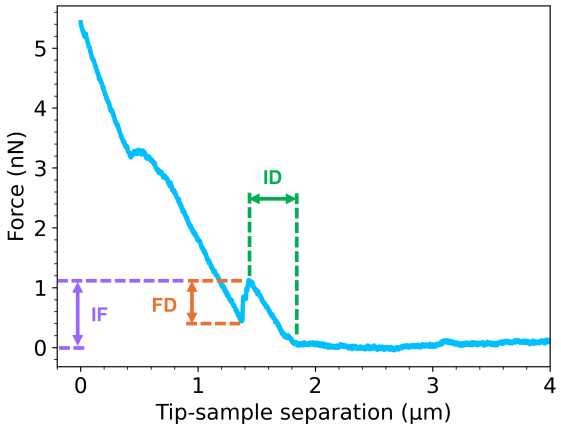

Fig. 6: The three characteristics of an insertion event: force drop (FD), insertion force (IF) and indentation depth (ID)

- The insertion force is defined as the force required to penetrate the cell membrane, and this is measured as the force value at the tip of the peak.
- The force drop is defined as the difference between the insertion force and the decreased value of force. This was measured as the left-sided peak height.
- The indentation depth is defined as the difference in distance between the contact point and the moment of insertion, measured by subtracting the cell height (contact point) from the tip position at the peak.

Automatic processing algorithms (Section II-C were then used to extract extra information (metadata) on the experimental settings to acquire the force-distance curve. These are: cantilever spring constant and insertion velocity. The tip diameter of the tip used in the experiment is manually added to the metadata. At last, the metadata together with the values for number of insertion events, force drop, insertion force and indentation depth for each force-distance curve, are accumulated and stored.

C. Algorithms for data processing and analysis

A Python tool was written in order to analyse hundreds of force-distance curves automatically in minutes. The essential processing steps that one would do to the data in the JPK data processing software are also implemented in the Python tool. Because the force-distance curves display the cell reaction to a sharp tip insertion, they are not typical force-distance curves. Therefore, it was found that the processing methods used in the JPK data processing software were unsuitable for accurate automatic processing without manual interventions. Hence, most processing steps described in this section follow a different methodology to allow for accurate automatic processing.

1) Loading force spectroscopy data and basic corrections

All the algorithms written to automatically process data is implemented in Python programming language. To load the JPK force spectroscopy data, the Python library `afmformats` [19] was used. This reads each force-distance curve data and metadata, such as: piezo height, force, time, x and y positions, speed, sensitivity and spring constant.

Force-distance curves are not always perfect and need some adjustments. For instance, the laser is not aligned exactly in the middle of the laser detector, causing the baseline to have some offset from zero force. This usually occurs due to thermal drift during experiments. Thus, all force data must undergo a baseline correction so that the force data before contact is approximately zero. The method used for this correction is a simple vertical translation by the minimum value in the approach force array.

Similarly, the distance data needs to be corrected for two reasons. Firstly, the distance data is taken directly from the piezo movement, which is not exactly the location of the tip apex because it does not account for the deflection of the cantilever. To correct for this, the deflection of the cantilever must be added to the distance data to obtain the real tip-sample separation (δ). Figure 7 explains this schematically. The deflection can be derived from dividing the force data by the cantilever spring constant. This calculation is done element wise, where each element in the force data (f) is divided by the spring constant (k) and added to the corresponding element of the distance array (d) (Equation 3).

$$\delta = d + \frac{f}{k} \tag{3}$$

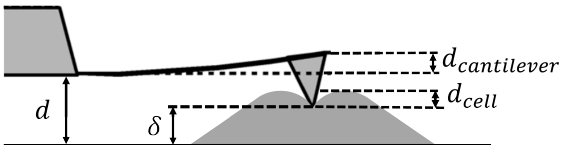

Fig. 7: Schematic of the cantilever deflection ($d_{cantilever}$) effect on the actual position of the tip with respect to the hard substrate (δ), where d is the measured piezo distance and d_{cell} the deformation of the cell

The second correction is to correct the sample-distance estimation made by the AFM, which should be zero when the tip is in contact with the hard substrate beneath the cell. This only requires a horizontal translation of the distance data by the distance value at the last data point.

2) Contact point determination

The contact point determination is one of the most crucial steps. If not done accurately, it will lead to false results in indentation measurements, cell height, and the calculation of the Young's modulus [20]. As this contact point is not obtained directly from the AFM and needs to be identified by carefully observing the force-distance curve, it makes this a time-consuming step. In this study, thousands of force-distance curves will be collected. Thus, algorithms need to be employed to determine the contact points fast.

Various methods have been applied to determine the contact point automatically; the challenge is to see if the method also works for soft matter, especially living cells. In this study, four different methods are evaluated on a test data set based on how close their estimated contact point are to the real contact point (manually identified). This test set consists of a subset of 200 force-distance curves corresponding to a grid measurement on one cell. The evaluation uses the mean absolute deviation (MAD) to measure how well the method estimated the contact point, the smaller the MAD error, the better. The MAD error calculation is defined in Equation 4, where n is the number of force-distance curves in the test set (in this case 200), $\mathbf{x_{estimated}}$ is the estimated contact point by one of the methods, and $\mathbf{x_{real}}$ is the real contact point.

$$MAD = \frac{1}{n}\sum_{i=1}^{n} |x_{estimated,i} - x_{real,i}| \tag{4}$$

Also, the confidence intervals of 5 to 95% of the deviation errors are noted to get an idea of the spread of the data; the smaller the interval, the better. In the following headers, the four methods are described.

Deviation from baseline:

In the data processing software supplied by JPK, the contact point is determined by identifying the point where the curve leaves the zero force line (baseline). If the baseline is noisy or tilted, the baseline can be smoothed and corrected with an offset. However, this is something done manually to make sure the baseline correction is correct. The default setting for the baseline correction is to find the average value of the first 10% of the data and offset the whole curve by that value [21].

The first 50% data points are used instead of the first 10% because the collected data all had relatively long baselines. The first threshold value, $h1$, is defined as the standard deviation of the first 50% of the data multiplied by a factor 4. The details of the algorithm are given in Appendix B.

Ratio of Variances:

Another method, proposed by Gavara et al. (2016), is the ratio of variances (RoV) [20]. For every force data point (f_i), the variance of a specific interval of data points (N) to the left and to the right of it is calculated. Then the forward interval is divided by the backwards interval to obtain the ratio, see Equation 5.

$$RoV_i = \frac{var(f_{i+1} : f_{i+N})}{var(f_{i-N} : f_{i-1})} \tag{5}$$

If the two intervals to the left and right of a data point have similar variance, then the ratio results in a value around 1; if very dissimilar, the ratio results in a value higher than 1. Then, the RoV (y-axis) is plotted against tip-sample separation (x-axis), and spikes will show at places where there is a change in variance. The contact point will occur at such a spike, and the spike can be detected using a peak detection algorithm (similar to the method explained in Section II-C3). Because multiple spikes will be present, and a selection of the contact point spike must be made, the largest spike is chosen. The details of the algorithm are given in Appendix B.

Linear/non-linear piecewise regression:

The force-distance curve can also be fitted with a known model that resembles the most common shape. For example, a piecewise regression consisting of a linear segment followed by some non-linear segment. The change point of the piecewise model (where the linear segment changes into the non-linear segment) is then chosen as the contact point. Multiple different functions can be used for the non-linear segment, such as polynomials, power laws, and exponentials.

Due to the variety of non-linear functions that can be used, several will be tested and evaluated on the data set. The following non-linear functions are considered:

- Second-order up to ninth-order polynomials: $a_n x_n + a_{n-1}x_{n-1} + ... + a_1 x + a_0$
- Power-law: $ax^b + c$
- Exponential: $ae^{bx} + c$

The details of the algorithm are given in Appendix B. ***Derivative:***

Another alternative is the derivative method, which takes the numerical difference between two data points with a specific interval in between [22]. The forward derivative is used; see Equation 6. This computes the slope (m_i) between a data point (d_i,f_i) and a specific number of points (N) further, another data point (d_{i+N},f_{i+N}).

$$m_i = \frac{f_{i+N} - f_i}{d_{i+N} - d_i} \tag{6}$$

The derivative (y-axis) can be plotted against the tip-sample separation (x-axis). Where the slope is constant, the derivative will be close to zero. At the point of contact, a sudden decrease in the derivative value will be observed (negative slope). To find this point, a similar method is used as in the deviation from the baseline method. Because the baseline in this method is inherently zero (constant slope), the threshold values are imposed on the actual value of the derivative of each point. The details of the algorithm are given in Appendix B.

3) Identifying and quantifying insertion events

The insertion events, which are observed as force drops in a force-distance curve, are in different locations with different magnitudes and shapes. Therefore, these events are very difficult to reproducibly and automatically identify. The method used for insertion event detection is the `find_peaks` function provided by the Python library `scipy` [23]. This function finds all the local maxima (peaks) in the force data array by the simple comparison of neighbouring values, and then a subset of these peaks is chosen based on specified peak prominence. The peak prominence is a measure of how much a peak stands out from the surrounding peaks, which is calculated as the vertical distance between the peak and its lowest contour line (base of peak). This is similar to the height of the peak, only that in this case, the value of the base of the peak to the left and to the right may be different, and in this method, the highest base value is chosen as the lowest contour line.

Once the insertion points have been found, each force-distance curve with at least one insertion event is analysed further for the characteristics of the peak: force drop, insertion force, and indentation depth.

First, the insertion force is found by taking the absolute height (force) of the peak, which is returned by that same `find_peaks` function. Then, the height of the base to the left of the peak is found (also returned by the function), which can be subtracted from the insertion force to obtain the force drop. Finally, the position of the peak in terms of tip-sample separation is subtracted from the position of the contact point to obtain the indentation depth.

4) Fitting apparent Young's modulus

The model used to fit the Young's modulus on the force-distance curve is the model for parabolic indenter [24], see Equation 7. With E the Young's modulus, ν the Poisson ratio, R_C the radius of curvature at the apex of the paraboloid indenter, δ the deformation of the cell for a certain force F.

$$F = \frac{4\sqrt{R_C}}{3}\frac{E}{1-\nu^2}\delta^{3/2} \tag{7}$$

D. Statistical analysis

The total number of force–distance curves was first counted. Next, all curves corresponding to no cell and only the hard support substrate were excluded by applying the constraint that the cell height must be greater than 0.5 µm. The remaining force–distance curves were then counted. These remaining data were used for the analysis of the effects of the independent variables on the dependent variables. A summary of these variables is provided in Table I.

TABLE I: Summary of the four independent variables and four dependent variables

Independent variables (X)	Dependent variables (Y)
Cell height (H)	Number of insertion events (N)
Tip diameter (D)	Force drop (FD)
Insertion velocity (V)	Insertion force (IF)
Spring constant (S)	Indentation depth (ID)

1) Number of insertion events

The integer dependent variable "number of insertion events" was analysed first. This variable represents the number of peaks identified in a force–distance curve. A value of zero indicates no insertion events were identified, while a value of one or more indicates one or more insertion events were detected. To examine the effect of height on this variable, a bar chart was created using all the data (force–distance curves). Height was divided into 0.5 µm bins on the x-axis, and the y-axis shows the number of insertion events as a percentage of the total number of force–distance curves within each height bin.

This process was repeated for the other independent variables. Since these variables have discrete values, they define the binning for the x-axis in the bar charts. Additionally, an important step was to filter out force–distance curves where the velocity was altered for the analysis of tip diameter, and vice versa. The bins and data filters for each independent variable are summarised in the following points:

- **H.** Bins: 0.5-1, 1-1.5, 1.5-2, 2-2.5, 2.5-3, 3-3.5, 3.5-4, 4-4.5, >5 (µm). Data: all.
- **D.** Bins: 0.7, 1, 2 (µm). Data: with constant velocity (v = 2 µm/s) and Arrow-TL cantilevers (k < 0.5 N/m).
- **V.** Bins: 0.5, 1, 2, 5, 10, 20 (µm/s). Data: with constant tip diameter (d = 2 µm) and Arrow-TL cantilevers (k < 0.5 N/m).
- **S.** Bins: 0.021-0.025, 0.146, 0.17, 0.216, 0.326, 0.524, 1.149 (N/m). Data: all.

The bar charts were then observed for any increasing or decreasing trends.

2) Force drop, insertion force and indentation depth

After completing the analysis of the number of insertion events, a statistical analysis was conducted to quantify the effects of the independent variables on the characteristics of the first insertion event: force drop, insertion force, and indentation depth. The dataset containing all the force–distance curves was further filtered to exclude curves without insertion events. This removal was necessary because the variables characterising the insertion event are zero when no insertion occurs. With 70% of the force–distance curves showing zero insertion events, retaining these zeros would heavily skew the distribution of variables with non-zero values.

The statistical analysis addressed the following question: what is the effect of X on Y when an insertion event is present? Once this question was answered, the findings were integrated with results from the analyses of the number of insertion events and success rates, leading to an overall conclusion.

In this research, linear regression is applied to see if one independent variable affects an outcome variable. The method

used to fit the linear regression was ordinary least squares (OLS). OLS is a basic and interpretable method to solve a linear regression problem, however, it is sensitive to outliers and to dependence among variables [25]. In light of these limitations, the data was standardised to centralise the mean of the data around zero, and the dependence among variables was analysed through a correlation matrix. Equation 8 shows the formula used to standardise each independent variable, where μ and σ are the mean and standard deviation of the data. The correlation is calculated by dividing the covariance of two variables by their standard deviations multiplied. If the correlation is 0 the two variables are not correlated, if it is +1, then the two variables are perfect positively correlated, and if it is -1, the two variables are perfect negatively correlated.

$$z = \frac{x - \mu}{\sigma} \tag{8}$$

Furthermore, because it is a linear regression, it cannot explain any non-linearities in the data [25]. Even though the relationships between the independent variables and dependent variables are likely non-linear, this research chooses the interpretability of the OLS linear regression over an uninterpretable and complex model.

First, simple linear regression was applied to the data, testing each independent variable individually against each dependent variable. This analysis provides coefficient estimates and their associated standard errors. A t-test was then conducted for each coefficient to evaluate whether it is no different from zero (null hypothesis) or significantly different from zero (alternative hypothesis). If the coefficient is no different from zero, it suggests no relationship exists between the tested independent and dependent variables. The t-test also determines the statistical significance of the coefficients, yielding t-values, p-values, and confidence intervals. A p-value below 0.05 indicates statistical significance. Ideally, the standard errors and confidence intervals should be narrow, reflecting precise estimates. This method is highly interpretable, however, it is limited to using only one independent variable to explain the data, whereas in reality all four independent variables may have had an influence on the data.

Second, multiple linear regression was employed to predict the impact of several independent variables on an outcome variable [26]. This method assumes that the independent variables are independently and identically distributed. To verify this assumption, a correlation matrix was computed prior to applying the regression analysis. High correlations between independent variables can lead to collinearity, which negatively affects the regression results by producing unreliable coefficient estimates and obscuring the individual contributions of the correlated variables to the outcome. Multiple linear regression provides a slightly more complex model to the simple linear regression, while keeping the results interpretable. However, it cannot account for interaction effects between independent variables.

Multiple linear regression also enables us to test if interactions are present between independent variables [26]. An interaction means that two variables affect each other's values. For example, take the independent variables cell height (x_1) and tip diameter (x_2). Then, their interaction term can be created by multiplying them together ($x_1 * x_2$). The two variables and their interaction term will also have their own coefficients (β_1, β_2 and β_3) and an intercept (β_0). Equation 9 presents the formula for multiple linear regression with two independent variables and an interaction term. Each coefficient is linked with a standard error, which is omitted from the equation for clarity.

$$y = \beta_0 + \beta_1 x_1 + \beta_2 x_2 + \beta_3 x_1 x_2 \tag{9}$$

The interaction terms for the four independent variables are: H×D, H×V, H×S, D×S, and V×S. The interaction term D×V was excluded because these variables were controlled during the experiments, and their individual effects were independently measured. Consequently, the total number of parameters in the multiple linear regression model is nine, resulting in a very large model. Such large models are challenging to interpret and likely result in overfitting. Overfitting occurs when the model includes variables or interaction terms that do not influence the outcome but still capture some variation, leading to spurious contributions.

Selecting variables and/or interaction terms to remove from the model can be challenging and time-consuming. To address this, the Bayesian Information Criterion (BIC) is used to evaluate how well the statistical model explains the observed data while favouring simplicity. The BIC is defined in Equation 10, where n represents the sample size, and d denotes the number of parameters.

$$BIC = -2 * loglikelihood + p \log n \tag{10}$$

This quantification is based partly on the log-likelihood (how well the model explains the data), and partly based on penalising an increase in number of parameters in the model (how complex the model is) [27]. The model with the smallest BIC value is then preferred. This method has been used to simplify the very large and difficult to interpret model that includes all variables and interaction terms. The algorithm used to perform the multiple linear regression with interaction variables and the model selection using BIC is described in Appendix D.

III. Results

A. Evaluation of custom 3D printed tips

1) Scanning electron microscopy

Figure 8(a, b, c) shows the SEM images taken at 45° angle of each different diameter tip printed on an Arrow-TL cantilever. Both the 2 and 1 µm tip prints were as designed. Only the 0.2 µm tip prints consistently resulted in a tip that was more upright than slanted. Additionally, Figure 9 depicts a SEM image of the altered tip design printed on re-used clogged microfluidic cantilevers.

The close-up SEM images of the cylindrical tip end taken from the side are shown in Figure 8(d, e, f). The evaluation of the characteristics are presented in Table II, which shows the original design dimensions and the actual dimensions. The results show that for the 2 µm tip, the diameter was consistently around 2 µm, and the height was consistent but 1

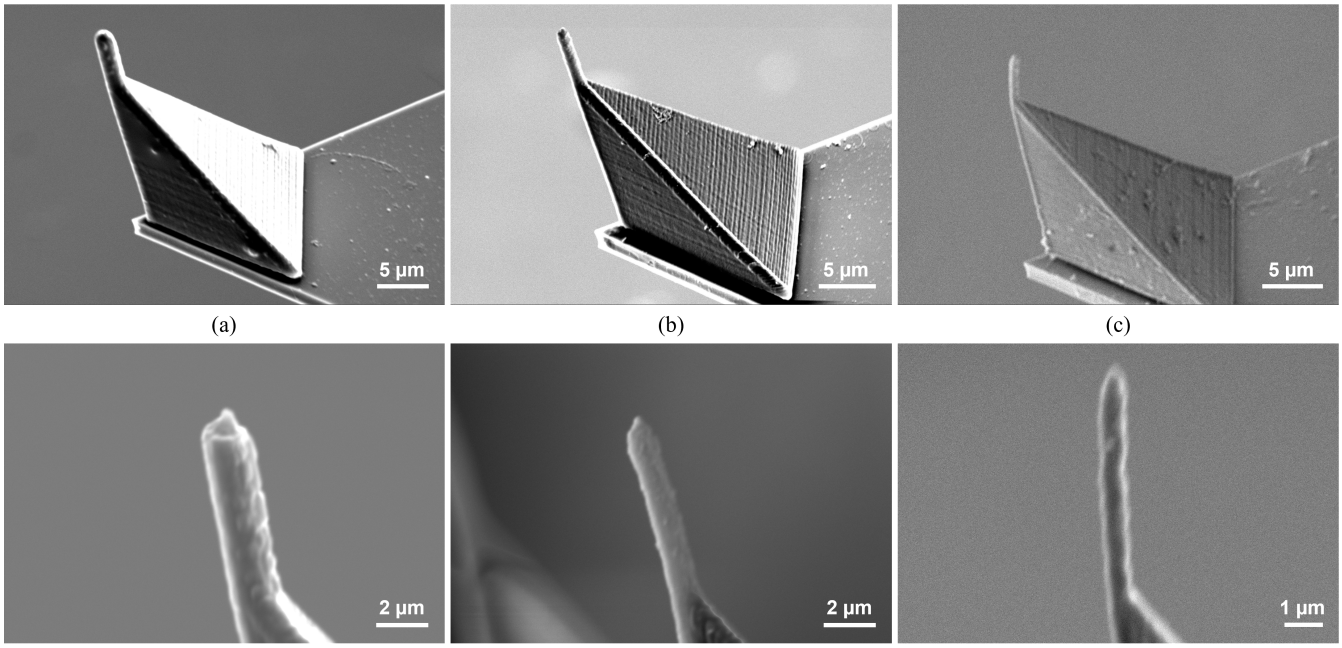

(a) (b) (c)

(d) (e) (f)

Fig. 8: SEM images of the 2, 1 and 0.7 (0.2) µm diameter tip, taken at a 45° angle (a, b, c), and taken from the side and close up (d, e, f)

µm lower than the design. The radius of curvature at the tip apex was much larger than expected for one voxel, averaging 263 nm with considerable uncertainty due to varying image resolution.

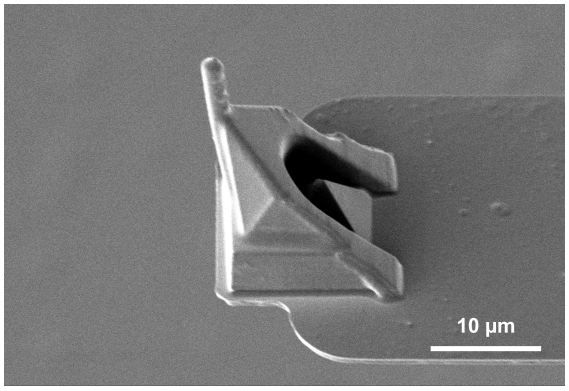

Fig. 9: SEM image of the altered tip design with diameter 2 µm printed on a re-used clogged microfluidic cantilever, taken at a 45° angle

Furthermore, for the 1 µm tip, the diameter was again consistent around 1 µm. The height was similarly consistent but offset by ∼0.5 µm. The radius of curvature was smaller than the 2 µm tip, averaging 130 nm with less uncertainty. Lastly, for the 0.2 µm tip, the diameter was consistent but had the value 0.7 µm, the smallest achievable with the 2PP printer for this design. The height was again consistent and only slightly deviating from the design. Finally, the radius of curvature at the tip apex was smaller than the 1 µm tip and was consistent around 105 nm.

TABLE II: Print evaluation of printed tips in terms of tip diameter (D), tip height (H) and tip apex radius (r)

	D (µm)	**H** (µm)	**r** (nm)
2 µm design	2	8	32
2 µm print	1.97 ± 0.09	7.13 ± 0.33	263 ± 192
1 µm design	1	7.5	32
1 µm print	1.07 ± 0.11	6.91 ± 0.39	130 ± 20
0.2 µm design	0.2	6.1	32
0.2 µm print	0.71 ± 0.08	5.97 ± 0.13	105 ± 15

Overall, the tips are good for use, as the prints are stable and consistent and have the correct diameter and sufficient height. However, the 0.2 µm tip is now referred to as the 0.7 µm tip, as the diameter deviated significantly from the design.

B. Force spectroscopy experiments on PDMS

Figure 10 depicts the force-distance curve corresponding to the the 3D printed tip coming into and out of contact with a PDMS sheet. A dip in the curve is observed during the extend and retract curve, corresponding to the cantilever snapping into contact with the surface as it comes in close proximity and due to adhesion forces as it retracts.

TABLE III: Mean effective Young's modulus of a PDMS sheet measured by the AFM and nanoindenter

	Mean Young's modulus (MPa)
AFM	5.892 ± 0.538
Nanoindenter	5.164 ± 0.057

The results from the Young's modulus calculations from the AFM and nanoindenter are shown in Table III. The means, 5.892 and 5.164 MPa, are in a similar range. Moreover, their order of magnitude is in agreement with the values found in literature, around 1 MPa [28]. The uncertainty for the nanoindenter is, as expected, significantly less than the AFM results, as it is made for doing very precise rheological measurements. Furthermore, a more suitable probe stiffness was chosen to match the elasticity of the material, whereas the micro-cantilever spring constant was chosen to match the cell elasticity.

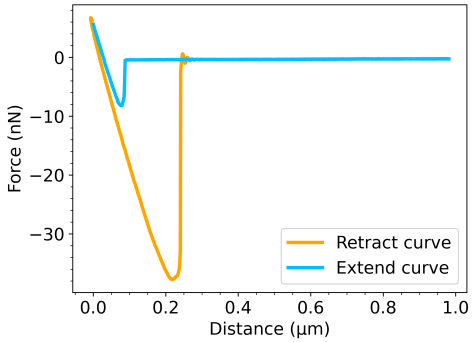

Fig. 10: A force-distance curve measured on a PDMS sample with a 2 µm tip

These tips are suitable for obtaining accurate force-distance data on cells, though the cylindrical part may break under lateral or excessive force. Therefore, imaging the probes after cell experiments is essential.

C. Contact point determination

Table IV shows the evaluation results for the best outcome in each method. For instance, the piecewise regression results only show the combination linear with a 7^{th} order polynomial because this had the best results compared to the other non-linear functions. The same holds for the RoV and derivative method, where N was optimal at 600. The full table of results are in Appendix B. The results show that the derivative method, with N being 600, performed the best in terms of the MAD error and small confidence interval.

TABLE IV: Evaluation of contact point determination methods using the mean absolute deviation (MAD) error and the confidence intervals (CI) 5 to 95% of the error

Method	MAD	CI 0.05	CI 0.95
Deviation from baseline	0.5691	0.0198	1.3698
Piecewise linear-polynomial 7	0.3883	0.0178	1.0930
RoV (N=600)	0.5504	0.0199	1.6830
Derivative (N=600)	0.1989	0.0086	0.3470

Since the contact point is the undeformed height of the cell at a specific location, the contact points can be plotted against the grid-position to obtain a height profile of a cell. Figure 11 shows a comparison of the manually determined ('real') height profile of a cell and the height profile automatically determined by the derivative method. The two colour maps are very similar, and thus the automatically determined contact points using the derivative method is suitable for this purpose.

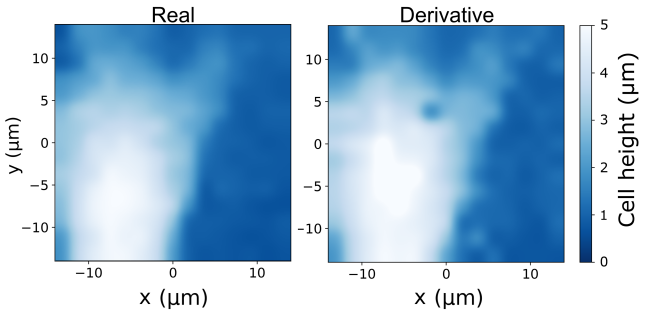

Fig. 11: Two colour maps showing the height profile of a cell, the real one being determined manually and the other automatically by the derivative method.

D. Force spectroscopy experiments on cells

In total, 72 cells were probed, resulting in 12,622 force-distance curves from the grid measurements. However, not all curves correspond to a cell, as some curves were taken on the surrounding hard substrate. For the statistical analysis, these must be filtered out by keeping the force-distance curves with contact point heights larger than 0.5 µm. The remaining number of force-distance curves then became 8,884.

Figure 12 shows a visualisation of the results of one grid measurement. This grid shows two cells next to each other. See Figure 12a for an optical image of the cells after the grid measurement were taken. The grid settings for this specific image were 20x20 points on an area of 50x50 µm. The diameter of the tip used was 2 µm, at a insertion velocity of 2 µm/s and with a spring constant of 0.326 N/m. Three other examples are included in Appendix C for the 1 µm, 0.7 µm and re-used microfluidic cantilever.

The cell height profile is plotted in Figures 12b and 12c in a 3D surface map and a 2D colour map, respectively. Two neighbouring cells are identified, with the highest parts of the cells reaching nearly 5 µm. As each pixel in the colour map corresponds to one force-distance curve, complementary plots were created to present the outcome of the dependent variables. Figure 12d visualises the number of insertion events per force-distance curve, showing that a single insertion event occurs on the centre area of the cell (height more than 2 µm), and up to three insertion events in the highest areas of the cell (more than 3 µm). Furthermore, Figures 12e, 12f, and 12g show the complementary plots of the force drop, insertion force, and indentation depth of the first insertion event, respectively. In this example, the results show that all first insertion events had similar force drop value (∼200 nN), insertion force (∼1.5 nN), and indentation depth (∼0.5 µm), except for a few outliers which are mainly located around the slanted areas of the cell.

Even though this example shows many successful insertion events, this was usually not the case. Figure 13 shows the distribution of the number of insertion events visualised in a histogram. The bin representing zero insertion events contains

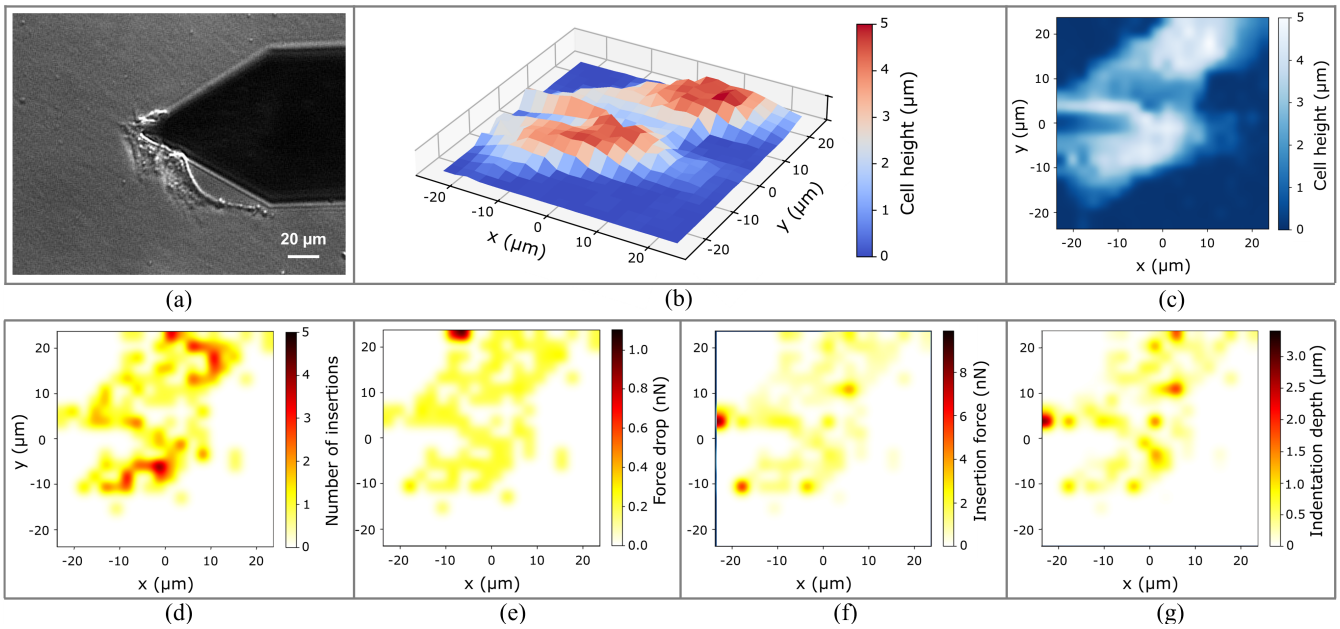

Fig. 12: One example of results obtained from one grid measurement on two cells; (a) shows the optical image of the cells with the cantilever at the end of the grid measurement; the cell height is plotted in (b) 3D and in (c) 2D; (d) visualises the number of insertion events, and (e) force drop, (f) insertion force and (g) indentation depth (g) of the first insertion event.

77% of the force-distance curves, suggesting that this occurs more often than observing at least one insertion event.

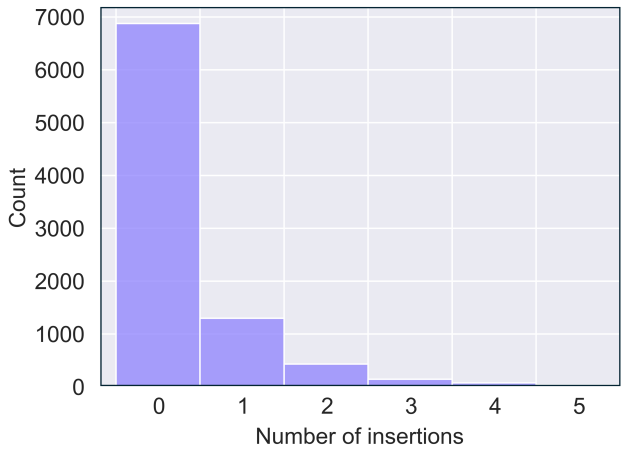

Fig. 13: Distribution of the number of insertion events of all the data

E. Statistics: number of insertion events

1) Cell height

To investigate the cell height effects on the number of insertion events all the 8,884 force-distance curves were included in the analysis. Figure 14 presents the stacked bar plot of cell height against the percentage of force-distance curves with a specific number of insertion events. Moreover, the total number of force-distance curves in each height bin is noted in white text inside the bar.

An increasing trend is observed between cell height and number of insertion events. Starting at a success rate of 10% in the smallest height bin (0.5-1 µm), reaching a local maximum at cell height bin 2.5-3 µm with 35% success rate and then slightly decreasing to finally reach the maximum at the highest bin (>5 µm) with 40% success rate. Moreover, two or more insertion events are only significantly observed above a cell height of 1.5 µm.

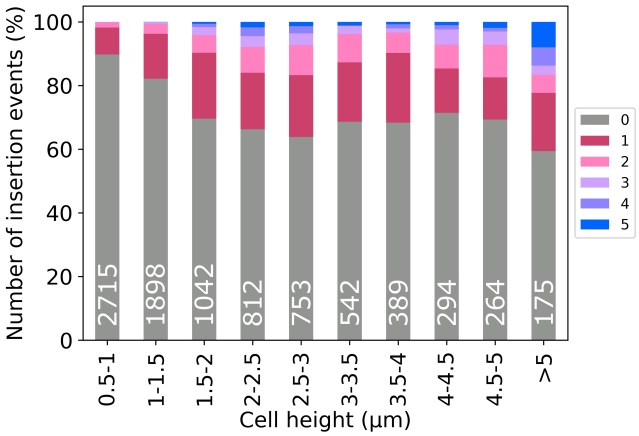

Fig. 14: Cell height effects on number of insertion events (percentage); the white text refers to the total number of force-distance curves in each bin

2) Tip diameter

To gain insight into the effects of tip diameter on the number of insertion events, the filtered data (v = 2 µm/s, k < 0.5 N/m) were included in the analysis, see Figure 15.

There is no clear trend between the three tip diameters and the number of insertion events since the percentages lie close. It may indicate that there is a lower success rate (25%) for the smallest 0.7 µm tip diameter, as compared to the 1 and 2 µm tip diameters (28%). However, this is unusual as 0.7 and 1 lie closer together than 1 and 2; so, the effect seen may be due to another effect, such as the spring constant of the cantilever. Therefore, the effects of tip diameter in the range of 0.7 to 2 µm remains inconclusive.

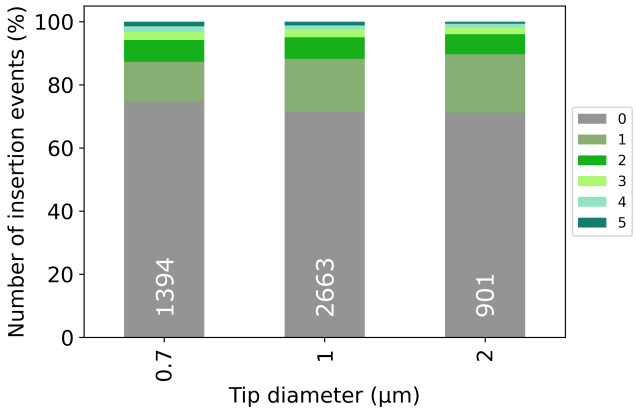

Fig. 15: Tip diameter effects on number of insertion events (percentage); the white text refers to the total number of force-distance curves in each bin

3) Insertion velocity

To look into the insertion velocity effects on the number of insertion events, the other filtered data (d = 2 µm, k $<$ 0.5 N/m) is analysed, see Figure 16.

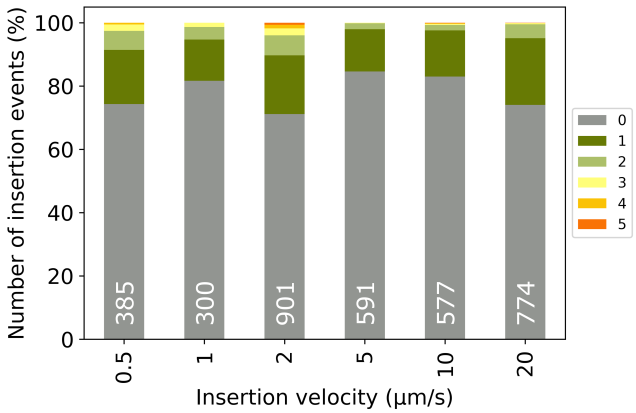

Fig. 16: Insertion velocity effects on number of insertion events (percentage); the white text refers to the total number of force-distance curves in each bin

There is no clear trend between the insertion velocities and the number of insertion events as the percentages fluctuate up to 10% throughout the tested velocities. It is unclear why there is a peak at 2 µm/s, with two other peaks at the extreme values for 0.5 and 20 µm/s, and a decrease for the velocities in-between. This observation does not account for interaction effects with cell height and spring constant, posing a significant limitation on this method. Therefore, the insertion velocity effects in the range of 0.5 to 20 µm/s are inconclusive.

4) Spring constant

To examine the spring constant effects on the number of insertion events, all force-distance curves were analysed, see Figure 17. The first spring constant bin, 0.022 N/m, defines a range of spring constants between 0.021 and 0.025 N/m. Moreover, as the spring constant could not be controlled in the experiments, the number of force-distance curves per bin is not equally distributed.

The last two bins correspond to the re-used clogged microfluidic cantilevers, and without these bins an increasing trend can be observed for the Arrow-TL cantilevers. The lowest spring constant bin with extremely flexible probes shows a success rate of only 20%, whereas the cantilever with a spring constant in the higher bin of 0.216 N/m shows a success rate of 40%, as well as a higher number of insertion events. Furthermore, the re-used microfluidic cantilevers with higher spring constants 0.5 and 1.1 N/m show chances of only 3-10%.

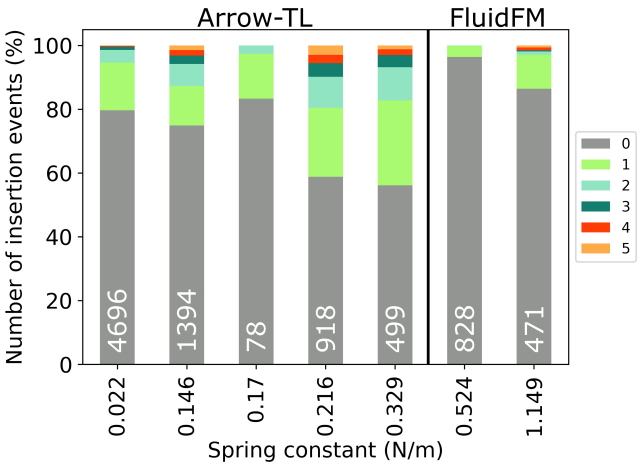

Fig. 17: Spring constant effects on number of insertion events (percentage); the white text refers to the total number of force-distance curves in each bin

F. Statistics: force drop, insertion force and indentation depth

The data is filtered to remove the points with zero insertion events, and the remaining amount of force-distance curves is 2,009. The correlation matrix heat map of the independent variables is depicted in Figure 18. It can be observed that cell height and tip diameter have a weak positive correlation, insertion velocity and tip diameter have a moderate positive correlation, and spring constant and insertion velocity have a weak negative correlation. Therefore, it cannot be assumed that the independent variables are independent. This makes it important that the multiple linear regression with interactions is applied because the effects on the outcome variables are always a sum of all the present independent variables and possible interactions between them. Multiple linear regression tries to isolate each independent variable to find their relative contributions to the whole; in this way, the independent

variables that have a significant effect on an outcome variable can be discriminated.

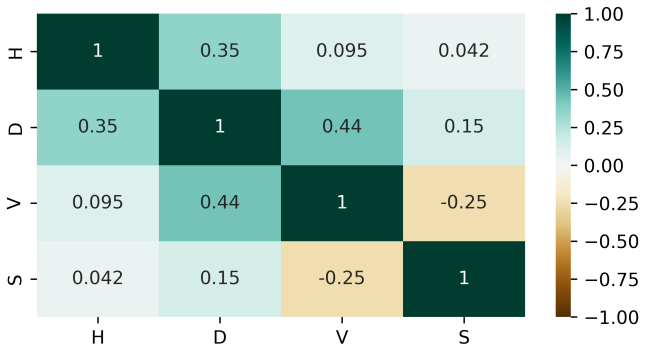

Fig. 18: The correlation matrix for all independent variables, visualised in a heat map

In addition, the outcome variables may also be correlated, as they are all measuring characteristics of the same insertion event. This can again be calculated using a correlation matrix and visualised in a heat map, see Figure 19. It can be noted that force drop and insertion force are quite strongly positively correlated, meaning that a higher force drop most likely also means a higher insertion force. Indentation depth is weakly correlated, which may indicate that a higher force drop does not necessarily occur paired with a higher indentation depth. However, between insertion force and indentation depth, there is a moderate positive correlation, indicating that a higher insertion force may be paired with a higher indentation depth.

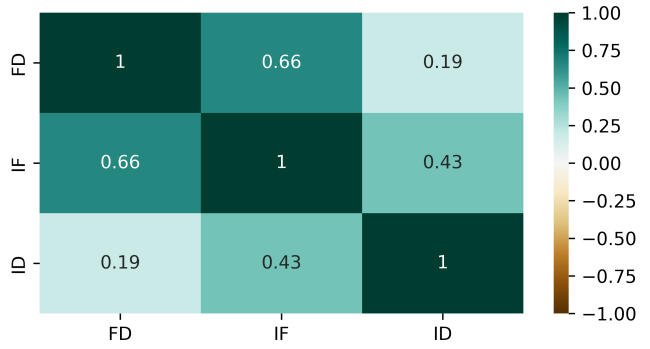

Fig. 19: The correlation matrix for the three outcome variables, visualised in a heat map

Following this, the results of the multiple linear regression with interactions are presented. The full results of the simple linear regression, multiple linear regression without interactions, and more details on the regression with interactions (BIC plots) are available in Appendix D.

The multiple linear regression model with interactions for each dependent variable was selected using the smallest BIC value. The final formulas are:

$$FD \sim H + D + H * D + H * S$$
$$IF \sim H + D + S + H * D + H * S + D * S$$
$$ID \sim H + D + H * S$$

TABLE V: Regression results for force drop (FD), insertion force (IF) and indentation depth (ID)

FD	**Coef**	**Std err**	**t**	**P**	**[0.025**	**0.975]**
y_0	0.3510	0.016	22.283	0.000	0.320	0.382
H	-0.4341	0.050	-8.689	0.000	-0.532	-0.336
D	-0.3145	0.036	-8.824	0.000	-0.384	-0.245
HxD	0.4836	0.067	7.209	0.000	0.352	0.615
HxS	0.4786	0.017	27.408	0.000	0.444	0.513
IF	**Coef**	**Std err**	**t**	**P**	**[0.025**	**0.975]**
y_0	1.6494	0.035	47.361	0.000	1.581	1.718
H	-0.5543	0.111	-4.999	0.000	-0.772	-0.337
D	-0.4520	0.093	-4.850	0.000	-0.635	-0.269
S	3.2550	0.254	12.829	0.000	2.757	3.753
HxD	0.8885	0.152	5.862	0.000	0.591	1.186
HxS	0.3475	0.080	4.355	0.000	0.191	0.504
DxS	-2.5847	0.260	-9.946	0.000	-3.094	-2.075
ID	**Coef**	**Std err**	**t**	**P**	**[0.025**	**0.975]**
y_0	0.8163	0.013	60.983	0.000	0.790	0.843
H	0.3514	0.015	22.761	0.000	0.321	0.382
D	-0.0689	0.014	-4.795	0.000	-0.097	-0.041
HxS	-0.0452	0.015	-3.056	0.002	-0.074	-0.016

The regression results for these formulas are given in Table V. The results are statistically significant (P<0.05), and the confidence intervals are small. The insertion velocity and all interaction variables including the insertion velocity did not end up in the selected formulas for the multiple linear regression. This was mainly due to the results being statistically insignificant because of large P-values (P>0.05), which led to the variables being excluded from the formulas. This does not suggest that insertion velocity has no effect on the outcome variables, only that it remains inconclusive.

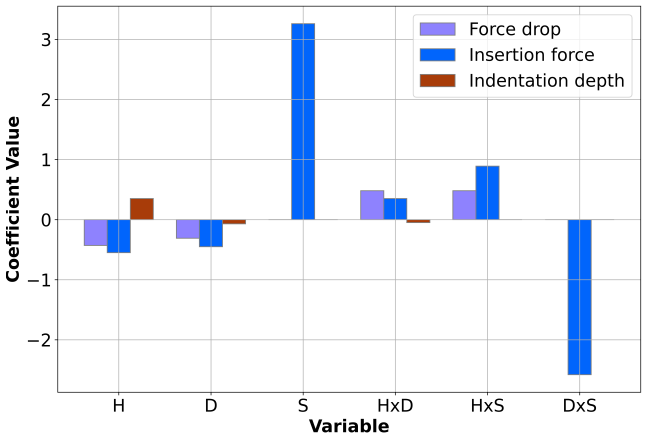

Fig. 20: Summary of the coefficients values found in the multiple linear regression for the independent variables and interaction terms for force drop, insertion force and indentation depth

The coefficients each provide a contribution to explain the data, and these coefficients are summarised per independent variable and interaction variable in Figure 20. It was found

that cell height (H) on its own decreases the force drop and the insertion force, however increases the indentation depth. Tip diameter (D) on its own decreases the force drop and the insertion force and slightly decreases the indentation depth. Spring constant of the cantilever greatly increases the insertion force, whereas the force drop and indentation depth remain inconclusive.

Looking at the interaction variables, it was found that increasing tip diameter in combination with increasing cell height has an extra increasing effect on the insertion force and force drop. Similarly, the spring constant in combination with cell height also results in an extra increase in insertion force and force drop, as well as a slight decrease in indentation depth. Finally, the tip diameter and spring constant result in an extra decrease in the insertion force.

The relationships have been found for height, tip diameter, and spring constant of the cantilever. The mean values for force drop, insertion force and indentation depth have been mentioned here to better grasp these relationships (see Table VI). As the tip diameter is increased from 0.7 to 2 μm, the force drop decreases from $\sim$600 pN to $\sim$250 pN. Also, the insertion force decreases from $\sim$2.5 nN to $\sim$1.5 nN, and the indentation depth only slightly decreases from $\sim$900 nm to $\sim$600 nm.

TABLE VI: The mean values of force drop (FD), insertion force(IF) and indentation depth (ID) as tip diameter increases from 0.7 to 2 μm and as spring constant increases from 0.022 to 0.216 N/m

D (μm)	**Mean FD** (nN)	**Mean IF** (nN)	**Mean ID** (μm)
0.7	0.64	2.52	0.89
2	0.25	1.53	0.63
S (N/m)	**Mean FD** (nN)	**Mean IF** (nN)	**Mean ID** (μm)
0.022	0.04	0.52	0.83
0.216	0.28	2.38	0.77

Furthermore, as the spring constant increases from 0.02 to 0.2 N/m the mean force drop increases from $\sim$40 pN to $\sim$300 pN. Moreover, the insertion force increases from $\sim$0.5 nN to $\sim$2.5 nN, and the indentation depth remains approximately equal at $\sim$800 nm.

IV. Discussion

A. Fabrication of custom 3D printed tips

Two-photon polymerisation has proven to be a versatile technique to print on top of microcantilevers. The smallest tip diameter which the printer was able to print was 700 nm, however, in literature smaller feature size of 400 nm and tip apex radius of curvature of 30 nm have been reported which better match the theoretical values [29]. A possible reason for the difference is the use of different resin and design of the tip. A slanted tip was designed to compensate for the angled AFM cantilever holder, however, the resolution of the laser voxel is higher in the horizontal plane as compared to the vertical plane. Therefore, printing a tip which is vertical may yield smaller feature sizes.

The 3D printed tips have been successfully employed for force spectroscopy on mouse preosteoblast cells in a liquid environment. Therefore, 2PP can provide extra design freedom to practitioners of single-cell sampling to create their own custom microfluidic tips.

B. Algorithms for data processing and analysis

The algorithms that have been written for this specific research has shown accurate and fast data processing results that was not previously possible with existing algorithms. The algorithms could be compared to open-source Python packages such as Nanite [30] and PyFMLab [31] that also analyse force spectroscopy data on cells, however their focus is much more on rheological analysis and not insertion event analysis.

Limitations still exist for the algorithms written for this research. For instance, the contact point determination algorithm has shown very accurate results, but still an error of 200 nm, thus improvements as always possible. Secondly, the force drop detection algorithm based on finding prominent peaks has potential to be greatly improved. During this study, the algorithm also detected small force drops which were likely not insertion events. An improved method could select the correct force drops linked to an insertion event more accurately. However, as it is difficult to verify which force drop is linked to an actual insertion event, finding this improved method becomes a complex problem.

C. Statistical analyses

The force spectroscopy data has been analysed for trends between the independent variables and the dependent variables. First, the bar charts were used to analyse the effects of the independent variables on the number of insertion events, which gave insights into the success rates. Second, multiple linear regression has been employed to analyse the effects of the independent variables on the force drop value, insertion force and indentation depth of to an insertion event. Multiple linear regression is useful but difficult to implement without proper physical interpretation. The following section attempts per independent variable to offer insights as to why certain behaviour is observed. This research does not provide concrete causal relationships since that would require more rigorous analysis.

1) Cell height

The bar chart analyses have shown that an increase in cell height increases the occurrence of at least one insertion event (higher success rate). This may be due to indentation depths not exceeding the depth of the cell itself at higher cell heights. So, at lower cell heights, the cell may be more likely to deform completely as the tip indents it, than keep its shape and allow the tip to insert through the cell membrane.

Furthermore, the bar chart shows a slight decrease of success rate between cell heights 3 to 5 μm. This decrease could be due to the number of insertion events not being so much affected by the absolute cell height, but rather the normalized cell height, which is a function of the maximum height of the cell on which the data was collected. The average cell height for mouse preosteoblasts is around 3.5 μm. This may explain

the accumulation of higher insertion events around 2 to 3 µm. The following decrease and plateau between cell heights 3 to 5 µm relates to a variety of larger cells, wherein both maximum cell heights are combined with non-maximum cell heights, possibly causing the number of insertion events to be more constant. Then, in the highest height bin, >5 µm, the data most likely only relates to the maximum cell height. Therefore, this could explain the high number of insertion events observed.

From the multiple linear regression, it was found that cell height alone decreases the force drop value and the insertion force; however, it increases the indentation depth. Out of all the possible relationships, the indentation depth may be the most logical and intuitive one. The thicker the cell, the more material to displace and indent into. Thin parts of the cell can never reach indentation depths larger than their own thickness. However, at high parts of the cell, small indentation depths also still occur.

The insertion force decrease may be explained by the cell's material properties at different cell heights/locations. For example, the nucleus is known to be stiff relative to the cell itself. Also, the thinner areas appear stiffer due to the hard cell-support substrate. When plotting cell height against the apparent Young's modulus (Figure 21), it was found that the lower parts of the cell appear, in general, stiffer than the higher parts of the cell. Thus, the high parts of the cell will require less force for the insertion than the lower parts of the cell. This idea agrees with theories in the literature, such as the cell finite-thickness effect analysed in Garcia et al. (2020) [32].

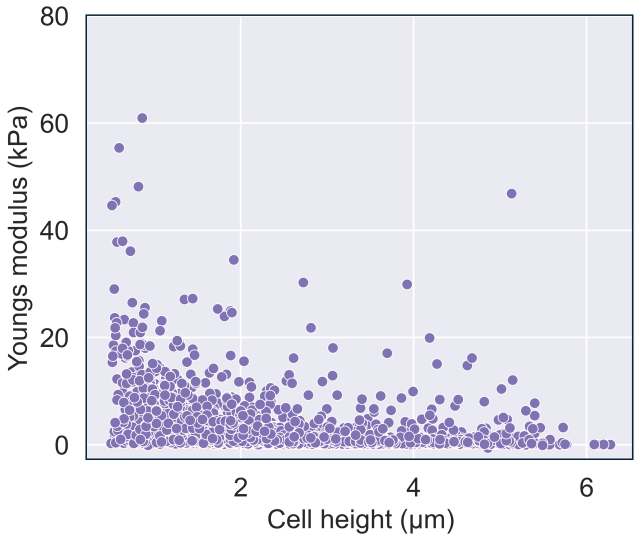

Fig. 21: Scatter plot of cell height against the apparent Young's modulus showing that at higher cell height the cell appears softer

Moreover, lower insertion force inherently means that the cantilever is less deflected, and the force drop will be less as compared to an insertion with higher insertion force. This can possibly explain the decrease in the force drop observed as an effect of cell height.

2) Tip diameter

The bar chart analyses have shown that the effects of tip diameter in the range of 0.7 to 2 µm on the insertion success rate remain inconclusive. The expectation was that a thinner tip diameter would result in higher success rates [10]. This effect was however not observed, possibly caused by the small range of diameters chosen in the experiment design, or the effects of the cantilever spring constant, which could not be controlled throughout the experiments.

One would expect that an increase in tip diameter increases the insertion force, as there is a larger surface area that is trying to penetrate the membrane. The multiple linear regression showed that the increase in tip diameter alone decreases the force drop value and the insertion force and slightly decreases the indentation depth. Most likely, there is an underlying reason why this behaviour is observed. One idea is that the small force drops identified in the force-distance curves with larger tip diameters may not correspond to an actual insertion event but result from the movement of structures inside the cell, such as the cytoskeleton [13]. The larger tip diameter probes are more prone to this occurrence because their indentation depth is much larger, and they will start to affect the underlying cytoskeleton before penetrating the cell membrane.

That the force drop effect is slightly decreasing for larger tip diameters may be linked to the insertion force. The lower the insertion force, the smaller the deflection of the cantilever, and the smaller the force drop as the cantilever springs back towards its original shape. In addition, the force drop may also be linked to the spring constant of the cantilever used in the experiment. When plotting tip diameter against spring constant (Figure 22), one can observe that lower spring constants were linked to the 0.7 and 1 µm tip than the 2 µm tip. A more flexible cantilever will deflect more, possibly resulting in a larger force drop.

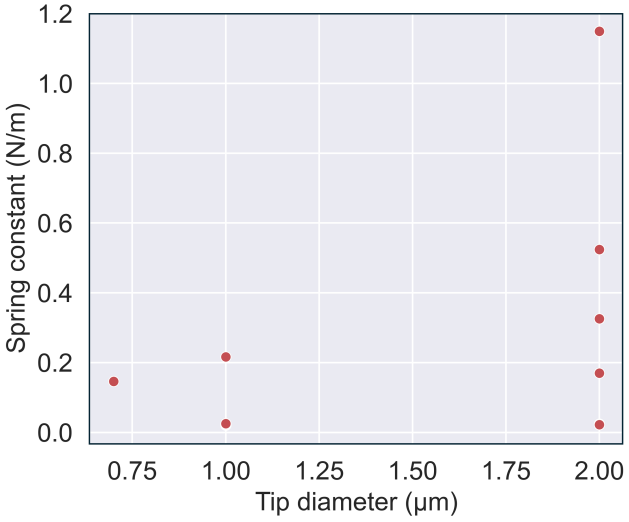

Fig. 22: Scatter plot of tip diameter against spring constant showing that the spring constants varied between different cantilevers and were in general lower for the 0.7 and 1 µm tips

On the contrary, increasing tip diameter and cell height together results in an extra increase in insertion force and force drop. This means that when using a larger tip diameter, it is best to choose the highest parts of the cell to increase these values.

Furthermore, it is counterintuitive that an increase in tip diameter decreases the indentation depth. A larger indentation depth is expected for the larger tip diameter [10]. Even though the regression model shows that this effect is very small, it is still a measurable effect. This may also be linked to the low insertion forces observed for the larger tip, which also occurred at small indentation depths.

Looking at the values, as the tip diameter is increased from 0.7 to 2 µm, the insertion force decreases from ∼2.5 nN to ∼1.5 nN, and the indentation depth only slightly decreases from ∼900 nm to ∼600 nm. These values are comparable to the insertion forces and indentation depths recorded in other studies for similar probe sizes (different cells) [9], and these values are much lower than the typical pyramid type probes [33]. Also, the force drop increase from around ∼250 pN ∼600 pN when the tip diameter is reduced, are comparable to the results found in Bitterli (2012) [9].

3) Spring constant

The bar chart analyses shows an increasing trend from 20 to 40% in success rate for the Arrow-TL cantilevers with higher spring constant. However, this is likely not an ever-increasing trend line. It is expected that the trend line starts to decrease again after a certain point, because very stiff cantilevers are expected to not be able to "feel" the cell at all.

Furthermore, the re-used microfluidic cantilevers with higher spring constants 0.5 and 1.1 N/m show success rates of only 3-10%. It is unknown if the spring constant is the dominating effect or some other factors inherent to using a completely different probe. One possibility is that this was due to the re-used microfluidic cantilever measurements being more noisy. Figure 23 compares two typical force-distance curves from both cantilevers. The noisy signal of the re-used microfluidic cantilever could be due to the laser signal being weaker due to the higher transparency of the material, as compared to the Arrow-TL cantilever. A noisy signal results in difficult identification of contact point and insertion events, leading to inaccurate results for the spring constant effect. Therefore, the re-used microfluidic cantilevers cannot be compared to the Arrow-TL cantilevers.

From the multiple linear regression, it was found that the spring constant increases the insertion force, while the force drop value and indentation depth remain inconclusive. Intuitively, one would expect the insertion force to remain constant for the same tip diameter, no matter the spring constant of the probe; if the probe reaches a certain force, an insertion event occurs. However, the analyses show that a higher spring constant increases the insertion force. A possible explanation is that it is the force loading rate that is affecting the insertion force. The loading rate (N/s) can be calculated by multiplying the spring constant (N/m) by the piezo velocity (m/s). The higher the spring constant, the higher the force for the same unit of displacement, as compared to a low spring constant. The loading rate is a more logical explanation for the

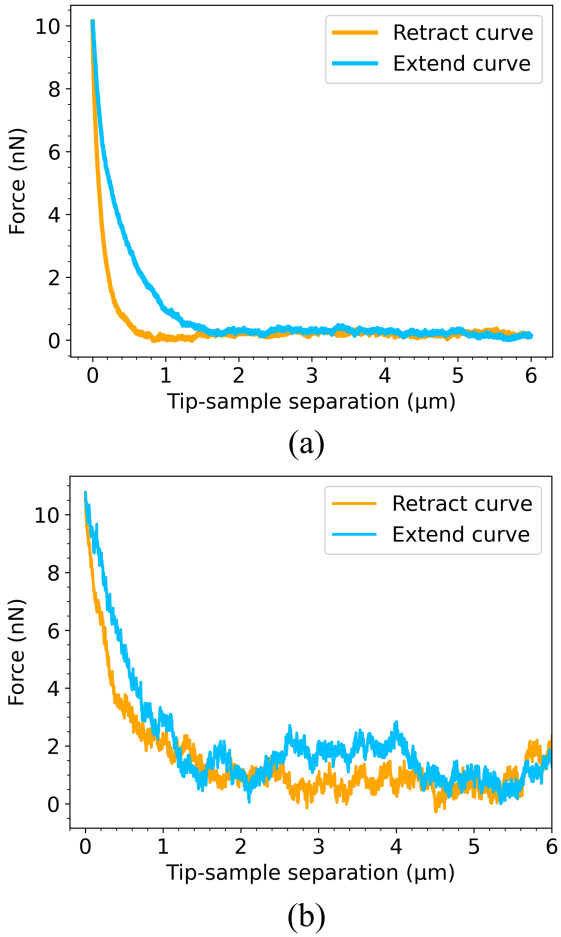

Fig. 23: Showing typical force-distance curve obtained from (a) the Arrow-TL cantilever and (b) the re-used FluidFM cantilever

increase in insertion force, as the cell is sensitive to changes in force, reacting differently to how fast the force changes. In this case, the cell requires higher forces to insert the tip at faster loading rates and lower forces at lower loading rates. This has also been observed in literature [12, 34].

In addition, the spring constant, in combination with cell height, also results in an extra increase in insertion force. Before, it was mentioned that increased cell height decreases the insertion force, but in combination with a higher spring constant, the insertion force is slightly higher. This may be interpreted as a higher loading rate on the highest (and softest) part of the cell, resulting in higher insertion forces than on the cell edges (stiffer) with slower loading rates.

Furthermore, tip diameter and spring constant together also have an extra effect on the insertion force. Namely, a thinner tip diameter combined with a more flexible cantilever results in higher insertion forces than a larger tip diameter with a stiffer cantilever. So, in this case, a thinner tip, which theoretically requires less force to penetrate the cell membrane, should be combined with a more flexible cantilever to obtain more accurate measurements. Higher insertion forces may also lead to higher force drops, as it was shown that they are correlated.

The effect of spring constant on the force drop remains inconclusive even though a clear effect is to be expected. A more flexible cantilever is more sensitive to small changes in force, and for the same amount of force, the deflection of the cantilever is higher, and thus amplifying the force drop. The interaction model could not conclude anything about the individual effect of the spring constant on the force drop, but the spring constant, together with cell height, does seem to increase the force drop value. This could be interpreted as a stiffer cantilever and high cell height combined, resulting in a larger force drop, whereas a more flexible cantilever with lower cell heights results in smaller force drops.

The indentation depth is also expected to change with the spring constant. From the literature, the lower the spring constant, the larger the indentation depth [12]. From the interaction model again, the individual effect of spring constant on indentation depth remains inconclusive. However, in combination with cell height there seems to be a small additional effect. Increasing the two together may actually decrease the indentation depth slightly, which is more in line with what was described in literature [12]. The effect may be small because the range tested was small (0.02-1.1 $\mathrm{N/m}$), whereas Kwon et al. (2009) tested two different spring constants 0.26 and 23 $\mathrm{N/m}$, observing a much more pronounced effect. Moreover, because it is an interacting effect, nothing can be said about which of the two variables is mainly causing this extra effect.

4) Insertion velocity

The bar chart analyses shows that the insertion velocity effects on the success rate in the range of 0.5 to 20 $\mu\mathrm{m/s}$ are inconclusive. Similarly, for the multiple linear regression, the insertion velocity variable was excluded from the model as it was not giving any significant results.

An idea as to why the insertion velocity experiments were so inconclusive is that the spring constant used for those experiments was very low (0.02 $\mathrm{N/m}$), which in turn resulted in a very slow force loading rate. As mentioned, the loading rate can be calculated by multiplying the spring constant by the piezo (insertion) velocity. If this is applied to the velocity experiments for piezo velocities 0.5, 1, 2, 5, 10 and 20 $\mu\mathrm{m/s}$ and spring constant 0.02 $\mathrm{N/m}$, the loading rates become 10, 20, 40, 100, 200 and 400 μN/s, respectively. If this is compared to the other data where the spring constant was 0.3 $\mathrm{N/m}$ and the piezo velocity was only 2 $\mu\mathrm{m/s}$, the loading rate was 600 μN/s. Moreover, it was found that the loading rate (or spring constant) greatly affects the insertion force, which means that low loading rates result in lower insertion forces. Also, the low loading rate shows poor insertion success rates. The velocity experiments are likely completely dominated by this loading rate effect.

On the other hand, the loading rate is actually the insertion velocity, so indirectly, the insertion velocity is studied, which results in some individual effects on the insertion force. This aligns with what was found in the literature, namely that the cell behaves more solid and elastic-like at faster velocities and more fluid and viscous-like at slower velocities [35, 3].

V. Conclusion

The aim of this paper is to improve the quantifiability and reproducibility of a cell membrane insertion event using force spectroscopy on mouse preosteoblast cells (MC3T3-E1). To reach this goal the following objectives have been defined: (1) the microfabrication of custom tips with varying diameter on commercial cantilevers, (2) The creation and evaluation of algorithms tailored to process and analyse force-distance curves corresponding to cell membrane insertion, (3) The analysis of variables that affect the occurrence of insertion events, (4) The application of statistical analysis such as multiple linear regression to find individual and interacting effects of the factors that influence insertion event characteristics.

During the research, custom tips have been fabricated on commercial tipless microcantilevers using 3D printing with two-photon polymerisation. The tip design consists of a cylindrical tip with a sharp cone end, on top of a pyramidal base. The design corrects for the 11° tilt in the cantilever holder, avoids interference between pyramidal base and cell because of the high aspect ratio of the cylindrical tip, and enables tip visibility during use. The tip diameters, height and radius of curvature at the tip apex have been measured, where the tip diameters are 0.7, 1 and 2 $\mu\mathrm{m}$, with heights of 6, 7 and 7 $\mu\mathrm{m}$, and radii of 260, 130 and 100 nm, respectively. These custom tips were successfully used in single-cell force spectroscopy experiments, to find the influence of four factors: cell height, tip diameter, insertion velocity and cantilever spring constant.

Furthermore, new algorithms have been created and evaluated to automatically process and detect the contact point, hard substrate contact point, and, if present, the number of insertion events, giving insights into the reproducibility of insertion events. Additionally, an algorithm is able to measure the force drop value, insertion force and indentation depth of the first insertion event, providing information about the quantifiability of the insertion event. The automatic and accurate detection of the contact point was especially challenging, where existing methods proved insufficient without manual tweaking of parameters. During the research, a new algorithm has been developed based on taking derivatives to reproducibly and accurately detect the contact point. This algorithm was also evaluated against three other algorithms and was found to perform the best with a mean absolute deviation of below 200 nm.

Finally, to find the individual and interacting effects of the four factors on the occurrence and characteristics of the insertion event, bar charts and multiple linear regression have been applied to all the force-distance curves. The data consisted of 9,000 force-distance curves collected from 75 cells. The results of this research demonstrate that selecting large cells (5 $\mu\mathrm{m}$) and the highest location on the cell, increases force drop occurrence from 10% to 40% while decreases the force drop visibility. This is often also paired with a decrease in insertion force and an increase in indentation depth. This behaviour might be explained due to local cell elasticity differences based on the thickness of the cell.

Furthermore, cantilevers with a spring constant of 0.2 $\mathrm{N/m}$ achieved higher force drop occurrence (40%) and visibility

($\sim$300 pN), compared to more flexible cantilevers with a spring constant of 0.02 N/m (20% occurrence, $\sim$40 pN visibility). An increase in the spring constant resulted in higher insertion forces. This behaviour may be explained by the inherent change in the loading rate of the force as the spring constant is changed. Thus, for a specific cell, the piezo insertion velocity must be tuned to the cantilever spring constant to obtain an optimal loading rate.

Also, while decreasing the tip diameter from 2 to 0.7 µm did not affect the occurrence rate, it did increase force drop visibility from $\sim$250 to $\sim$600 pN. This was paired with an increase in insertion force of $\sim$1 nN.

In general, it was found that a larger force drop is often paired with higher insertion forces and that cell height and cantilever spring constant are important factors that influence the quantifiability (visibility) of cell membrane insertion events. These findings provide valuable insights for optimising experimental parameters in single-cell analysis techniques that require physical puncturing of the cell membrane.

References

[1] Prithwidip Saha, Tal Duanis-Assaf, and Meital Reches. "Fundamentals and Applications of FluidFM Technology in Single-Cell Studies". In: *Advanced Materials Interfaces* 7 (23 Dec. 2020). ISSN: 21967350. DOI: 10.1002/admi.202001115.

[2] Ricardo Garcia. "Nanomechanical mapping of soft materials with the atomic force microscope: Methods, theory and applications". In: *Chemical Society Reviews* 49 (16 Aug. 2020), pp. 5850–5884. ISSN: 14604744. DOI: 10.1039/d0cs00318b.

[3] Andreas Janshoff. "Viscoelastic properties of epithelial cells". In: *Biochemical Society Transactions* 49 (6 Dec. 2021), pp. 2687–2695. ISSN: 14708752. DOI: 10.1042/BST20210476.

[4] Amir Farokh Payam and Ali Passian. "Imaging beyond the surface region: Probing hidden materials via atomic force microscopy". In: *Science Advances* 9 (2023). A review paper. URL: https://www.science.org.

[5] Marcos Penedo et al. "Visualizing intracellular nanostructures of living cells by nanoendoscopy-AFM". In: *Sci. Adv* 7 (2021), p. 4990. URL: https://www.science.org.

[6] Orane Guillaume-Gentil et al. "Single-Cell Mass Spectrometry of Metabolites Extracted from Live Cells by Fluidic Force Microscopy". In: *Analytical Chemistry* 89 (9 May 2017), pp. 5017–5023. ISSN: 15206882. DOI: 10.1021/acs.analchem.7b00367.

[7] Christoph G. Gäbelein et al. "Mitochondria transplantation between living cells". In: *PLoS Biology* 20 (3 Mar. 2022). ISSN: 15457885. DOI: 10.1371/journal.pbio.3001576.

[8] Annie Sahota et al. "Recent advances in single-cell subcellular sampling". In: *Chemical Communications* 59 (36 May 2023), pp. 5312–5328. ISSN: 1364-548X. DOI: 10.1039/D3CC00573A. URL: https://pubs-rsc-org.tudelft.idm.oclc.org/en/content/articlehtml/2023/cc/d3cc00573a%20https://pubs-rsc-org.tudelft.idm.oclc.org/en/content/articlelanding/2023/cc/d3cc00573a.

[9] Bitterli. Joanna Katarzyna. "AFM Based Single Cell Microinjection: Technological Developements, Biological Experiments and Biophysical Analysis of Probe Indentation". In: (2012).

[10] Marcos Penedo et al. "Cell penetration efficiency analysis of different atomic force microscopy nanoneedles into living cells". In: *Scientific Reports* 11 (1 Dec. 2021). ISSN: 20452322. DOI: 10.1038/s41598-021-87319-3.

[11] Guocheng Zhang et al. "Study of the Effect of Cell Prestress on the Cell Membrane Penetration Behavior by Atomic Force Microscopy". In: *Micromachines* 14 (2 Feb. 2023). ISSN: 2072666X. DOI: 10.3390/mi14020397.

[12] Eun Young Kwon, Young Tae Kim, and Dae Eun Kim. "Investigation of penetration force of living cell using an atomic force microscope". In: *Journal of Mechanical Science and Technology* 23 (7 2009), pp. 1932–1938. ISSN: 1738494X. DOI: 10.1007/s12206-009-0508-z.

[13] Matthew R. Angle et al. "Penetration of cell membranes and synthetic lipid bilayers by nanoprobes". In: *Biophysical Journal* 107 (9 Nov. 2014), pp. 2091–2100. ISSN: 15420086. DOI: 10.1016/j.bpj.2014.09.023.

[14] Gerald Göring et al. "Tailored probes for atomic force microscopy fabricated by two-photon polymerization". In: *Applied Physics Letters* 109 (6 Aug. 2016), p. 63101. ISSN: 00036951. DOI: 10.1063/1.4960386/32602. URL: /aip/apl/article/109/6/063101/32602/Tailored-probes-for-atomic-force-microscopy.

[15] Robert C.L.N. Kramer et al. "Multiscale 3D-printing of microfluidic AFM cantilevers". In: *Lab on a Chip* 20 (2 Jan. 2020), pp. 311–319. ISSN: 14730189. DOI: 10.1039/c9lc00668k.

[16] Ayoub Glia, Muhammedin Deliorman, and Mohammad A. Qasaimeh. "FluidTIP for High-Resolution Imaging and Enhanced Micro- and Nano-Scale Biomanipulations in Atomic Force Microscopy". In: *2023 International Conference on Manipulation, Automation and Robotics at Small Scales (MARSS)*. IEEE, Oct. 2023, pp. 1–6. ISBN: 979-8-3503-3039-7. DOI: 10.1109/MARSS58567.2023.10294147. URL: https://ieeexplore.ieee.org/document/10294147/.

[17] Caroline A Schneider, Wayne S Rasband, and Kevin W Eliceiri. "NIH Image to ImageJ: 25 years of image analysis". In: *Nature Methods* 9.7 (June 2012), pp. 671–675. DOI: 10.1038/nmeth.2089. URL: https://www.nature.com/articles/nmeth.2089.

[18] Małgorzata Lekka. "Discrimination Between Normal and Cancerous Cells Using AFM". In: *BioNanoScience* 6.1 (Jan. 2016), pp. 65–80. DOI: 10.1007/s12668-016-0191-3. URL: https://doi.org/10.1007/s12668-016-0191-3.

[19] *afmformats*. URL: https://afmformats.readthedocs.io/en/stable/ (visited on 11/11/2024).

[20] Núria Gavara. "Combined strategies for optimal detection of the contact point in AFM force-indentation

curves obtained on thin samples and adherent cells". In: *Nature Publishing Group* (2016). DOI: 10.1038/srep21267. URL: www.nature.com/scientificreports.

[21] *JPK DP Data Processing Software Manual*. Version 4.2. Available at https://www.nanophys.kth.se/nanolab/afm/jpk/manuf-manuals/DPmanual.4.2.pdf. JPK Instruments AG. Oct. 2012.

[22] A. Yew. *Numerical differentiation: finite differences*. Last accessed 19 November 2024. 2011. URL: https://www.dam.brown.edu/people/alcyew/handouts/numdiff.pdf.

[23] Pauli Virtanen et al. "SciPy 1.0: Fundamental Algorithms for Scientific Computing in Python". In: *Nature Methods* 17 (2020), pp. 261–272. DOI: 10.1038/s41592-019-0686-2.

[24] S. V. Kontomaris, A. Malamou, and A. Stylianou. "The Hertzian theory in AFM nanoindentation experiments regarding biological samples: Overcoming limitations in data processing". In: *Micron* 155 (Apr. 2022). ISSN: 09684328. DOI: 10.1016/j.micron.2022.103228.

[25] Ludwig C. Nitsche. *Ordinary Least Squares Linear Regression: Flaws, Problems and Pitfalls*. Last accessed 19 November 2024. 2009. URL: https://lcn.people.uic.edu/classes/che205s17/docs/che205s17_reading_06c.pdf.

[26] Lawrence Joseph. *Interactions in Multiple Linear Regression*. Last accessed 19 November 2024. URL: https://www.medicine.mcgill.ca/epidemiology/joseph/courses/EPIB-621/interaction.pdf.

[27] Sadanori Konishi and Genshiro Kitagawa. *Information Criteria and Statistical Modeling*. Springer Science+Business Media, Sept. 2007. DOI: 10.1007/978-0-387-71887-3. URL: https://doi.org/10.1007/978-0-387-71887-3.

[28] Edoardo Rubino and Tindaro Ioppolo. "Young's modulus and loss tangent measurement of polydimethylsiloxane using an optical lever". In: *Journal of Polymer Science Part B Polymer Physics* 54.7 (Dec. 2015), pp. 747–751. DOI: 10.1002/polb.23972. URL: https://doi.org/10.1002/polb.23972.

[29] Ayoub Glia, Muhammedin Deliorman, and Mohammad A. Qasaimeh. "3D Generation of Multipurpose Atomic Force Microscopy Tips". In: *Advanced Science* 9 (27 Sept. 2022). ISSN: 21983844. DOI: 10.1002/advs.202201489.

[30] Paul Müller et al. "Nanite: Using machine learning to assess the quality of atomic force microscopy-enabled nano-indentation data". In: *BMC Bioinformatics* 20 (1 Sept. 2019). ISSN: 14712105. DOI: 10.1186/s12859-019-3010-3.

[31] Javier López-Alonso et al. "PyFMLab: Open-source software for atomic force microscopy microrheology data analysis [version 2; peer review: 2 approved]". In: *Open Research Europe* 3 (187 2024). DOI: 10.12688/openreseurope.16550.1. URL: https://doi.org/10.12688/openreseurope.16550.1.

[32] Pablo D. Garcia, Carlos R. Guerrero, and Ricardo Garcia. "Nanorheology of living cells measured by AFM-based force-distance curves". In: *Nanoscale* 12 (16 Apr. 2020), pp. 9133–9143. ISSN: 20403372. DOI: 10.1039/c9nr10316c.

[33] Orane Guillaume-Gentil et al. "Force-Controlled Fluidic Injection into Single Cell Nuclei". In: *Small* 9 (11 June 2013), pp. 1904–1907. ISSN: 1613-6829. DOI: 10.1002/SMLL.201202276. URL: https://onlinelibrary-wiley-com.tudelft.idm.oclc.org/doi/full/10.1002/smll.201202276%20https://onlinelibrary-wiley-com.tudelft.idm.oclc.org/doi/abs/10.1002/smll.201202276%20https://onlinelibrary-wiley-com.tudelft.idm.oclc.org/doi/10.1002/smll.201202276.

[34] Lei Wang et al. "Effect of AFM nanoindentation loading rate on the characterization of mechanical properties of vascular endothelial cell". In: *Micromachines* 11 (6 June 2020). ISSN: 2072666X. DOI: 10.3390/MI11060562.

[35] Yuri M. Efremov et al. "Measuring nanoscale viscoelastic parameters of cells directly from AFM force-displacement curves". In: *Scientific Reports* 7 (1 Dec. 2017). ISSN: 20452322. DOI: 10.1038/s41598-017-01784-3.

Outlook

6.1. Thesis conclusion

A literature study is conducted to review the use of AFM with solid and microfluidic microcantilevers for single-cell analysis, focussing on single-cell injection and biopsy and the technical challenges involved. For instance, the large forces (>20 nN) required to penetrate the cell membrane can cause irreversible damage; and the large indentation depths, which usually reach half of the cell height, significantly reduce the spatial resolution when targeting a specific subcellular component. Most importantly, the reproducibility of results is extremely low, mainly due to the natural cell-to-cell variability but also due to the low cell membrane penetration success rate. This success rate for typical microfluidic cantilever probes is usually around 13%, mainly owing to the large size of the pyramidal tip.

As single-cell biopsy consists of the insertion of the microcantilever tip through the cell membrane, potentially influencing factors on this insertion event are reviewed for improvements in success rate, insertion forces and indentation depths. For example, the tip geometry, insertion velocity, the cantilever's spring constant, and the insertion location on the cell. The effects of these factors are studied mostly using experimental methods. Various computational approaches to model the cell membrane insertion are also explored, such as finite element analysis (FEA) and molecular dynamics. In this literature study, the following research gap has been identified:

- The factors that have been observed to affect insertion success rate and insertion force and indentation depth are tip geometry, cantilever spring constant, insertion velocity and location of cell membrane insertion. However, the last three have been insufficiently researched (only one or two papers).
- Additionally, most studies lack proper statistical analysis due to small sample sizes and not isolating independent variables, causing low statistical power and the inability to conclude on the influence of just one factor.

The goal of this research then became to employ the force feedback of the atomic force microscope for guidance and monitoring cell membrane insertion. The research question has been defined as:

> *How to reproducibly and quantifiably monitor cell membrane insertion events using force spectroscopy?*

With sub-questions:

1. What is the influence of AFM tip velocity and location of cell membrane insertion?
2. What is the optimal tip geometry and cantilever stiffness for cell membrane insertion?

At the beginning of the research, reproducibility and quantifiability of cell membrane insertion events were defined to answer the "how" part of the main research question. Firstly, the reproducibility is measured as how often a discontinuity ("force drop") in a set of force spectroscopy curves occurs as a percentage, this is then referred to as the success rate or the occurrence rate. The quantifiability is defined by how clearly these discontinuities are visible, which is measured as the value of the force drop (height of peak). Additionally, insertion force and indentation depth are also measured to gain insights into how these can be minimized during single-cell injection and biopsy experiments.

To answer sub-questions (1) and (2), the effects of the four factors were systematically analysed for their influence on cell membrane insertion success rate and visibility. Furthermore, to process thousands of force spectroscopy curves, data processing algorithms were created and employed to enable large sample sizes for the statistical analyses. The statistical analyses consisted of the calculation of the success rate which was visualised in bar charts, and a multiple linear regression to quantify the effects of the four factors on the characteristics of an insertion event: force drop, insertion force and indentation depth.

Concerning sub-question (1), the location of cell membrane insertion was measured as the height of the cell at the location of insertion. The results from the statistical analyses indicate that cell height has a significant influence, namely that selecting large cells (5 μm) and the highest location on the cell, increases force drop occurrence from 10% to 40% while decreases the force drop visibility. This is often also paired with a decrease in insertion force and an increase in indentation depth. This behaviour might be explained by local cell elasticity differences based on the thickness of the cell.

Furthermore, regarding sub-question (2), the tip geometry effects were analysed using different tip diameters and the results demonstrate that reducing the tip diameter from 2 to 0.7 μm did not affect the occurrence rate, while it did increase force drop visibility from $\sim$250 to $\sim$600 pN. This was paired with an increase in insertion force of $\sim$1 nN. The results also showed that the spring constant of the cantilever has significant influence, specifically that cantilevers with a spring constant of 0.2 N/m achieved higher force drop occurrence (40%) and visibility ($\sim$300 pN), compared to more flexible cantilevers with a spring constant of 0.02 N/m (20% occurrence, $\sim$40 pN visibility). An increase in the spring constant resulted in higher insertion forces. This behaviour may be explained by the inherent change in the loading rate of the force as the spring constant is changed. Thus, for a specific cell, the piezo insertion velocity must be tuned to the cantilever spring constant to obtain an optimal loading rate (second part to the answer of sub-question (1)).

Even though no optimal tip geometry and cantilever spring constant for sub-question (2) were found, the results indicate that especially for spring constant, an optimal range of loading rates could exist for a type of cell. However, to establish this range, very rigorous data collection and analyses is required. In this research, the algorithms created offer data processing as well as statistical computations and can assist future studies in this in-depth analysis of loading rate or other factors.

Finally, it was found that a larger force drop is often paired with higher insertion forces and that cell height and cantilever spring constant are important factors that influence the reproducibility and quantifiability of cell membrane insertion events. These findings provide valuable insights for optimising experimental parameters in single-cell analysis techniques that require physical puncturing of the cell membrane.

6.2. Recommendations

The following points are recommendations for future researchers in this specific field:

- To accompany this research, a validation method should be created to validate if a force drop was the result of a successful insertion event or something else. This will increase the validity of the data and provide information on how a real insertion event can be distinguished from other cell movements. This validation method may involve an extra experimental device built around the AFM or may use already existing capabilities in the AFM such as optical or fluorescence imaging. The AFM optical and fluorescent images however, do not offer a side view.
- To complement this research, the development of theoretical models for the elastic and viscous behaviour of cells, and the cell membrane behaviour, to explain physical results from data analyses.
- In this research, the importance of the spring constant of the cantilever was found. One idea is that changing the spring constant only really changes the force loading rate on the sample. More rigorous and in-depth data collection and analyses are required to quantify the relationship between the loading rate and the insertion success rate, force drop, insertion force and indentation depth. Because the loading rate is the piezo velocity multiplied by the cantilever spring constant, if the optimal loading rate was known for a specific cell, then the piezo insertion velocity can be tuned to the cantilever spring constant during experiments to obtain the optimal loading rate.
- Moreover, the importance of tip diameter for a higher insertion success rate is evident. Therefore, new cylindrical probe designs are suggested for the microfluidic cantilever tips used for single-cell injection and biopsy studies.

6.3. Reflection

6.3.1. Process of project

The idea of this project started in a meeting together with my supervisors (to be) on subcellular imaging techniques using nanoneedle probes in the AFM. I was intrigued by the possibility of visualising these structures by extracting all the information from the force spectroscopy data. We finally settled on a research project, not about subcellular imaging, but on subcellular biopsy using a microfluidic probe in the AFM. My project was directed towards tackling technical issues that my daily supervisor faced during cell experiments with this technique.

After the literature study, I chose to do an experimental study instead of a computational one, as I was keen to learn how it is to work in the cleanroom and the lab with cells. Also, I had my mind set on the microfabrication of 3D printed tips on top of commercially available, tipless cantilevers. I wanted to fabricate tips with different diameters on cantilevers with different spring constants. However, only one model of tipless cantilevers was available, so not a very large range of spring constants could be tested. This showed through in the results, nonetheless the effect could be quantified and was significant. In addition, the smallest tip diameter that I was able to print was 700 nm, and I was hoping to print below 400 nm to see clearer differences between 2 $\mu\mathrm{m}$, 1 $\mu\mathrm{m}$ and 400 nm diameters.

Furthermore, for the insertion velocity experiments, I chose the default value from most papers, which was 2 $\mu\mathrm{m/s}$, and took values close and further away from this value with a maximum at 20 $\mu\mathrm{m/s}$. The data collection on different cell heights was more straightforward, the AFM control system allowed me to define a grid on which each point of a force-distance curve would be measured. In this way, I was able to collect a lot of data automatically.

The large number of force-distance curves that I was planning to collect also needed to be processed afterwards to extract all the useful information. As processing one force-distance curve was already a tedious process, and multiple would just be repetitive work, I chose to write an algorithm to automate this process. Even though this resulted in some very useful algorithms, this process took a lot of learning time and I encountered countless issues and moments where I had to re-think everything. Luckily, I liked the coding part of this project the most, and happily spent hours behind my laptop to solve the puzzle of writing an algorithm.

The last stage of the project was to do the statistical analyses. I chose to do a multiple linear regression to quantify the effects of the individual experimental factors, as well as their interaction terms. This method was very useful to unravel the multifaceted data that I collected. After the regression, I also had to think very hard about the results and why certain behaviour was observed. This physical interpretation part was also very interesting and I enjoyed making these interpretations based on literature and my ideas. Before this project, I had never heard of multiple linear regression with interaction terms, and I also forgot most of my knowledge of statistics. Therefore, this process involved a lot of reading and teaching myself how this works.

One part of the original research question was changed namely the microfluidic part. I ended up only using solid probes because I was only studying the insertion event and the factors that influence it. Originally, the idea was to find the optimal experimental factors and integrate them into the design of a new microfluidic probe and do experiments on cells. However, quite early on this was already considered to be a bit ambiguous. During the midterm review, this part of the research question was finally dropped.

6.3.2. Timeline

For the first five months, I conducted the literature study for this project. Next to the literature study, I followed various philosophy courses at the Erasmus University in Rotterdam. During this time I enjoyed reading different articles and writing the report. Then, in the following six months, I fabricated all the 3D tips on the tipless cantilevers and imaged them using SEM, also I wrote most of the data processing code in Python (while the AFM was broken). During this time I completed all the cell experiments, which resulted in roughly 12,000 force-distance curves to analyse, of which about 9,000 are on cells. The final stage of this project consisted of all the data processing and statistical analyses. This took another month and a half to complete. After another month I handed in the final thesis report. Originally, the plan was to complete the project within a year, but looking back it seems like I needed some extra time, the complete project took me 14 months.

6.3.3. Personal improvement

Looking back at my thesis project, there are a great amount of personal improvements that I can recognise. First and foremost, I increased my knowledge of many aspects related to my thesis topic, cell biology, mechanobiology, mechanical modelling of cells, cell membrane mechanics, data processing algorithms and statistical analyses using multiple linear regression. Secondly, I greatly advanced my coding skills in Python, as well as the problem-solving skills required during coding. I also improved my time management skills and learned to be open to flexible planning in a period of doing cell experiments, where accurate coordination between the cell culture lab, AFM lab and myself was very important.

Furthermore, I very much enjoyed taking part in the discussions during the Micro and Nano Engineering department meetings, where I learned valuable new presentation skills and critical thinking. Moreover, during the weekly meetings with my supervisors, I learned to prepare for meetings and apply received feedback on my work. I struggled with setting hard deadlines for myself because endless improvements can always be made. During this project I tried my best to set these deadlines, however I found that I still only set them once I was happy enough with my work.

In the end, it was my first time doing a large and in-depth scientific research project, and all that comes with it. Many things went wrong, but also many things that went right. I am very grateful for all the new skills I have gained throughout this process.

III

Appendix

A

Custom 3D tips

A.1. Print evaluations

A.1.1. 2 micron tip

Figure A.1 shows the SEM images of a 2 μm tip printed on a tipless cantilever, and Table A.1 evaluates the print dimensions and compares it to the design dimensions.

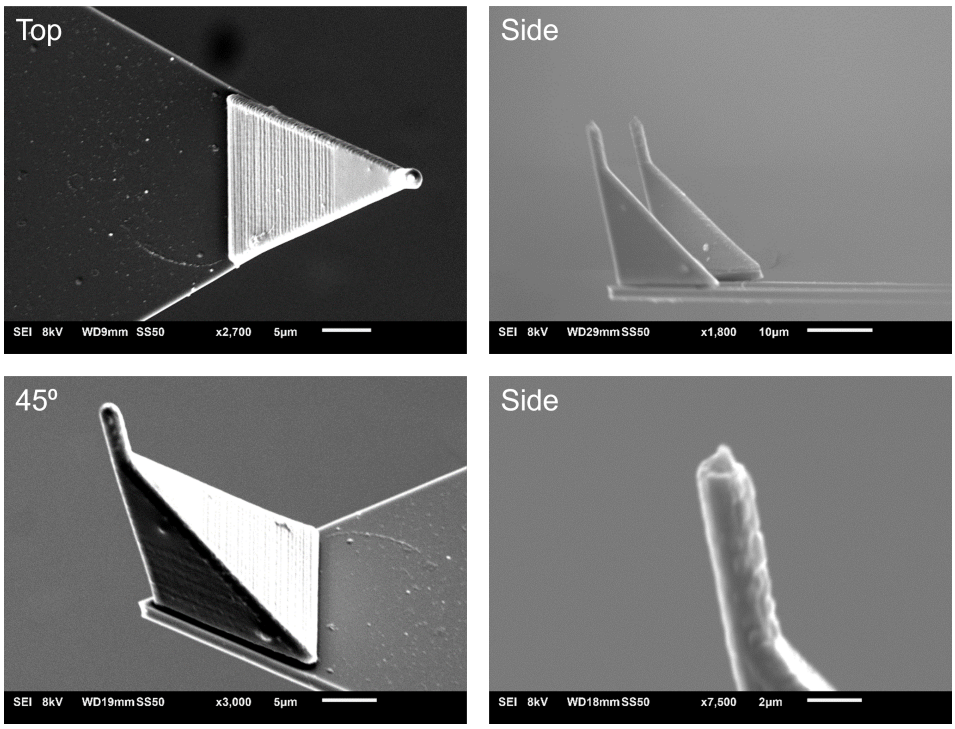

Figure A.1: SEM images from different angles of a custom tip 3D printed using two-photon polymerisation (2PP), with cylindrical tip diameter of 2 μm

Table A.1: Print evaluation of 2 μm tip

	D (μm)	H (μm)	r (nm)
Design	2	8	32
Print 1	1.90	7.29	232
Print 2	1.90	7.50	154
Print 3	2.04	6.92	538
Print 4	2.07	7.08	220
Print 5	1.94	6.84	173
Mean	1.97	7.13	263
Uncertainty	±0.08	±0.33	±192

A.1.2. 1 micron tip

Figure A.2 shows the SEM images of a 1 μm tip printed on a tipless cantilever, and Table A.2 evaluates the print dimensions and compares it to the design dimensions.

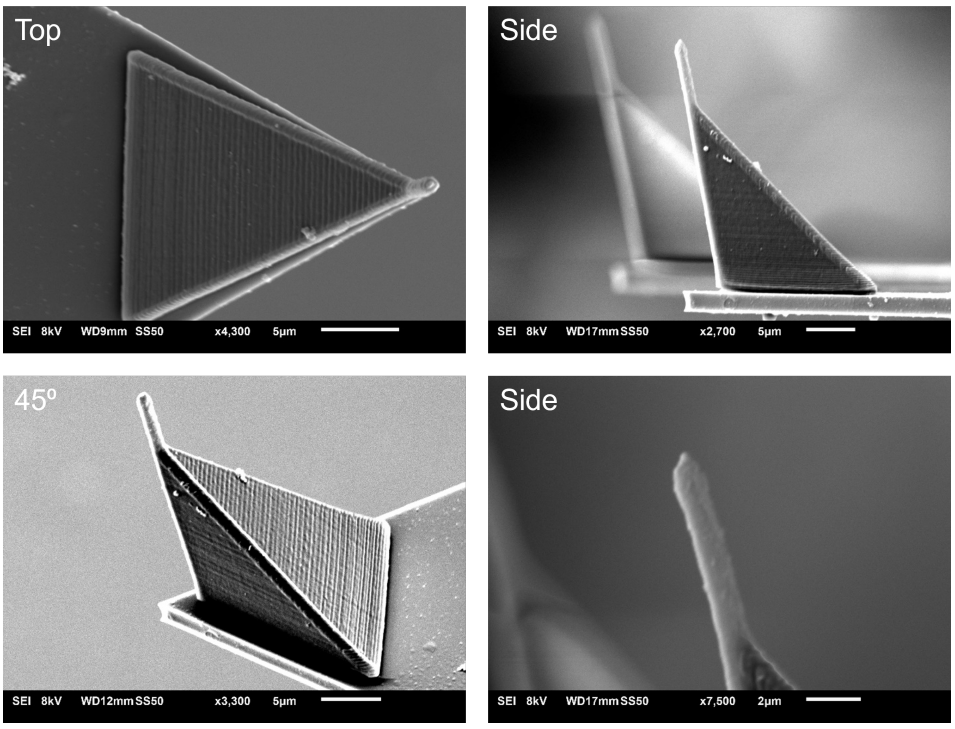

Figure A.2: SEM images from different angles of a custom tip 3D printed using two-photon polymerisation (2PP), with cylindrical tip diameter of 1 μm

Table A.2: Print evaluation of 1 μm tip

	D (μm)	H (μm)	r (nm)
Design	1	7.5	32
Print 1	0.93	6.46	156
Print 2	1.11	7.22	120
Print 3	1.09	6.76	125
Print 4	1.15	7.23	117
Mean	1.07	6.91	130
Uncertainty	±0.11	±0.39	±20

A.1.3. 0.7 micron tip

Figure A.3 shows the SEM images of a 0.7 μm tip printed on a tipless cantilever, and Table A.3 evaluates the print dimensions and compares it to the design dimensions.

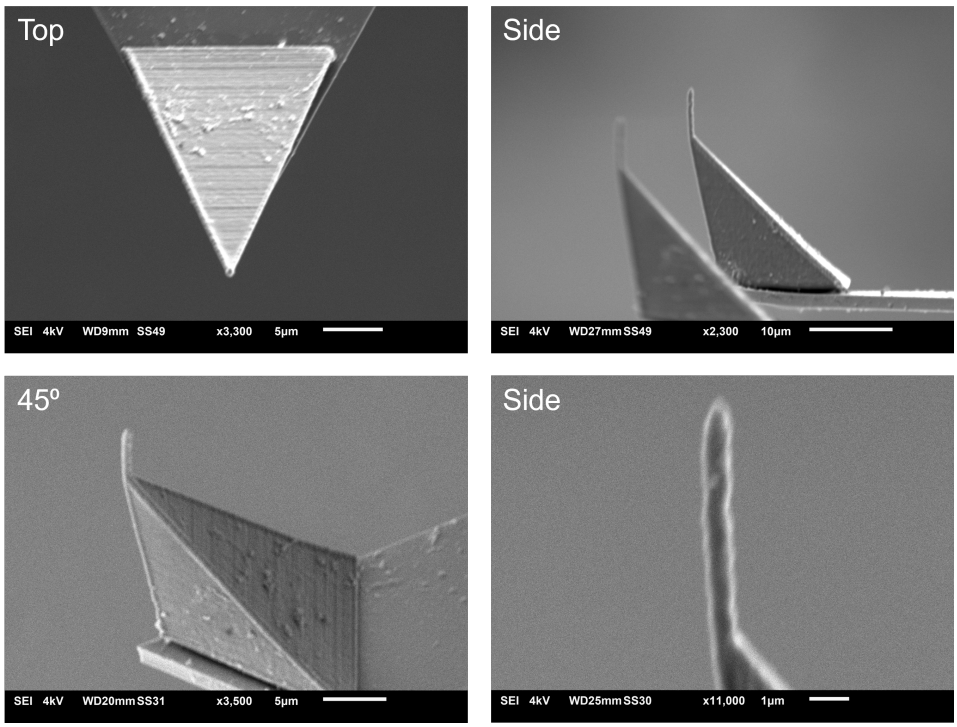

Figure A.3: SEM images from different angles of a custom tip 3D printed using two-photon polymerisation (2PP), with cylindrical tip diameter of 0.7 μm

Table A.3: Print evaluation of 0.2 (0.7) μm tip

	D (μm)	H (μm)	r (nm)
Design	0.2	6.1	32
Print 1	0.62	6.01	116
Print 2	0.72	5.89	86
Print 3	0.73	5.86	110
Print 4	0.78	6.12	106
Mean	0.71	5.97	105
Uncertainty	±0.08	±0.13	±15

A.2. Force spectroscopy experiments on PDMS

The 2 μm tip was used to estimate the Young's modulus of a PDMS sheet using the AFM device, and compared to the Young's modulus measured by a nanoindenter of the same PDMS sheet. The results of the AFM and nanoindenter measurements are shown in Table A.4.

Table A.4: Results of the effective Young's modulus measurements of a PDMS sheet from AFM and nanoindenter data.

Data number	AFM - Y.m. (MPa)	Nanoindenter - Y.m. (MPa)
1	6.511	5.209
2	5.861	5.189
3	5.974	5.094
4	5.784	-
5	5.533	-
6	5.436	-
7	6.148	-
Mean	5.892	5.164
Uncertainty	0.538	0.057

A.3. AFM chip holder

In this case, it was chosen to make a holder that can hold three AFM chips, and that can be 3D printed. Figure A.5 shows the final design in SolidWorks. Furthermore, the fixation mechanism will be using a tape available next to the NanoScribe to tape down the back part of the AFM chip (not the cantilever side) to the AFM chip holder. The tape will be placed there where the holder is thicker.

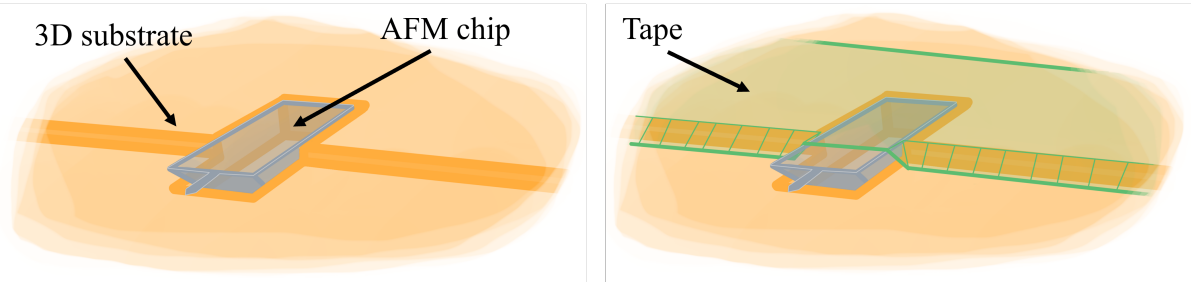

Figure A.4: Drawing showing the concept of AFM chip holder, a tape is used to fix the chip on the substrate

The 3D printer used was a resin-based MSLA (Masked Stereolithography) printer, in this case, the Prusa SL1S, with the resin 'Prusament Resin - Tough Prusa Orange'.The final printed result can be seen in Figure A.6

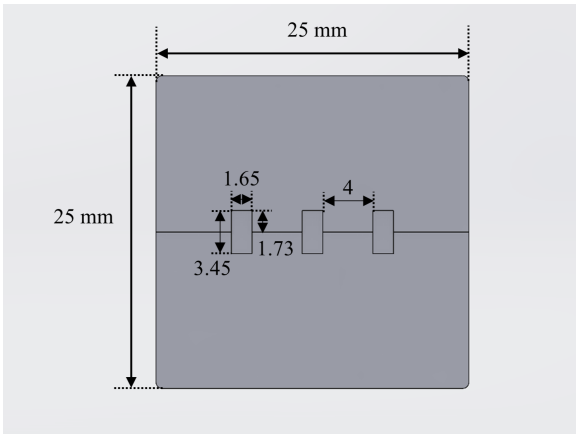

(a) Top view

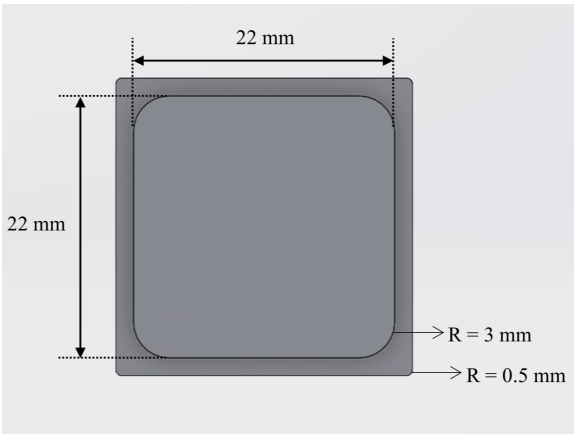

(b) Bottom view

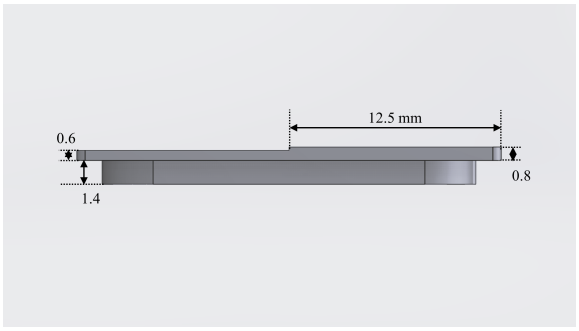

(c) Side view

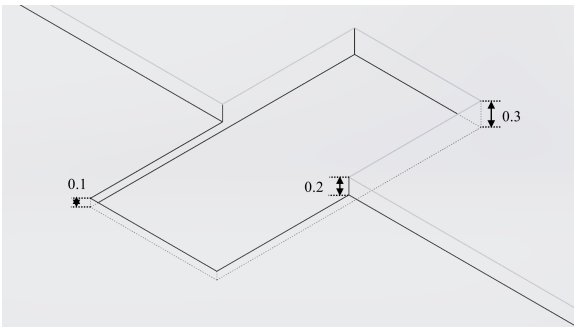

(d) Close-up view of trench for AFM chip

Figure A.5: Dimensions of AFM chip holder

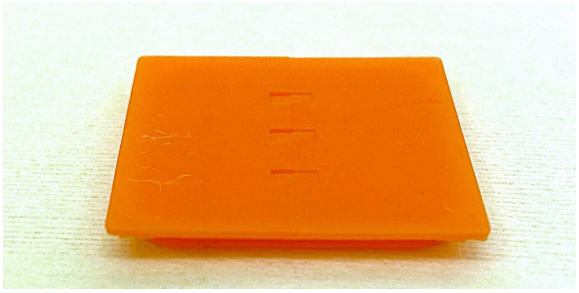

(a) Top-side view

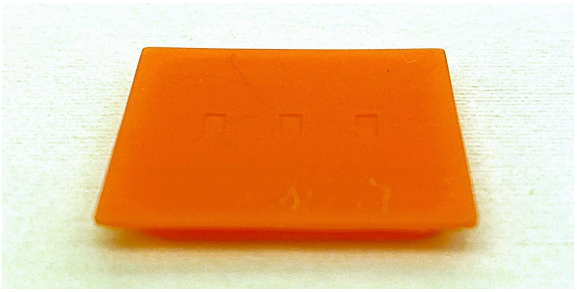

(b) Top-front view

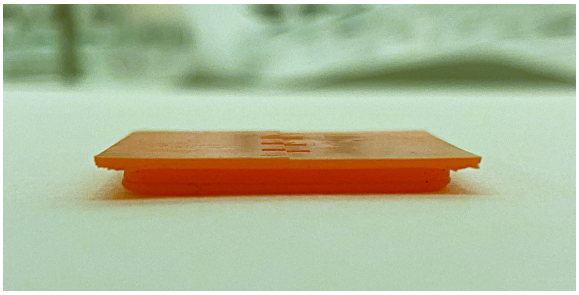

(c) Side-side view

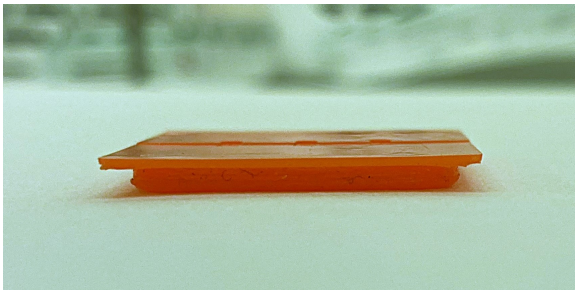

(d) Side-front view

Figure A.6: Final printed outcome of design

B

Algorithms

The complete code is available on GitHub at `https://github.com/Marie762/AFM-JPK`

B.1. Contact point determination

In this section, the different algorithms for contact point detection are described in pseudocode, and the results of the evaluation are presented.

B.1.1. Deviation from baseline

The deviation from the baseline method is implemented as seen in Algorithm 1.

Algorithm 1 Deviation from Baseline Method

procedure DetermineContactPoint($force\_distance\_curve$, $h1$, $h2$)
    Estimate Baseline:
        Fit a linear baseline using the first half of the force-distance data.
        Extend the baseline across the entire force-distance curve.
    Compute Deviations:
        For each data point, calculate the deviation from the baseline.
    Identify Initial Contact:
        Locate the first point where deviation exceeds threshold $h1$.
    Refine Contact Point:
        Trace back to find the first point where deviation falls below threshold $h2$.
    Return: The determined contact point.
end procedure

The results of the deviation from the baseline method are given in Table B.1.

Table B.1: Evaluation results of the deviation from baseline method for contact point determination, using the mean absolute deviation (MAD) error, and the confidence intervals (CI) 5 to 95% of the error

Method	MAD	CI 0.05	CI 0.95
Deviation from baseline	0.5691	0.0198	1.3698

B.1.2. Ratio of variances (RoV)

The ratio of variances (RoV) method is implemented as seen in Algorithm 2.

Algorithm 2 Derivative-Based Contact Point Detection

1: **procedure** DetermineContactPointRoV($force\_data$)
2: **Compute RoV:**
3: Calculate the RoV of the force data.
4: **Detect Peaks:**
5: Detect all the peaks in the RoV using a peak detection algorithm.
6: **Identify Contact Point:**
7: Select the highest peak.
8: **Return:** The determined contact point.
9: **end procedure**

The results of the RoV method are given in Table B.2.

Table B.2: Evaluation results of the RoV method for contact point determination with different numbers for the parameter N, using the mean absolute deviation (MAD) error, and the confidence intervals (CI) 5 to 95% of the error

N	MAD	CI 0.05	CI 0.95
100	1.5112	0.0580	3.4674
200	1.3650	0.0455	3.2141
300	1.1561	0.0079	3.2275
400	0.7525	0.0072	2.5416
500	0.6245	0.0141	2.1370
600	0.5504	0.0199	1.6830
700	0.6655	0.0250	2.3276
800	0.7553	0.0322	2.5979

B.1.3. Linear/non-linear piecewise regression

The linear/non-linear piecewise regression method is implemented as seen in Algorithm 3.

Algorithm 3 Piecewise Function-Based Contact Point Detection

procedure DetermineContactPointPiecewise($force\_distance\_curve$)
    Define Model:
        Construct a piecewise function comprising:
            - A linear segment representing the baseline.
            - A non-linear segment capturing the interaction post-contact.
    Estimate Curve:
        Fit the defined piecewise function to the entire force-distance curve using appropriate fitting techniques (e.g., least squares).
    Identify Contact Point:
        Determine the transition point between the linear and non-linear segments of the fitted function.
        This transition point corresponds to the contact initiation between the tip and the cell.
    Return: The determined contact point.
end procedure

The results of the linear/non-linear piecewise regression method are given in Table B.3.

Table B.3: Evaluation results of the linear/non-linear piecewise regression method for contact point determination with different non-linear functions, using the mean absolute deviation (MAD) error, and the confidence intervals (CI) 5 to 95% of the error

Piecewise function	MAD	CI 0.05	CI 0.95
Linear - Linear	1.5203	0.4781	2.9949
Linear - Quadratic	1.1164	0.2806	2.5283
Linear - Cubic	1.0817	0.1750	2.1059
Linear - 4th order polynomial	0.7655	0.0738	1.7319
Linear - 5th order polynomial	0.5774	0.0510	1.3116
Linear - 6th order polynomial	0.4577	0.0332	1.0197
Linear - 7th order polynomial	0.3883	0.0178	1.0930
Linear - 8th order polynomial	0.5190	0.0504	1.1340
Linear - 9th order polynomial	0.9239	0.0184	2.8000
Linear - Power law	1.0547	0.0683	2.3800
Linear - Exponential	0.7676	0.0287	2.0483

B.1.4. Derivative

The derivative method is implemented as seen in Algorithm 4.

Algorithm 4 Derivative-Based Contact Point Detection

1: **procedure** DetermineContactPointDerivative($force\_distance\_curve$, $h1$, $h2$)
2: **Compute Forward Derivative:**
3: Calculate the forward derivative of the force-distance data.
4: **Identify Initial Contact:**
5: Locate the first data point where the derivative exceeds threshold $h1$.
6: **Refine Contact Point:**
7: Traverse backwards from the identified point to find the first point where the derivative falls below threshold $h2$.
8: **Return:** The determined contact point.
9: **end procedure**

The results of the derivative method are given in Table B.4.

Table B.4: Evaluation results of the derivative method for contact point determination with different numbers for the parameter N, using the mean absolute deviation (MAD) error, and the confidence intervals (CI) 5 to 95% of the error

N	MAD	CI 0.05	CI 0.95
100	0.3952	0.0291	0.9742
200	0.2876	0.0247	0.3889
300	0.2672	0.0174	0.3681
400	0.2345	0.0178	0.3371
500	0.2428	0.0168	0.3724
600	0.1989	0.0086	0.3470
700	0.2111	0.0154	0.3846
800	0.1996	0.0127	0.3736
900	0.2038	0.0162	0.3487
1000	0.2014	0.0182	0.3553
1100	0.2107	0.0250	0.3737
1200	0.2201	0.0194	0.3932
1300	0.2239	0.0141	0.3938
1400	0.2259	0.0270	0.4057
1500	0.2389	0.0405	0.4169
1600	0.2446	0.0418	0.4209
1700	0.2505	0.0591	0.4336
1800	0.2589	0.0355	0.4754
1900	0.2858	0.0418	0.5224
2000	0.3022	0.0531	0.5822
2100	0.3121	0.0355	0.6076
2200	0.3404	0.0536	0.7798

B.2. Multiple linear regression algorithm

To apply the multivariate linear regression to all the data, an algorithm was used. This algorithm is described in pseudocode in Algorithm 5.

Algorithm 5 Multiple Linear Regression Analysis with All Subsets Selection and BIC

procedure AnalyseDependentVariable($dependent\_variable$, $independent\_variables$)
    Data Preparation and Visualisation:
        Standardise all independent variables and their interaction terms.
        Compute and review descriptive statistics for each independent variable and interaction term.
        Calculate the correlation matrix for all independent variables and interaction terms.
        Generate scatter plots for each pair of independent variables and interaction terms.
    Initial Multiple Linear Regression:
        Fit a multiple linear regression model including all independent variables and their interactions.
    Model Selection Using All Subsets:
        Generate All Possible Subsets:
            Enumerate all possible combinations of independent variables and interaction terms.
        Fit Models for Each Subset:
    for each subset S in all possible subsets **do**
        Fit a multiple linear regression model using subset S.
        Compute the BIC for the fitted model.
    end for
        Select Best Model:
            Identify the subset S^* with the lowest BIC value.
    Simplified Multiple Linear Regression:
        Fit a multiple linear regression model using the selected subset S^*.
    Model Comparison:
        Compare the following models:
            - **Full Model**: All independent variables and interactions.
            - **Simplified Model**: Selected variables based on all subsets BIC.
            - **No Interaction Model**: Independent variables without interaction terms.
        Evaluate models based on BIC, Adjusted R-squared, and other relevant metrics.
    Conclusion:
        Draw overall conclusions based on the aggregated evidence from all fitted models.
    Return: Summary of findings and the best-performing model (S^*).
end procedure

C

Force spectroscopy data on cells

C.1. 1 micron tip example

Figure C.1 gives an overview of the measurements taken on one cell using the 1 µm tip.

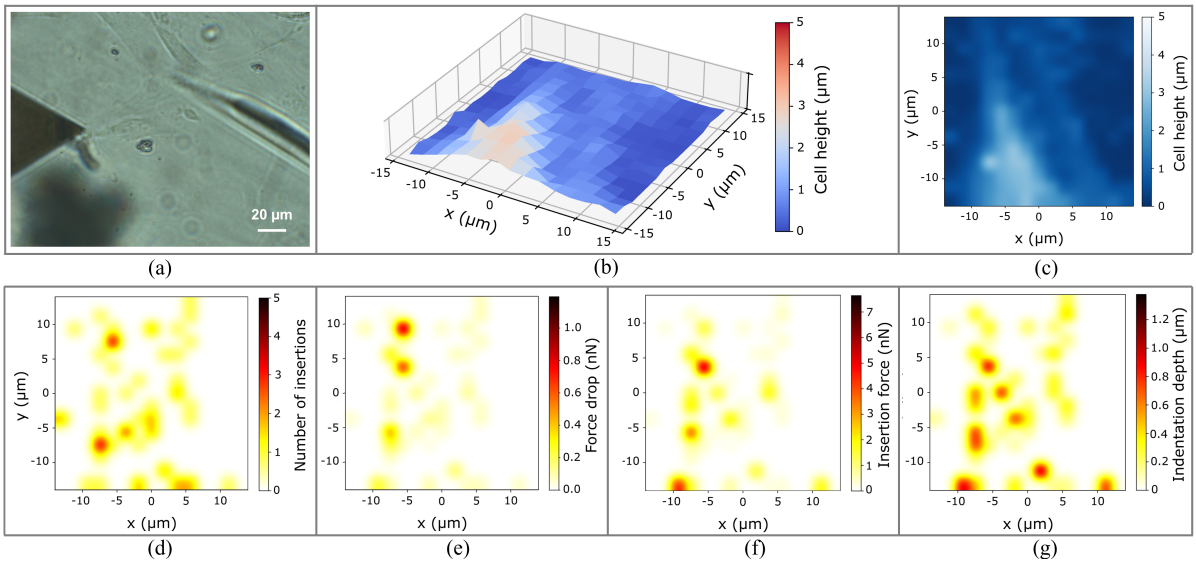

Figure C.1: An example of results obtained from one grid measurement on a cell using the 1 µm tip; (a) shows the optical image of the cell with the cantilever at the end of the grid measurement; the cell height is plotted in (b) 3D and in (c) 2D; (d) visualises the number of insertion events, and (e) force drop, (f) insertion force and (g) indentation depth (g) of the first insertion event.

C.2. 0.7 micron tip example

Figure C.2 gives an overview of the measurements taken on one cell using the 0.7 µm tip.

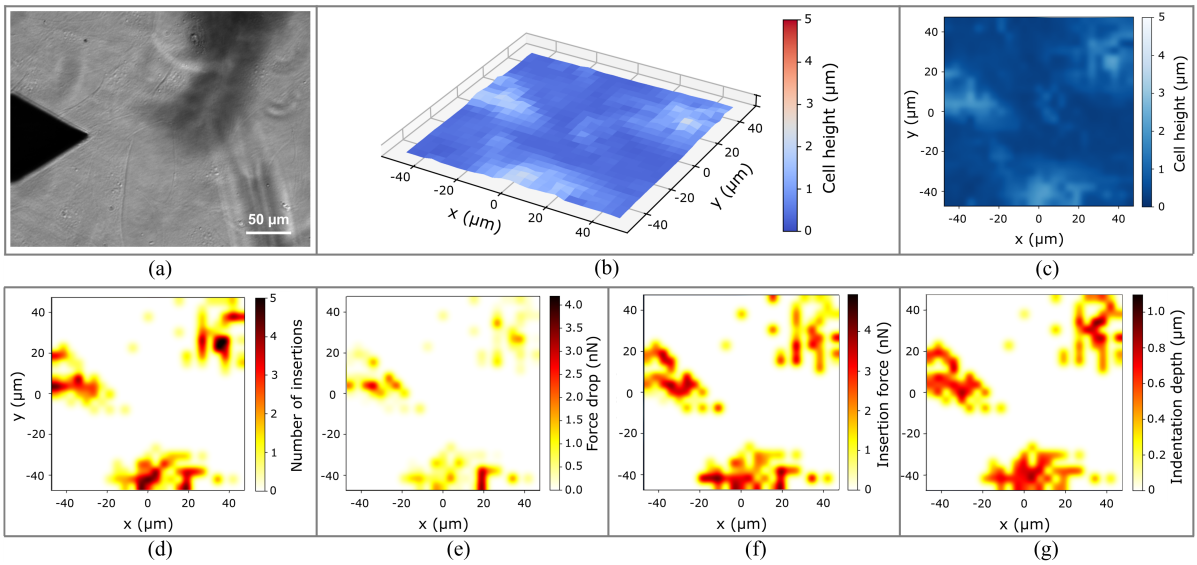

Figure C.2: An example of results obtained from one grid measurement on three cells using the 0.7 µm tip; (a) shows the optical image of the cells with the cantilever at the end of the grid measurement; the cell height is plotted in (b) 3D and in (c) 2D; (d) visualises the number of insertion events, and (e) force drop, (f) insertion force and (g) indentation depth (g) of the first insertion event.

C.3. Re-used clogged microfluidic tip example

Figure C.3 gives an overview of the measurements taken on one cell using the re-used clogged microfluidic cantilever, with 2 µm tip diameter.

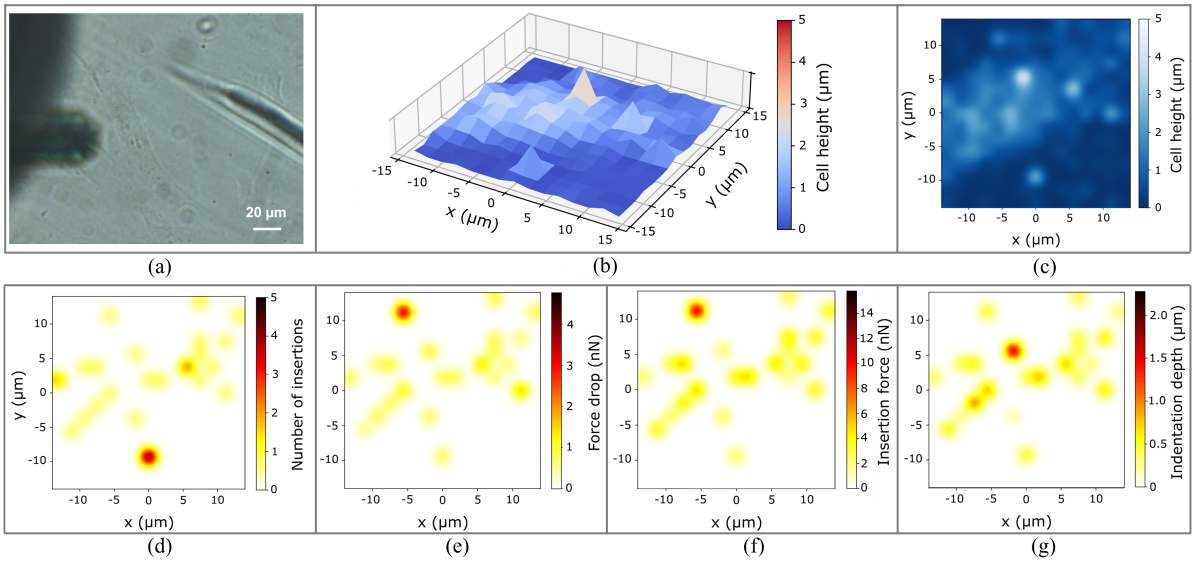

Figure C.3: An example of results obtained from one grid measurement on a cell using the re-used clogged microfluidic cantilever with 2 µm tip diameter; (a) shows the optical image of the cell with the cantilever at the end of the grid measurement; the cell height is plotted in (b) 3D and in (c) 2D; (d) visualises the number of insertion events, and (e) force drop, (f) insertion force and (g) indentation depth (g) of the first insertion event.

D

Statistical analysis

D.1. Simple linear regression

First, all the independent variables and the outcome variables are shown in Table D.1. This table also includes a few rows of the actual values of these variables.

Table D.1: The independent variables and outcome variables, including the first three rows of the data.

H	D	V	S	FD	IF	ID
2.52	2.00	2.00	0.33	0.15	0.54	0.19
1.57	2.00	2.00	0.33	0.15	0.74	0.16
1.59	2.00	2.00	0.33	0.51	4.37	0.88

Second, the independent variables are standardised, and the new values will be more centred around zero, see Table D.2.

Table D.2: The standardised independent variables, and unstandardised outcome variables. Again, including the first three rows of the data.

H	D	V	S	FD	IF	ID
0.15	1.09	-0.40	0.78	0.15	0.54	0.19
-0.62	1.09	-0.40	0.78	0.15	0.74	0.16
-0.61	1.09	-0.40	0.78	0.51	4.37	0.88

The descriptive statistics are given of the unstandardised data. The description includes the mean, standard deviation (std), lower and upper quartiles (Q1 and Q3), median, and maximum and minimum values. Table D.3 shows the descriptive statistics of all the variables.

Table D.3: Descriptive statistics of the independent variables and outcome variables (all unstandardised)

	H	D	V	S	FD	IF	ID
Mean	2.34	1.39	4.23	0.16	0.35	1.65	0.82
Std	1.23	0.55	5.58	0.21	0.84	1.96	0.68
Min	0.50	0.70	0.50	0.02	0.00	0.05	0.00
Q1	1.35	1.00	2.00	0.02	0.02	0.37	0.35
Median	2.13	1.00	2.00	0.15	0.09	0.81	0.66
Q3	3.06	2.00	2.00	0.22	0.25	2.22	1.04
Max	6.28	2.00	20.00	1.15	9.41	15.78	5.07

The simple linear regression between each independent variable and the outcome variables is applied. The regression results are summarised in Tables D.4, D.5 and D.6, for force drop, insertion force, and indentation depth, respectively.

In the tables, 'coef' refers to the coefficients in front of each variable. The coefficient of 'H' refers to the slope of the linear fit, and 'Intercept' to the y-intercept of the linear fit. Furthermore, the table shows the standard deviation ('Std err'), t-statistic ('t'), P-value ('P >|t|', 95% upper and lower confidence intervals ('[0.025 0.975']), and finally the R-squared to measure the goodness of fit.

Table D.4: Regression results for FD ~ H, FD ~ D, FD ~ V, and FD ~ S

	Coef	Std err	t	P>|t|	[0.025	0.975]	R -squared
Intercept	0.3510	0.019	18.702	0.000	0.314	0.388	0.008
H	0.0748	0.019	3.982	0.000	0.038	0.112	
Intercept	0.3510	0.019	18.632	0.000	0.314	0.388	0.000
D	-0.0165	0.019	-0.877	0.381	-0.053	0.020	
Intercept	0.3510	0.019	18.852	0.000	0.314	0.387	0.024
V	-0.1297	0.019	-6.968	0.000	-0.166	-0.093	
Intercept	0.3510	0.017	20.660	0.000	0.318	0.384	0.187
S	0.3651	0.017	21.486	0.000	0.332	0.398	

Table D.5: Regression results for IF ~ H, IF ~ D, IF ~ V, and IF ~ S

	Coef	Std err	t	P >|t|	[0.025	0.975]	R-squared
Intercept	1.6494	0.044	37.676	0.000	1.564	1.735	0.003
H	0.1032	0.044	2.358	0.018	0.017	0.189	
Intercept	1.6494	0.043	37.991	0.000	1.564	1.735	0.019
D	-0.2727	0.043	-6.280	0.000	-0.358	-0.188	
Intercept	1.6494	0.042	38.820	0.000	1.566	1.733	0.061
V	-0.4839	0.042	-11.386	0.000	-0.567	-0.401	
Intercept	1.6494	0.038	43.770	0.000	1.576	1.723	0.261
S	1.0039	0.038	26.633	0.000	0.930	1.078	

Table D.6: Regression results for ID ~ H, ID ~ D, ID ~ V, and ID ~ S

	Coef	Std err	t	P >|t|	[0.025	0.975]	R-squared
Intercept	0.8163	0.013	60.488	0.000	0.790	0.843	0.206
H	0.3081	0.013	22.824	0.000	0.282	0.335	
Intercept	0.8163	0.015	54.018	0.000	0.787	0.846	0.005
D	0.0456	0.015	3.014	0.003	0.016	0.075	
Intercept	0.8163	0.015	53.914	0.000	0.787	0.846	0.001
V	0.0175	0.015	1.155	0.248	-0.012	0.047	
Intercept	0.8163	0.015	53.922	0.000	0.787	0.846	0.001
S	-0.0211	0.015	-1.396	0.163	-0.051	0.009	

D.2. Multiple linear regression without interactions

In this section, multiple linear regression without interactions is applied. The correlation matrix for all independent variables and outcome variables is calculated, and the results are shown in the paper. These correlations are also visualised in scatter plots, such as the pair plot in Figure D.1.

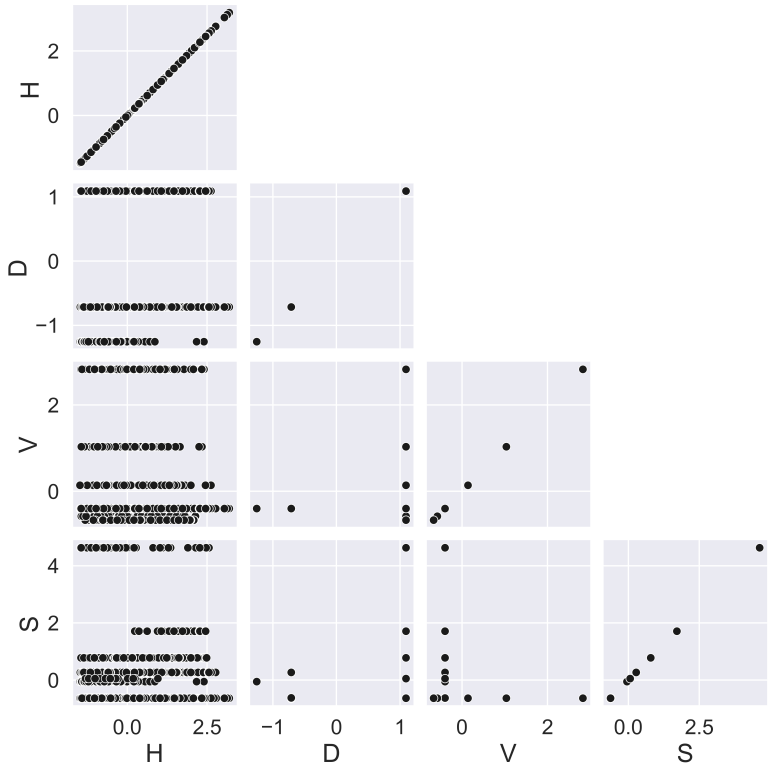

Figure D.1: Pair plot showing scatter plots of each variable against each other

The correlations between each variable and each outcome variable are visualised in a scatter plot, see Figure D.2.

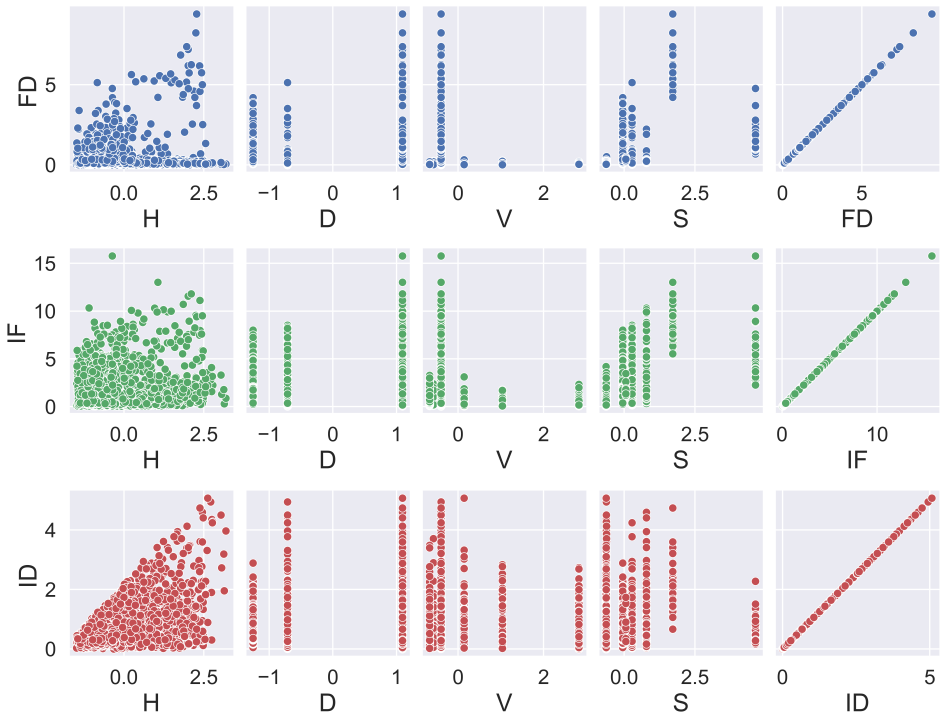

Figure D.2: Pair plots showing scatter plots of each variable against the outcome variables

D.2.1. Force drop

A multiple linear regression without interactions is applied to force drop, the results are shown in Table D.7.

Table D.7: Regression results for FD ~ H + D + V + S

	Coef	Std err	t	P >|t|	[0.025	0.975]	R-squared
Intercept	0.3510	0.017	20.884	0.000	0.318	0.384	
H	0.0969	0.018	5.372	0.000	0.061	0.132	
D	-0.1080	0.021	-5.188	0.000	-0.149	-0.067	0.206
V	0.0037	0.020	0.183	0.855	-0.036	0.043	
S	0.3779	0.018	20.761	0.000	0.342	0.414	

To see what happens when V is removed, a new formula is set up for the multiple linear regression: FD ~ H + D + S, and see if the results improve in terms of statistical significance and confidence intervals. The regression results are shown in Table D.8.

Table D.8: Regression results for FD ~ H + D + S

	Coef	Std err	t	P >|t|	[0.025	0.975]	R-squared
Intercept	0.3510	0.017	20.889	0.000	0.318	0.384	
H	0.0966	0.018	5.376	0.000	0.061	0.132	0.206
D	-0.1062	0.018	-5.850	0.000	-0.142	-0.071	
S	0.3767	0.017	22.169	0.000	0.343	0.410	

D.2.2. Insertion force

A multiple linear regression without interactions is applied to insertion force the results are shown in Table D.9.

Table D.9: Regression results for IF ~ H + D + V + S

	Coef	Std err	t	P >|t|	[0.025	0.975]	R-squared
Intercept	1.6494	0.036	45.631	0.000	1.579	1.720	
H	0.2398	0.039	6.184	0.000	0.164	0.316	
D	-0.5071	0.045	-11.320	0.000	-0.595	-0.419	0.321
V	-0.0166	0.043	-0.385	0.701	-0.101	0.068	
S	1.0644	0.039	27.188	0.000	0.988	1.141	

To see what happens when V is removed, a new formula is set up for the multiple linear regression: IF ~ H + D + S, and see if the results improve in terms of statistical significance and confidence intervals. The regression results are shown in Table D.10.

Table D.10: Regression results for IF ~ H + D + S

	Coef	Std err	t	P >|t|	[0.025	0.975]	R-squared
Intercept	1.6494	0.036	45.641	0.000	1.579	1.720	
H	0.2410	0.039	6.235	0.000	0.165	0.317	
D	-0.5155	0.039	-13.205	0.000	-0.592	-0.439	0.321
S	1.0698	0.037	29.270	0.000	0.998	1.141	

D.2.3. Indentation depth

A multiple linear regression without interactions is applied to indentation depth, the results are shown in Table D.11.

Table D.11: Regression results for ID ~ H + D + V + S

	Coef	Std err	t	P >|t|	[0.025	0.975]	R-squared
Intercept	0.8163	0.013	60.888	0.000	0.790	0.843	
H	0.3344	0.014	23.250	0.000	0.306	0.363	
D	-0.0755	0.017	-4.545	0.000	-0.108	-0.043	0.218
V	0.0133	0.016	0.832	0.406	-0.018	0.045	
S	-0.0206	0.015	-1.419	0.156	-0.049	0.008	

To see what happens when V and/or S is removed, three new formulas are set up for the multiple linear regression: ID ~ H + D + S, ID ~ H + D + V, and ID ~ H + D. The regression results are shown in Table D.12, D.13, and D.14, respectively.

Table D.12: Regression results for ID ~ H + D + S

	Coef	Std err	t	P >|t|	[0.025	0.975]	R-squared
Intercept	0.8163	0.013	60.893	0.000	0.790	0.843	
H	0.3335	0.014	23.258	0.000	0.305	0.362	0.217
D	-0.0687	0.014	-4.746	0.000	-0.097	-0.040	
S	-0.0249	0.014	-1.838	0.066	-0.052	0.002	

Table D.13: Regression results for ID ~ H + D + V

	Coef	Std err	t	P >|t|	[0.025	0.975]	R-squared
Intercept	0.8163	0.013	60.873	0.000	0.790	0.843	
H	0.3352	0.014	23.316	0.000	0.307	0.363	0.217
D	-0.0824	0.016	-5.180	0.000	-0.114	-0.051	
V	0.0214	0.015	1.434	0.152	-0.008	0.051	

Table D.14: Regression results for ID ~ H + D

	Coef	Std err	t	P >|t|	[0.025	0.975]	R-squared
Intercept	0.8163	0.013	60.857	0.000	0.790	0.843	
H	0.3338	0.014	23.267	0.000	0.306	0.362	0.216
D	-0.0725	0.014	-5.055	0.000	-0.101	-0.044	

D.3. Multiple linear regression with interactions

The four independent variables and the five extra interaction variables are standardised and shown in Table D.15, also including the first three rows of the data.

Table D.15: The standardised independent variables, and possible interaction variables. The outcome variable force drop is left unstandardised. Again, including the first three rows of the data.

H	**D**	**V**	**S**	**HxD**	**HxV**	**HxS**	**SxD**	**SxV**	**FD**	**IF**	**ID**
0.15	1.09	-0.40	0.78	0.58	-0.33	0.72	0.96	0.69	0.15	0.54	0.19
-0.62	1.09	-0.40	0.78	-0.14	-0.44	0.21	0.96	0.69	0.15	0.74	0.16
-0.61	1.09	-0.40	0.78	-0.12	-0.44	0.23	0.96	0.69	0.51	4.37	0.88

Table D.16 shows the descriptive statistics of all the variables and interaction variables.

Table D.16: Descriptive statistics of the independent variables, interaction variables, and outcome variables (all unstandardised)

	H	D	V	S	HxD	HxV	HxS	SxD	SxV	FD	IF	ID
Mean	2.34	1.39	4.23	0.16	3.50	10.52	0.38	0.24	0.36	0.35	1.65	0.82
Std	1.23	0.55	5.58	0.21	2.66	16.78	0.61	0.43	0.41	0.84	1.96	0.68
Min	0.50	0.70	0.50	0.02	0.36	0.34	0.01	0.02	0.01	0.00	0.05	0.00
Q1	1.35	1.00	2.00	0.02	1.35	2.49	0.05	0.04	0.05	0.02	0.37	0.35
Median	2.13	1.00	2.00	0.15	2.59	4.39	0.13	0.10	0.29	0.09	0.81	0.66
Q3	3.06	2.00	2.00	0.22	5.21	8.47	0.42	0.22	0.44	0.25	2.22	1.04
Max	6.28	2.00	20.00	1.15	11.15	105.94	6.31	2.30	2.30	9.41	15.78	5.07

The correlation matrix for all independent variables and interaction variables is calculated, see Figure D.3 for the resulting matrix.

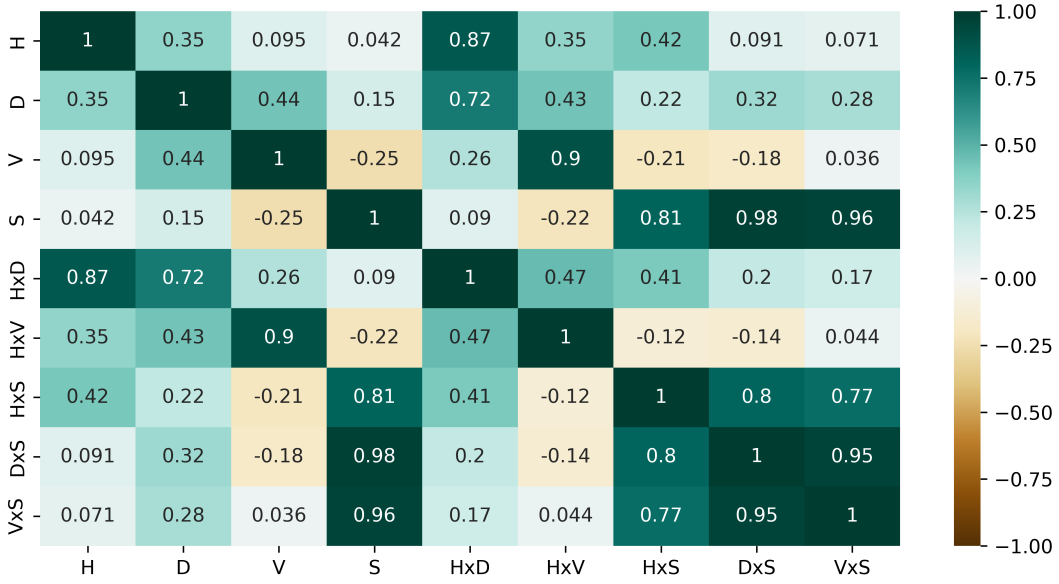

Figure D.3: The correlation matrix for all independent variables and interaction variables, visualised in a heat map

Similarly, the correlations between each variable and each outcome variable can be visualised in a scatter plot, see Figure D.4.

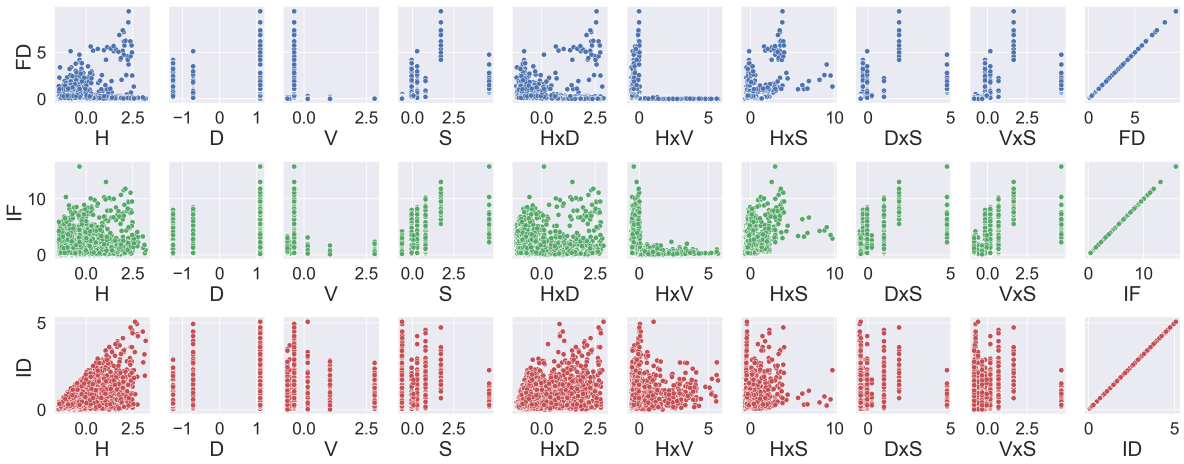

Figure D.4: Pair plots showing scatter plots of each variable against the outcome variables, including interaction variables.

D.3.1. Force drop

The multiple linear regression for all variables and interaction variables is applied to see the effect on force drop. The regression results are shown in Table D.17.

Table D.17: Regression results for FD ~ H + D + V + S + HxD + HxV + HxS + DxS + VxS

	Coef	Std err	t	P >|t|	[0.025	0.975]	R-squared
Intercept	0.3510	0.016	22.281	0.000	0.320	0.382	
H	-0.4381	0.050	-8.731	0.000	-0.537	-0.340	
D	-0.3569	0.048	-7.363	0.000	-0.452	-0.262	
V	3.5035	4.146	0.845	0.398	-4.628	11.635	
S	11.9055	14.392	0.827	0.408	-16.319	40.130	0.304
HxD	0.5258	0.075	7.036	0.000	0.379	0.672	
HxV	-0.0605	0.050	-1.210	0.227	-0.159	0.038	
HxS	0.4646	0.039	12.037	0.000	0.389	0.540	
DxS	-0.0001	0.119	-0.001	0.999	-0.234	0.233	
VxS	-11.5034	13.937	-0.825	0.409	-38.836	15.829	

The result of the BIC value graph for force drop against each unique formula is depicted in Figure D.5, where the minimum BIC value found is highlighted in red. The corresponding formula to that red dot is expressed in Equation D.1.

$$FD \sim H + D + H * D + H * S \tag{D.1}$$

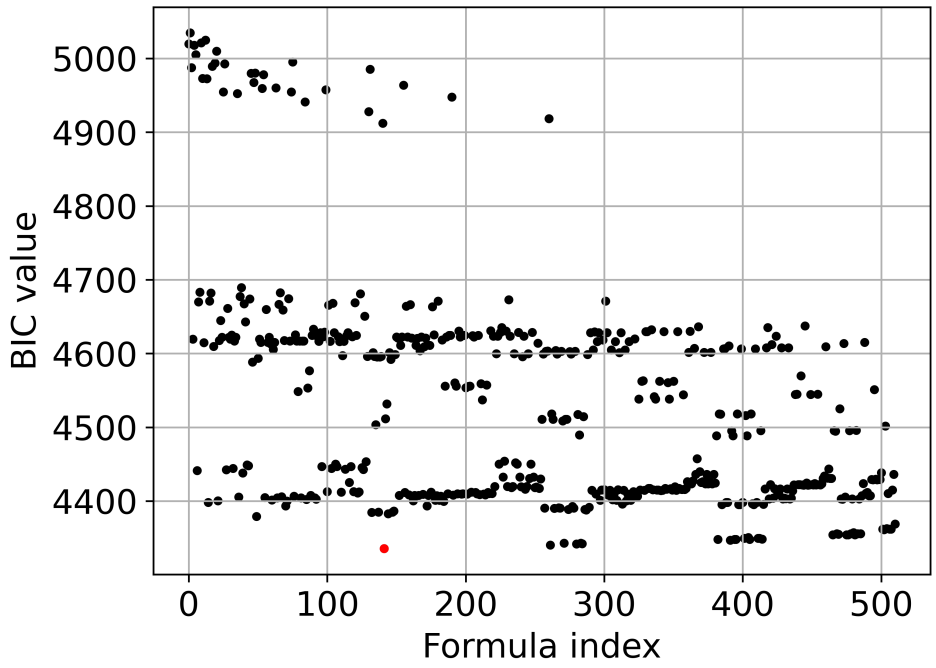

Figure D.5: BIC value graph for the multiple linear regression with interaction results of force drop, the minimum value found is highlighted in red and corresponds to formula $FD \sim H + D + H * D + H * S$.

The regression results for that formula are given in Table D.18.

Table D.18: Regression results for FD ~ H + D + HxD + HxS

	Coef	Std err	t	P >|t|	[0.025	0.975]	R-squared
Intercept	0.3510	0.016	22.283	0.000	0.320	0.382	
H	-0.4341	0.050	-8.689	0.000	-0.532	-0.336	
D	-0.3145	0.036	-8.824	0.000	-0.384	-0.245	0.302
HxD	0.4836	0.067	7.209	0.000	0.352	0.615	
HxS	0.4786	0.017	27.408	0.000	0.444	0.513	

D.3.2. Insertion force

The multiple linear regression for all variables and interaction variables is applied to see the effect on insertion force. The regression results are shown in Table D.19.

Table D.19: Regression results for IF ~ H + D + V + S + HxD + HxV + HxS + DxS + VxS

	Coef	Std err	t	P >|t|	[0.025	0.975]	R-squared
Intercept	1.6494	0.035	47.427	0.000	1.581	1.718	
H	-0.5588	0.111	-5.043	0.000	-0.776	-0.341	
D	-0.5258	0.107	-4.912	0.000	-0.736	-0.316	
V	1.1241	9.155	0.123	0.902	-16.829	19.078	
S	6.4793	31.774	0.204	0.838	-55.835	68.793	0.373
HxD	1.0572	0.165	6.408	0.000	0.734	1.381	
HxV	-0.2956	0.110	-2.677	0.007	-0.512	-0.079	
HxS	0.2615	0.085	3.069	0.002	0.094	0.429	
DxS	-2.5910	0.263	-9.859	0.000	-3.106	-2.076	
VxS	-3.0615	30.770	-0.099	0.921	-63.406	57.283	

The result of the BIC value graph for insertion force against each unique formula is depicted in Figure D.6, where the minimum BIC value found is highlighted in red. The corresponding formula to that red dot is expressed in Equation D.2.

$$IF \sim H + D + S + H * D + H * S + D * S \tag{D.2}$$

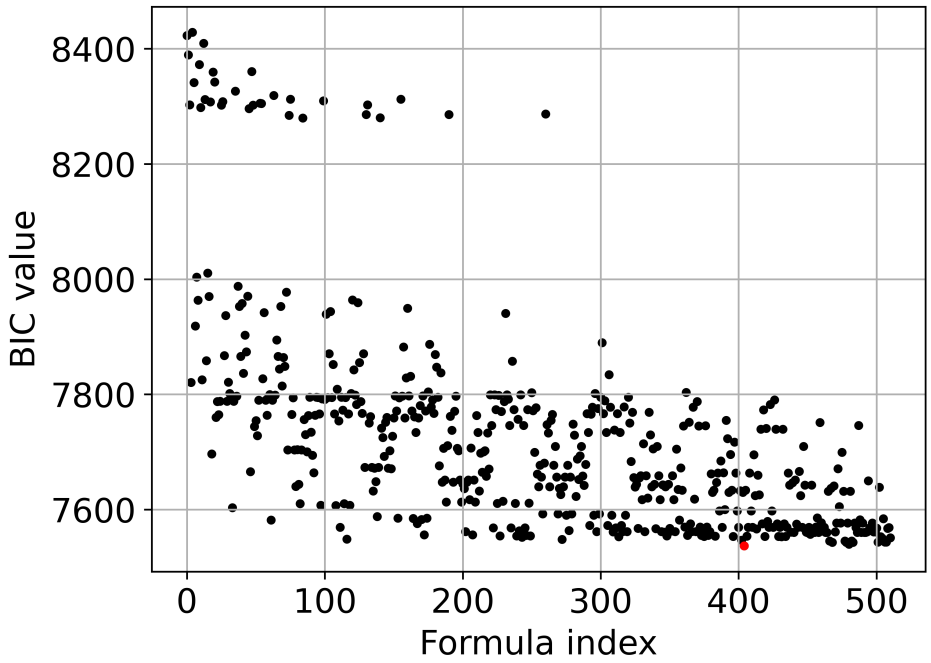

Figure D.6: BIC value graph for the multiple linear regression with interaction results of insertion force, the minimum value found is highlighted in red and corresponds to formula $IF \sim H + D + S + H * D + H * S + D * S$.

The regression results for that formula are given in Table D.20.

Table D.20: Regression results for IF ~ H + D + S + HxD + HxS + DxS

	Coef	Std err	t	P >|t|	[0.025	0.975]	R-squared
Intercept	1.6494	0.035	47.361	0.000	1.581	1.718	
H	-0.5543	0.111	-4.999	0.000	-0.772	-0.337	
D	-0.4520	0.093	-4.850	0.000	-0.635	-0.269	
S	3.2550	0.254	12.829	0.000	2.757	3.753	0.370
HxD	0.8885	0.152	5.862	0.000	0.591	1.186	
HxS	0.3475	0.080	4.355	0.000	0.191	0.504	
DxS	-2.5847	0.260	-9.946	0.000	-3.094	-2.075	

D.3.3. Indentation depth

The multiple linear regression for all variables and interaction variables is applied to see the effect on indentation depth. The regression results are shown in Table D.21.

Table D.21: Regression results for ID ~ H + D + V + S + HxD + HxV + HxS + DxS + VxS

	Coef	Std err	t	P >|t|	[0.025	0.975]	R-squared
Intercept	0.8163	0.013	61.227	0.000	0.790	0.842	
H	0.3125	0.042	7.358	0.000	0.229	0.396	
D	-0.2047	0.041	-4.989	0.000	-0.285	-0.124	
V	-3.0904	3.510	-0.881	0.379	-9.973	3.792	
S	-11.3406	12.181	-0.931	0.352	-35.230	12.549	0.228
HxD	0.1695	0.063	2.680	0.007	0.045	0.294	
HxV	-0.1415	0.042	-3.343	0.001	-0.225	-0.058	
HxS	-0.1377	0.033	-4.215	0.000	-0.202	-0.074	
DxS	0.2096	0.101	2.081	0.038	0.012	0.407	
VxS	10.8748	11.796	0.922	0.357	-12.260	34.009	

The result of the BIC value graph for indentation depth against each unique formula is depicted in Figure D.7, where the minimum BIC value found is highlighted in red. The corresponding formula to that red dot is expressed in Equation D.3.

$$ID \sim H + D + H * S \tag{D.3}$$

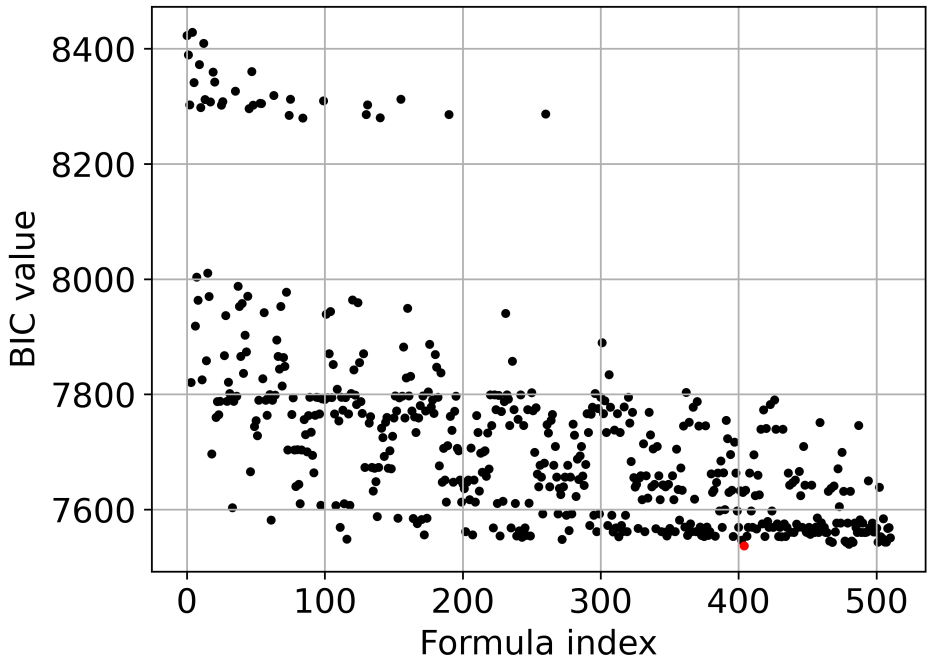

Figure D.7: BIC value graph for the multiple linear regression with interaction results of indentation depth, the minimum value found is highlighted in red and corresponds to formula $ID \sim H + D + H * S$.

The regression results for that formula are given in Table D.22.

Table D.22: Regression results for ID ~ H + D + HxS

	Coef	Std err	t	P >|t|	[0.025	0.975]	R-squared
Intercept	0.8163	0.013	60.983	0.000	0.790	0.843	0.220
H	0.3514	0.015	22.761	0.000	0.321	0.382	
D	-0.0689	0.014	-4.795	0.000	-0.097	-0.041	
HxS	-0.0452	0.015	-3.056	0.002	-0.074	-0.016	

D.4. Average values force drop, insertion force and indentation depth

D.4.1. Spring constant

Table D.23: Mean force drop (nN) per height category and spring constant

Height category (μm)	**S: 0.022** N/m	**S: 0.146** N/m	**S: 0.216** N/m	**S: 0.329** N/m	**S: 1.115** N/m
0.5-1	0.05	0.60	0.24	0.38	1.03
1-1.5	0.04	0.67	0.29	0.21	1.10
1.5-2	0.03	0.88	0.31	0.23	1.39
2-2.5	0.04	0.91	0.35	0.33	1.50
2.5-3	0.04	0.51	0.35	0.25	2.50
3-3.5	0.03	0.33	0.33	0.23	1.04
3.5 or larger	0.03	0.58	0.10	0.24	1.97
Average	**0.04**	**0.64**	**0.28**	**0.26**	**1.50**

Table D.24: Mean insertion force (nN) per height category and spring constant

Height category (μm)	**S: 0.022** N/m	**S: 0.146** N/m	**S: 0.216** N/m	**S: 0.329** N/m	**S: 1.115** N/m
0.5-1	0.40	2.47	2.06	1.33	5.21
1-1.5	0.51	2.50	2.49	1.09	4.28
1.5-2	0.45	2.63	2.51	1.44	5.04
2-2.5	0.44	3.49	3.01	1.56	5.53
2.5-3	0.49	2.88	2.54	2.04	4.72
3-3.5	0.52	2.47	2.16	1.75	3.38
3.5 or larger	0.85	1.22	1.89	2.05	4.48
Average	**0.52**	**2.52**	**2.38**	**1.61**	**4.66**

Table D.25: Mean indentation depth (um) per height category and spring constant

Height category (μm)	**S: 0.022** N/m	**S: 0.146** N/m	**S: 0.216** N/m	**S: 0.329** N/m	**S: 1.115** N/m
0.5-1	0.32	0.46	0.40	0.26	0.52
1-1.5	0.53	0.65	0.57	0.30	0.43
1.5-2	0.67	0.81	0.82	0.43	0.57
2-2.5	0.82	1.11	0.95	0.50	0.89
2.5-3	0.91	1.23	0.85	0.66	0.71
3-3.5	1.07	1.51	0.88	0.72	0.68
3.5 or larger	1.46	0.46	0.94	1.02	0.77
Average	**0.83**	**0.89**	**0.77**	**0.55**	**0.65**

D.4.2. Tip diameter

Table D.26: Mean force drop (nN) per height category and tip diameter

Height category (μm)	**D: 0.7 μm**	**D: 1 μm**	**D: 2 μm**
0.5-1	0.60	0.12	0.33
1-1.5	0.67	0.17	0.20
1.5-2	0.88	0.16	0.24
2-2.5	0.91	0.18	0.29
2.5-3	0.51	0.15	0.25
3-3.5	0.33	0.26	0.22
3.5 or larger	0.58	0.09	0.22
Average	**0.64**	**0.16**	**0.25**

Table D.27: Mean insertion force (nN) per height category and tip diameter

Height category (μm)	**D: 0.7 μm**	**D: 1 μm**	**D: 2 μm**
0.5-1	2.47	1.05	1.24
1-1.5	2.50	1.58	1.12
1.5-2	2.63	1.45	1.49
2-2.5	3.49	1.57	1.41
2.5-3	2.88	1.13	1.82
3-3.5	2.47	1.74	1.68
3.5 or larger	1.22	1.75	1.98
Average	**2.52**	**1.47**	**1.53**

Table D.28: Mean indentation depth (um) per height category and tip diameter

Height category (μm)	**D: 0.7 μm**	**D: 1 μm**	**D: 2 μm**
0.5-1	0.46	0.36	0.30
1-1.5	0.65	0.55	0.38
1.5-2	0.81	0.77	0.49
2-2.5	1.11	0.91	0.63
2.5-3	1.23	0.91	0.69
3-3.5	1.51	0.97	0.80
3.5 or larger	0.46	1.26	1.14
Average	**0.89**	**0.82**	**0.63**